

N O T I C E

THIS DOCUMENT HAS BEEN REPRODUCED FROM
MICROFICHE. ALTHOUGH IT IS RECOGNIZED THAT
CERTAIN PORTIONS ARE ILLEGIBLE, IT IS BEING RELEASED
IN THE INTEREST OF MAKING AVAILABLE AS MUCH
INFORMATION AS POSSIBLE

9950-568

(NASA-CR-164671) FABRICATION AND SURFACE
CHARACTERIZATION OF COMPOSITE REFRACTORY
COMPOUNDS SUITABLE FOR THERMIONIC CONVERTERS
Annual Report, 1 Nov. 1979 - 31 Oct. 1980
(Oregon Graduate Center for Study and)

N81-30185

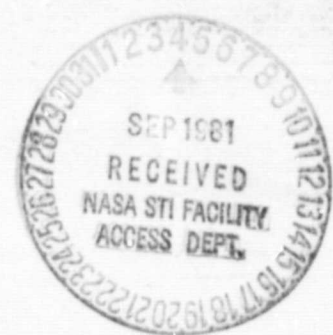
HC AOB/MF A01

Unclass

G3/24 27191

cg

FABRICATION AND SURFACE CHARACTERIZATION
OF COMPOSITE REFRACTORY COMPOUNDS
SUITABLE FOR THERMIONIC CONVERTERS



Oregon Graduate Center

19600 N.W. Walker Road
Beaverton, Oregon 97006

FABRICATION AND SURFACE CHARACTERIZATION
OF COMPOSITE REFRACTORY COMPOUNDS
SUITABLE FOR THERMIONIC CONVERTERS

ANNUAL REPORT
NOVEMBER 1, 1979 - OCTOBER 31, 1980
DECEMBER 1980

JET PROPULSION LABORATORY CONTRACT NO. 955156

OREGON GRADUATE CENTER
19600 N.W. WALKER ROAD
BEAVERTON, OREGON 97006

P. R. DAVIS
L. W. SWANSON

THIS WORK WAS PERFORMED FOR THE JET PROPULSION LABORATORY,
CALIFORNIA INSTITUTE OF TECHNOLOGY SPONSORED BY THE NATIONAL
AERONAUTICS AND SPACE ADMINISTRATION UNDER CONTRACT NAS7-100.

TABLE OF CONTENTS

	Page
I. Introduction	1
II. Rare Earth Hexaboride Surface Characterization - Task A	5
II-A. Clean Surface Characterization of LaB_6	5
II-B. Effects of Adsorbed Carbon Upon LaB_6 Surface Properties	20
II-C. Cesium Adsorption and Cesium-Oxygen Coadsorption on $\text{LaB}_6(100)$ and (110) Surfaces	25
II-C-1. Cs Adsorption on Clean LaB_6	27
II-C-2. Cesium Desorption from the Clean $\text{LaB}_6(100)$ Surface	35
II-C-3. Oxygen Adsorption on $\text{LaB}_6(100)$ and (110)	37
II-C-4. Coadsorption of Cesium and Oxygen onto $\text{LaB}_6(100)$ and (110)	45
II-C-5. Cesium Desorption from the Oxygen Covered $\text{LaB}_6(100)$ Surface	55
II-C-6. Comparison of Cesium-Oxygen Coadsorption on LaB_6 and W.	62
II-D. Evaluation of $\text{LaB}_6(100)$ as a Cesium Vapor TEC Electrode Material	64
III. Characterization of Refractory Alloys and Related Surfaces - Task B	68
IV. Effects of Adsorbates on Refractory Alloy Surface Properties - Task C	73
IV-A. Cesium Adsorption and Cesium-Oxygen Coadsorption on $\text{Zr/O/W}(100)$	73
IV-A-1. Cs Adsorption on $\text{Zr/O/W}(100)$	75
IV-A-2. O_2 Adsorption on $\text{Zr/O/W}(100)$	80
IV-A-3. Cs-O_2 Coadsorption on $\text{Zr/O/W}(100)$	80

TABLE OF CONTENTS (cont.)

	Page
IV-B. Comparison of Cesium Adsorption and Cesium-Oxygen Coadsorption on Zr/O/W(100) and W(100)	85
V. Technical Summary	100
References	103
Appendix	105

I. Introduction

The objective of the JPL thermionics program has been to establish the feasibility of an advanced lightweight, long-life, direct energy conversion system compatible with a nuclear reactor or solar heat source. The principal application foreseen at this time is the use of nuclear power for electric propulsion. Other applications of direct energy conversion that will benefit from this program include nuclear and solar thermionic/thermoelectric power for Earth orbital and lunar applications, as well as terrestrial topping cycle applications.

The objective of the OGC program in thermionics is to fabricate, characterize and evaluate new electrode materials that have the potential of significantly improving converter performance. The underlying philosophy of this work can be summarized in the following assumptions:

- (1) an emitter material for advanced mode TEC operation should exhibit both a low clean work function (2.1 to 3.0 eV) and low volatility;
- (2) the collector electrode work function should be as low as can be tolerated by back emission considerations; and
- (3) it would be desirable to have an emitter and collector of the same material.

Historically the emitter electrode has possessed a high clean surface work function. The advantage of a low clean surface emitter work function is its ability to exhibit high emitter current density

levels at relatively low temperature (e.g. 10 A/cm^2 at 1626 K for LaB_6) without any Cs pressure. This important advantage allows one to reduce the converter cesium pressure and hopefully eliminate or greatly reduce the vacuum arc drop, yielding much greater flexibility in converter design. In addition, it has been suggested that low work function electrode materials such as LaB_6 may greatly increase TEC efficiencies and result in higher power outputs at $\sim 1700 \text{ K}$.¹

For these reasons, the OGC program has paid particular attention to the techniques of fabricating and characterizing the surface properties of promising new electrode materials. Our objective has been to gain a clearer understanding of the basic surface properties of these materials in relation to their utilization as thermionic energy converter electrodes. We will continue to emphasize the study of those factors (e.g., cesium desorption kinetics and mechanisms of low work function production) which are of primary concern to successful thermionic converter performance.

During the past year we have assessed the relevant surface properties of some promising rare earth hexaboride (REB_6) electrode materials, both clean and with adsorbed cesium and cesium-oxygen layers. We have concluded a study of zirconium/tungsten and hafnium/tungsten alloys and have investigated the properties of adsorbed cesium and cesium-oxygen layers on the promising $\text{Zr/O/W}(100)$ surface. Our surface analysis techniques include Auger electron spectroscopy (AES), mass spectroscopy of surface desorption products (TDS),

field emission retarding potential (FERP)² technique of measuring work function and electron reflection, field electron (FEM) and field ion microscopy (FIM) and low energy electron diffraction (LEED).

Two important considerations in the selection of an appropriate emitter electrode material are its work function and volatility. In the case of the cesium thermionic diode it is important to know the variation of emitter work function ϕ_e with temperature T_e and cesium pressure P_{cs} . Then the emitted current density J_e may be determined as a function of these operational parameters. It is entirely equivalent to determine the functional dependence of the cesium coverage $\sigma = \sigma(T_e, P_{cs})$ and the dependence $\phi_e = \phi_e(\sigma)$, which may be done using thermal desorption mass spectrometry and FERP. Using a simple model and measured $\phi_e(\sigma)$ and $\sigma(T)$ curves we have assessed the usefulness of $LaB_6(100)$ as an electrode material in a hypothetical cesium vapor NEP converter.

Volatility of the emitter electrode at the operating temperature should be as low as possible in order to minimize contamination of the collector electrode. In the case of identical emitter and collector materials this may not be a significant problem. For binary electrode materials such as LaB_6 or CeB_6 it is now known that, within certain stoichiometric limits, the volatility is minimized and the vaporization occurs congruently so that emitter material condensing on the collector should not alter its composition.³

For single crystal materials, surface stability is an equally important consideration, since some crystal faces tend to facet, forming thermodynamically more stable structures. We have used FEM and FIM techniques to study stabilities of various crystal faces under high field and high temperature conditions.

During the past year we have concluded a study of a class of refractory materials which consist of dilute alloys of zirconium or hafnium in tungsten or molybdenum. Certain crystal faces of these alloys are known to produce low (~ 2.6 eV) work function surfaces which are unusually stable at elevated temperature (~ 2000 K).^{4,5} Original plans called for completion of the investigation of a group of W-Zr and W-Hf alloys, followed by a similar study of Mo-Zr and Mo-Hf alloys. However, upon completion of the W-Zr and W-Hf investigation, we decided that further work on polycrystalline alloys would not be fruitful, so we shifted emphasis to well-characterized single crystal surface studies.

The particular single crystal system chosen for extensive study was the Zr/O/W(100) surface. This model alloy system provides an ordered surface which lends itself to characterization by surface-sensitive techniques. Previous studies of this system have yielded insight into the nature of the low work function surface and methods of routinely achieving the low work function on this plane have been developed.⁵ During the past year we have carefully investigated the effects of oxygen adsorption, cesium

adsorption and cesium-oxygen coadsorption upon the properties of the Zr/O/W(100) surface. Work function, AES, thermal desorption and electron reflection measurements have been made and the results are compared with results of similar measurements on W(100).

The research program we have pursued during the past year can be conveniently separated into three major tasks:

Task A: Rare earth hexaboride surface characterization, including the effects of cesium and cesium-oxygen adsorbed layers;

Task B: Characterization of refractory alloys and related surfaces;

Task C: Study of the effects of adsorbates on refractory alloy surface properties.

We shall discuss individually the results obtained under each task.

II. Rare Earth Hexaboride Surface Characterization - Task A

II-A. Clean Surface Characterization of LaB₆

We previously reported⁶⁻⁸ studies of the chemical, geometric and electrical properties of clean LaB₆ single crystal surfaces. During the present reporting period we have extended these efforts to include careful FEM and FIM experiments. The aim of these experiments has been a direct comparison of the stabilities of the low index planes under thermal treatment and high field conditions. A brief description of high field phenomena will be included here for clarity.

Field emission is a phenomenon which can occur when the surface potential barrier of a metal is deformed by a sufficiently high externally applied positive field, of the order of 10^7 V/cm. Such a high field can be obtained in practice only by the use of a sharp point as the emitting surface. The surface potential step then becomes a potential hill of finite width and the quantum mechanical probability of electron tunneling from the Fermi level also becomes finite (Fig. 1). The Fowler-Nordheim equation describes this phenomenon,

$$I = A V^2 \exp[-(\phi^{3/2}/\beta V) v(z)] \quad (1)$$

where I is the emitted current, A is a pre-exponential constant, V is the applied voltage, ϕ is the work function, β is a geometric factor such that βV = applied field and $v(z)$ is a slowly varying image correction. The factor β is a function of microscopic local geometry and ϕ is the local work function. Thus, a strongly anisotropic emission pattern, displayed on a phosphor screen, may be obtained for a single crystal with various planes exposed, since the current emitted from a given region is a strong function of the local geometry and work function.

Field ionization is a phenomenon occurring at higher applied fields, of the order of 10^8 V/cm. In this case, a negative field is used and the experiment is performed in a moderate pressure of an imaging gas, such as helium. Electron tunneling occurs in reverse, from gas atoms into the metal. Gas atoms, polarized by the field,

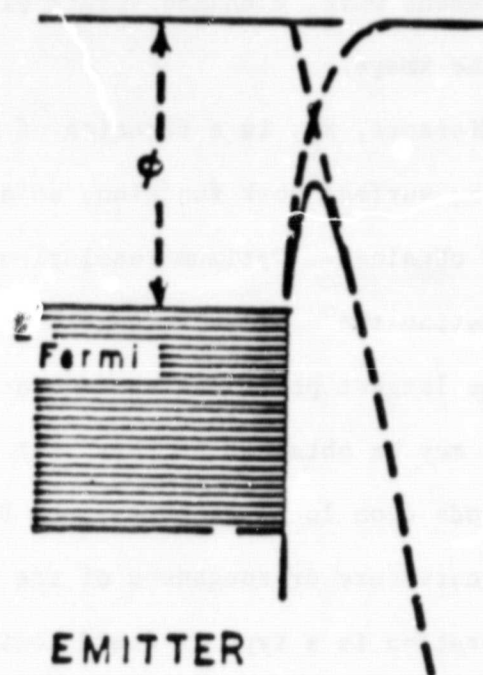


Figure 1. Potential energy diagram of a surface subjected to an external positive electric field (field emission case).

are drawn by the field gradient toward the surface. At some critical distance, x_c , the barrier between the atomic potential well and the surface potential is sufficiently narrow that electron tunneling occurs with high probability (Fig. 2). Ions thus formed are accelerated by the field and strike a fluorescent screen to form an ion emission pattern. In the present work, a channel plate electron multiplier is used to intensify the image.

The critical distance, x_c , is a function of the local field but is insensitive to the surface work function, so an anisotropic ion emission pattern is obtained. Optimum resolution for a given pattern is achieved by adjusting the applied voltage so that x_c is as small as possible over the largest practical surface area. Atomic resolution of surface features may be obtained at this best image voltage (BIV). Since the field depends upon local geometry, the BIV is a measure of the relative local curvature or roughness of the surface.

Field evaporation is a type of field ionization which occurs when the applied field is of sufficient strength to remove the surface atoms themselves. The surface may be cleaned of adsorbed atoms by this method, and substrate atoms may also be removed, leaving a field evaporated end form which is characteristic of equilibrium conditions under a high field. Field evaporation may be done in vacuum or in an imaging gas atmosphere. A thermally equilibrated end form, on the other hand, is achieved by heating in zero applied field with, in general, a different resulting microscopic surface structure.

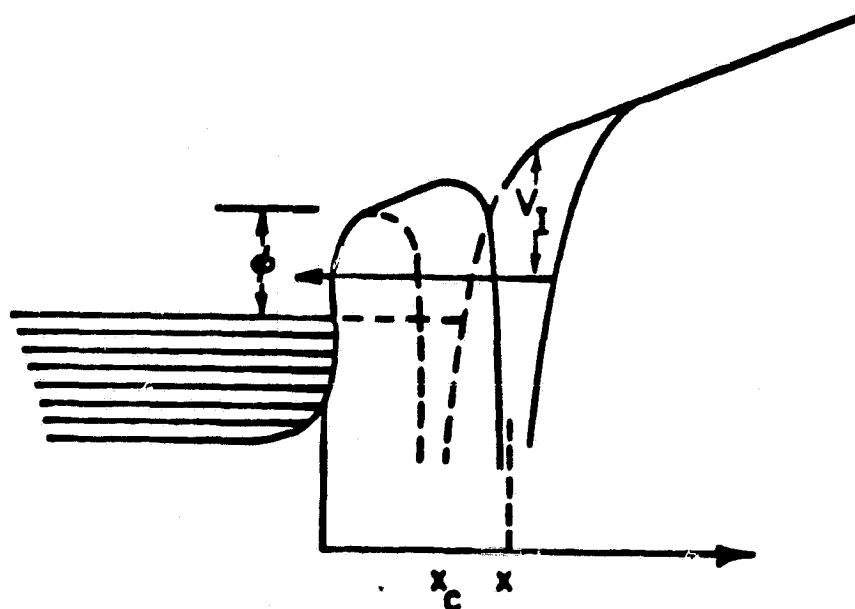


Figure 2. Potential energy diagram of an atom near a surface under the influence of a negative external field (field ionization case). V_I is the ionization potential of the atom.

The low temperature (77 K) field electron and ion emission patterns for three emitter end forms are shown in Figs. 3-8. Figures 3-6 show patterns obtained after field evaporation in H_2 and He; figs. 7 and 8 show the field ion (H_2 image gas) and electron emission patterns of the thermally annealed ($T \sim 1800$ K) end form. Field evaporation in H_2 and He occurred at voltages 20% and 30% above their respective BIV's. The He BIV was ~ 1.9 times larger than the H_2 BIV value. A comparison of the H_2 field ion pattern of Fig. 3, which reflects the local field enhancement distribution, with the corresponding electron pattern in Fig. 4, which reflects both the work function and field distributions, clearly shows that $\phi_{110} < \phi_{100}$ for this end form. In contrast, the end form obtained after field evaporation in He, while exhibiting a similar ion pattern (Fig. 5), shows an electron pattern in Fig. 6 which suggests a work function reversal, i.e., $\phi_{100} < \phi_{110}$. A result similar to Figs. 5 and 6 was obtained after field evaporation in vacuum. By adsorbing H_2 on the He field evaporated end form it was determined that the electron emission pattern difference between Figs. 4 and 6 was not due to adsorbed H_2 .

The field ion and electron patterns of the thermally equilibrated end forms shown in Figs. 7 and 8 are similar to those observed by Futamoto, et al.⁹ However, according to our results the latter authors appear to have inadvertently rotated the field electron pattern 45° relative to their indicated crystallographic designations. Upon thermal equilibration between 1600 to 1800 K the low index planes



Figure 3. Hydrogen field ion image of a (100) oriented LaB_6 emitter after field evaporation in H_2 , BIV = 13 kV.

ORIGINAL PAGE IS
OF POOR QUALITY

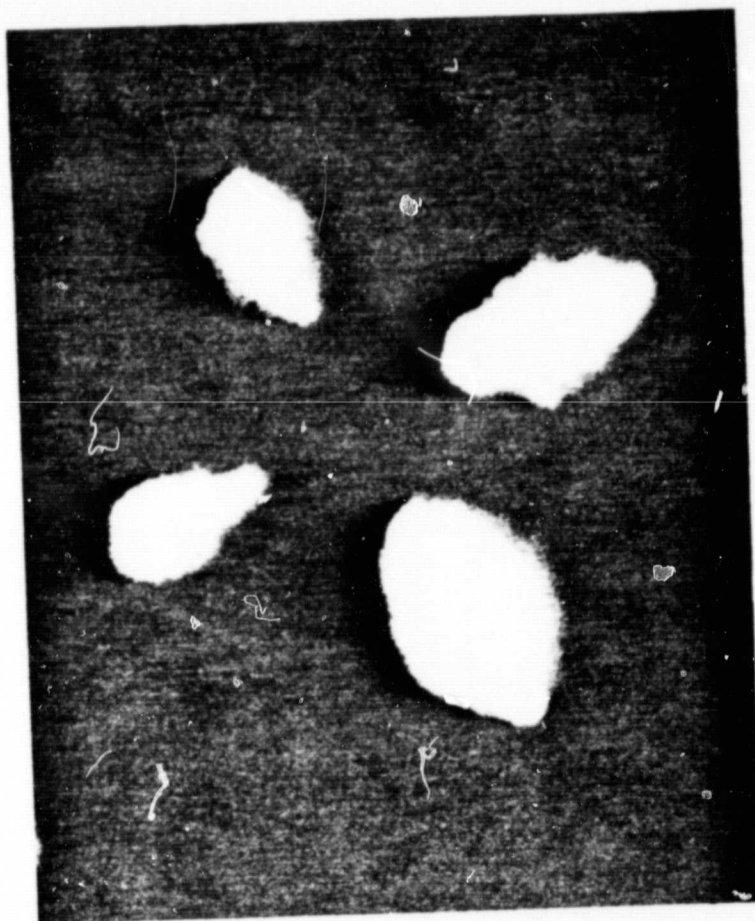


Figure 4. Field electron image of H_2 field evaporated end form.



Figure 5. Helium field ion image of a (100) oriented LaB_6 emitter after field evaporation in He, BIV = 24 kV.

ORIGINAL PAGE IS
OF POOR QUALITY

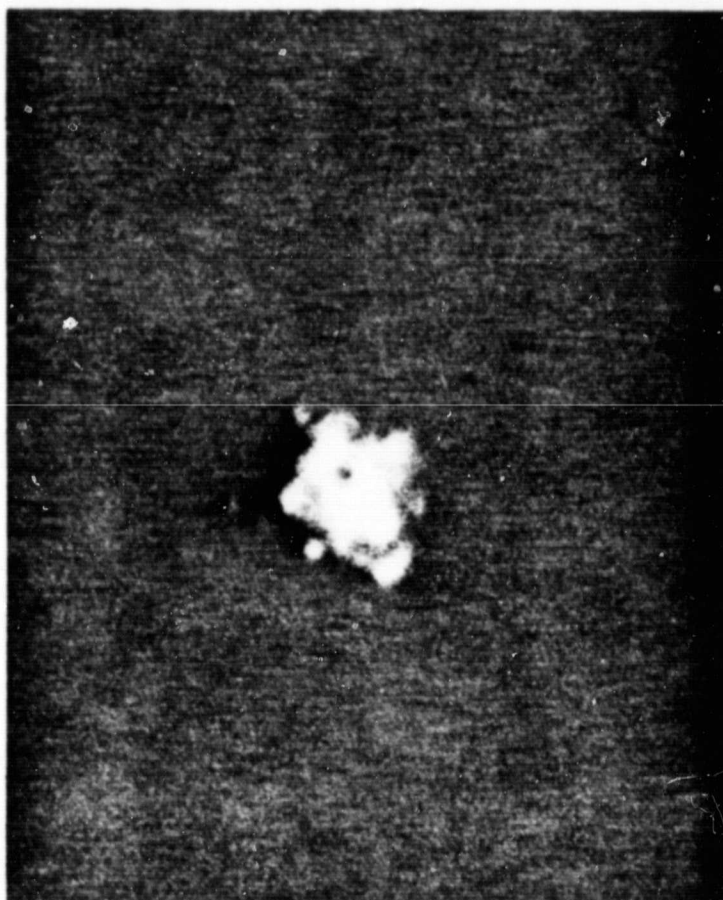


Figure 6. Field electron image of the field evaporated end form.



Figure 7. Hydrogen field ion image of a (100) oriented LaB_6 emitter after annealing 15 min. at 1800 K.

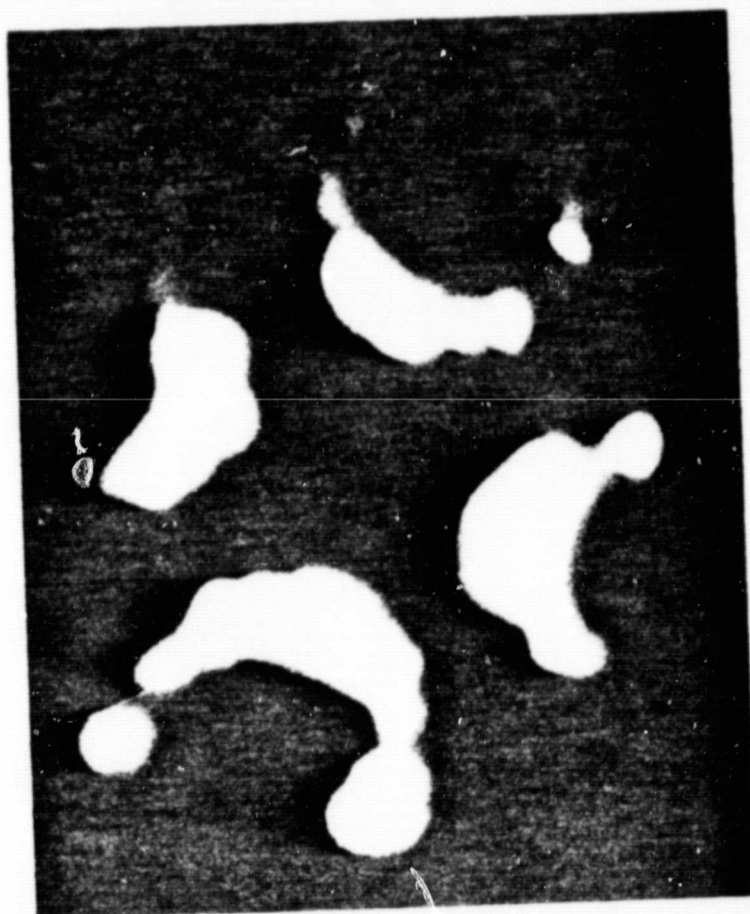


Figure 8. Field electron image of thermally annealed end form.

increase in size in the order $(111) > (110) > (100)$. In addition, the (210) - (310) regions become slightly faceted. Also in agreement with Putamoto, et al.,⁹ we found that long term heating at $T > 1800$ K led to irreversible formation of field enhanced microcrystallites randomly distributed over the surface.

These results clearly show that the work function difference between the (110) and (100) planes of the LaB_6 can be radically changed by the conditions of field evaporation. The thermal faceting observed in the FIM patterns shows that the (111) , (110) and (100) planes are the most thermodynamically stable crystal faces in vacuum. Further studies will be required to determine the thermal/geometric stability and the relationship between the surface B/La atom ratio and work function for the higher index planes, e.g., (321) , (346) , (210) .

Table I shows the best image voltages (BIV) and corresponding slopes m of the electron $I(V)$ characteristics of the various emitter end forms plotted according to equation (1) in the form $\log(I/V^2)$ vs. $1/V$. In this case, the slope m is given by

$$m = 2.8 \times 10^7 \phi^{3/2}/\beta \quad (2)$$

An important finding was the nearly 68% decrease in m when the field evaporated end forms were thermally equilibrated. According to equation (2) a reduction in m implies either a decrease in ϕ or increase in β . Since the H_2 BIV values (and hence β values) for the field evaporated and thermally equilibrated end forms are nearly

TABLE I

SUMMARY OF BEST IMAGE VOLTAGES (BIV) AND FOWLER-NORDHEIM SLOPES
FOR THE INDICATED IMAGE GAS AND END FORM OF THE LaB_6 EMITTER

End Form	Image Gas	BIV (kV)	Slope m (volts)	Low Work Function Plane
Field Evap. in H_2	H_2	13	4.4×10^4	(110)
Field Evap. in He	He	25	4.4×10^4	(100)
Thermally Equil. (~ 1800 K)	H_2	13	1.4×10^4	(112)

identical, we conclude that the average ϕ for the latter end form is 32% lower than the H_2 or He field evaporated end forms.

Atom probe studies of the LaB_6 surface in He imaging gas show field evaporation occurring as $B/La \sim 6$, thus leaving a near stoichiometric surface.¹⁰ However, upon heating to $T \sim 1800$ K the atom probe results showed predominantly La in the surface layer. In view of these results we conclude that thermal equilibration leads to a restructuring of the surface causing the "quenched in" 77 K surface to exhibit a simultaneous reduction in ϕ and formation of a La rich surface layer. From the Fig. 8 photo we further conclude that low work function regions of the thermally equilibrated end form occur at the higher index (112) planes. However, from the obvious faceting of the (210)-(310) region (see Fig. 7) an equally low work function for these higher index planes cannot be ruled out.

From the Table I results and Figs. 3-8 patterns of the field evaporated end forms, it can be concluded that, although the work function distribution is dramatically changed depending on whether field evaporation occurs in H_2 or He, the average work function is virtually unchanged. The reason for the reversal in the minimum work function between the (110) and (100) planes is believed to be due to an anisotropy in the surface B/La ratio brought about by field evaporation in H_2 . According to atom probe results,¹⁰ La is preferentially removed from the surface when field evaporated in H_2 . If this phenomenon is specific to the (100) plane, it may lead to an

anisotropy in the surface B/La stoichiometry and hence the change in the work function distribution noted in Figs. 4 and 6.

II-B. Effects of Adsorbed Carbon Upon LaB₆ Surface Properties

One factor which has a strong effect upon measured electrical properties, such as work function, of RB₆ surfaces is the presence of surface contamination. Carbon has been found to be an especially tenacious surface contaminant, and we therefore spent considerable time investigating the nature and effect of submonolayer quantities of adsorbed carbon. In particular, the effects of carbon on the work functions of LaB_{5.74}(100), (110) and LaB_{5.86}(110) surfaces has been investigated. The LaB_{5.86}(110) sample had a small bulk carbon impurity which could be made to segregate preferentially to the surface by applying the proper heating sequence. The surface carbon layer could be removed by heating in oxygen.

The behavior of the surface carbon and oxygen concentrations in vacuum, measured by AES, are shown in Fig. 9 as functions of sample temperature for the LaB_{5.86}(110) surface with slight initial CO contamination. Data were taken after heating to successively higher temperatures, for 1 minute intervals (2 m.n. for the 1900 K point), and cooling to room temperature. The carbon coverage formed by bulk diffusion increases with extended heating in the range 1700-1900 K, to about twice the maximum value shown here, and cannot be removed except by heating in oxygen.

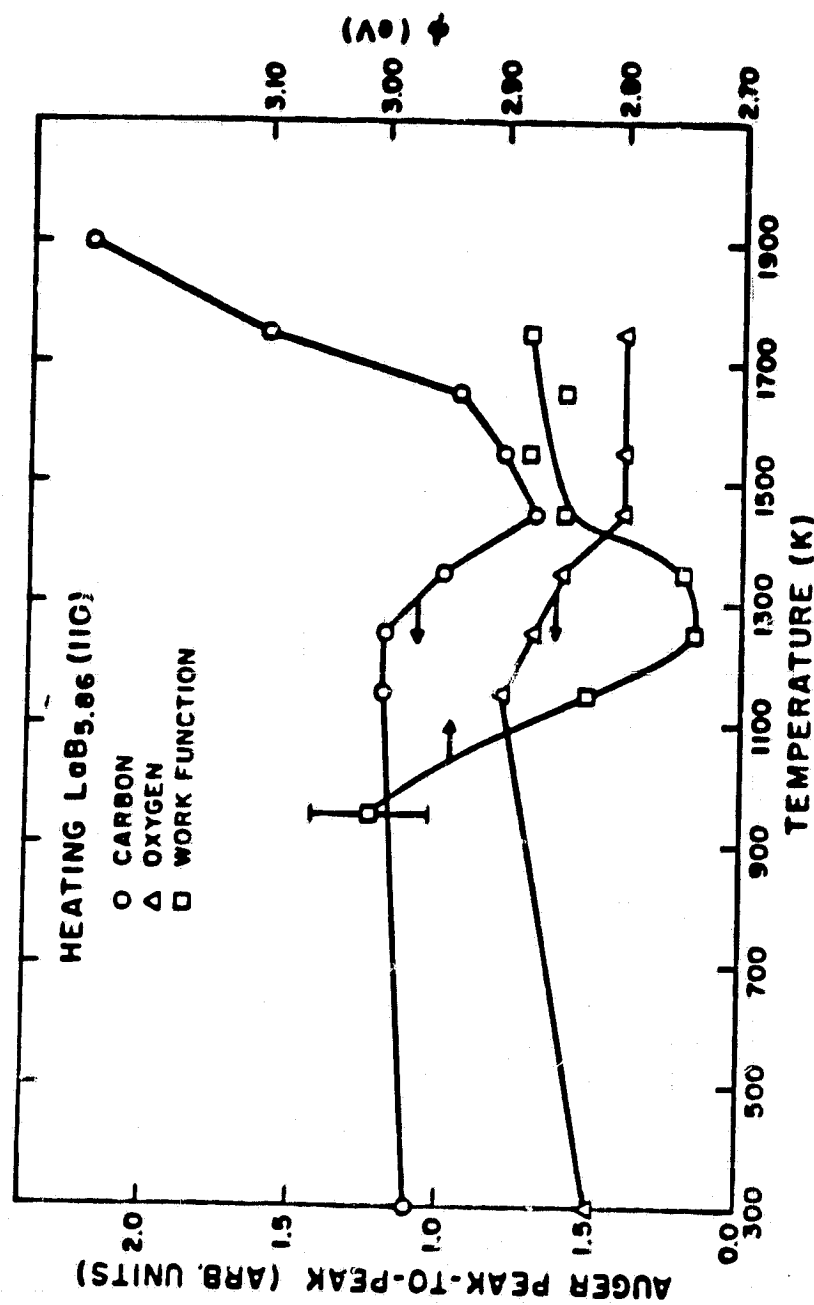


Figure 9. Evolution of the carbon Auger peak during heating of the LaB_{5.86}(110) sample, with initial slight CO contamination. The error bar indicates the uncertainty in FERP work function measurements.

The change in work function with temperature of the $\text{LaB}_{5.86}(110)$ crystal is also shown in Fig. 9. These ϕ measurements were made during a different heating sequence, with more heating in the temperature range below 1300 K. Thus, CO desorption and carbon diffusion are detectable at lower temperatures, shifting the work function curve to the left relative to the Auger curves. An increase in the corrected FERP work function of 0.1-0.2 eV is observed between the clean surface ($\phi = 2.75$) and the surface with maximum surface carbon segregation ($\phi = 2.9$ eV). The $\text{LaB}_{5.74}(110)$ sample, on the other hand, showed negligible surface carbon segregation after similar treatment. Previous studies on a $\text{LaB}_{5.74}(100)$ sample also showed negligible surface carbon segregation from the bulk.

The differences between the behavior of carbon in these samples cannot be explained by their initial bulk carbon contents. All three samples were prepared from crystals purified by three zone refinement passes, resulting in bulk carbon levels of ~ 0.0055 weight percent carbon (0.00092 C/La atom ratio).¹¹ The carbon contents were determined by combustion analysis of ~ 100 mg of material.

In a similar study of zone refined $\text{LaB}_6(100)$ surfaces, Oshima, et al.¹² reported formation of a surface carbon layer on a single zone refinement pass sample, while none was detected by AES on a triple pass sample. Bulk carbon was not detected in either sample studied by Oshima, et al., within the ~ 0.04 weight percent detection limit of the emission spectrography analysis method used. (This method is not as sensitive nor as accurate as combustion analysis.) Nevertheless,

those authors observed a graphitic carbon layer, estimated at 1-2 monolayers in thickness, on the single pass sample following several minutes heating of the initially clean surface at 1600-1900 K. The graphitic layer slowly converted to another form (apparently a surface carbide) during prolonged heating at 1200-1900 K, without loss of carbon. This latter form was found to be extremely stable, being apparently unchanged even during several hours heating at 1500 K in 5×10^{-6} torr oxygen. The effect upon work function of graphite or carbide layers on LaB_6 has not been reported by Oshima, et al.

We have not observed surface carbon of the magnitude described by Oshima, et al., nor have we had any difficulty in removing the carbon by heating at 1500 K in oxygen. Therefore, we believe that the bulk carbon concentration in our $\text{LaB}_{5.86}(110)$ sample is significantly less than that in the single pass sample they have studied. However, the quantity of carbon observed by AES on the $\text{LaB}_{5.86}(110)$ sample studied here is greater than that detected under the same conditions in earlier work on this sample. In addition, the carbon appears to be non-uniformly distributed over the surface, being highest near the edges and lowest in the center. The surface carbon can be reduced to undetectable levels by heating in oxygen, and the non-uniform surface distribution can be reproducibly re-established by subsequent heating to > 1600 K in vacuum. The apparent increase with time of the bulk carbon concentration, and its non-uniform distribution, as inferred from the surface segregation observations,

imply that carbon is being supplied to the sample from the TaC powder used to hold the sample in its molybdenum mounting sleeve. The larger $\text{LaB}_{5.74}$ samples, which have a shorter heating history, are mounted in similar fashion but as yet show no detectable increase in bulk carbon.

On the initially clean $\text{LaB}_{5.86}(110)$ surface we have observed a work function increase of approximately 0.15 eV for an estimated average surface-segregated carbon coverage of ~ 0.06 times the surface boron coverage, based upon tabulated Auger sensitivity factors.¹³ The uncertainty in this coverage assignment is large, but the absolute coverage of carbon in this case, corresponding to the maximum value we have observed, is of the order of .05 monolayer. A difficulty arises because the carbon layer is not uniform. Since the FERP beam probes a spot nearly 1 mm in diameter, the measured work function is only an average value. Nevertheless, we may conclude that even small levels of carbon contamination can cause significant increase in the $\text{LaB}_{5.86}(110)$ surface work function.

Previous evaluations of LaB_6 polycrystalline emitter material in thermionic converter tests¹⁴ did not show the low work function values measured in basic studies. However, hot-pressed polycrystalline LaB_6 like that used in those tests is known to contain significant bulk carbon contamination. Table II gives results obtained by Noack¹¹ for a typical lot of LaB_6 material powdered, hot pressed and after 1 and 3 zone refining passes. Note that the bulk carbon content

of the hot pressed polycrystalline material is more than thirty times that of the triple pass crystal. It seems quite likely that the poor showing of LaB_6 in thermionic tests is due to surface segregation of bulk carbon in the materials used.

Table II

CARBON CONTENTS OF DIFFERENTLY PREPARED LaB_6 SAMPLES

<u>Sample</u>	<u>Weight Percent Carbon</u>
LaB_6 powder (starting material)	.063
Hot pressed and electropolished polycrystalline material	.187
Single pass	.072
Triple pass	.0055

II-C. Cesium Adsorption and Cesium-Oxygen Coadsorption on LaB_6 (100) and (110) Surfaces

We have completed studies of cesium and cesium-oxygen coadsorption on a (100) oriented LaB_6 surface. Measurement of surface compositions, work functions and thermal stabilities of these layers were made using AES, FERP and TDS techniques. The AES and FERP results have been

compared with those of similar, previous measurements on a (110) LaB_6 surface.⁷

All measurements were performed in ultrahigh vacuum (2×10^{-10} torr). Oriented (100) and (110) crystals of triple zone-refined $\text{LaB}_{5.74}$ and $\text{LaB}_{5.85}$, respectively, were provided by Dr. J. Verhoeven of Ames Laboratory, DOE. Initial cleaning of the crystals consisted of annealing at temperatures up to 2000 K and/or heating at 1600 K in 10^{-6} torr of oxygen to remove trace amounts of carbon. Subsequent flashing to 1700 K was sufficient to remove all contaminants from the (100)-oriented crystal and all but trace amounts of carbon which diffused from the bulk to the surface of the (110) oriented crystal upon flashing.

Oxygen dosing was accomplished by admitting research grade (99.997%) oxygen into the chamber through a leak valve and pressure was monitored using a nude Bayard-Alpert ionization gauge. Cesium dosing was done using an SAES Getters source consisting of a finely divided mixture of Cs_2CrO_4 and silicon which when outgassed and heated resistively produces atomic cesium. The relative cesium flux was monitored using the quadrupole mass spectrometer which was located adjacent to the cesium source in the vacuum chamber.

Thermal desorption measurements were performed by heating the crystal with a programmable linear ramp current supply while the sample was situated in front of a 1.5 mm diameter aperture mounted on the entrance to the mass spectrometer. The proximity of the sample to the aperture caused the Re supports to be invisible to the

mass spectrometer ionizer, preventing detection of desorption products from the supports. Sample temperature was monitored using a W-Re thermocouple fastened directly to the crystal and calibrated pyrometrically in the temperature range 1000-2000 K. Due to the nature of the sample mount, heating rates were limited to a maximum of 32 K/sec.

When neutral cesium desorption spectra were desired, the crystal was biased at -30 V relative to the aperture in order to prevent desorbing ions from being collected. The ion spectra were obtained by biasing the crystal at +0.1 V relative to the aperture, turning the ionizer off, and adjusting the focus of the mass analyzer until the ion signal was maximized. By applying such a small voltage drop between the crystal and aperture (which were separated by ~ 1 mm), the field lines were such that only ions from the crystal were drawn into the analyzer. As a check, the ion desorption spectrum of the Re supports was measured and found to be substantially different from that of the sample.

II-C-1. Cs Adsorption on Clean LaB₆

Fig. 10 shows the work function and AES peak to peak signal strengths versus cesium dose time for the two crystals. Different cesium fluxes were used for the two surfaces. Separate adsorption-desorption experiments on the (100) surface have verified that the cesium AES signal is proportional to the quantity of cesium adsorbed. Thus, one may assume that a break in the cesium AES vs dose time curve represents a change in sticking coefficient. For both crystals, the

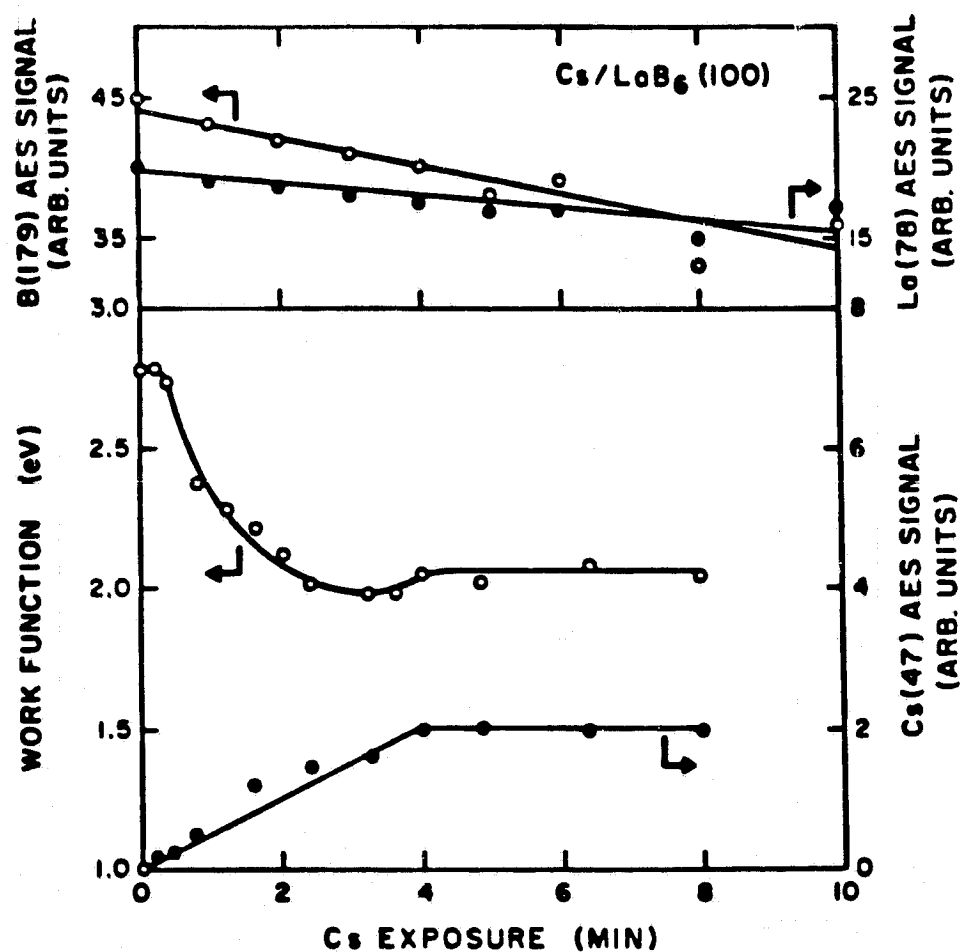


Figure 10(a). FERP work function, B(KLL, 179 eV), La(NOO, 78 eV) and Cs(NOO, 47 eV) Auger signal strengths vs Cs exposure for LaB₆(100).

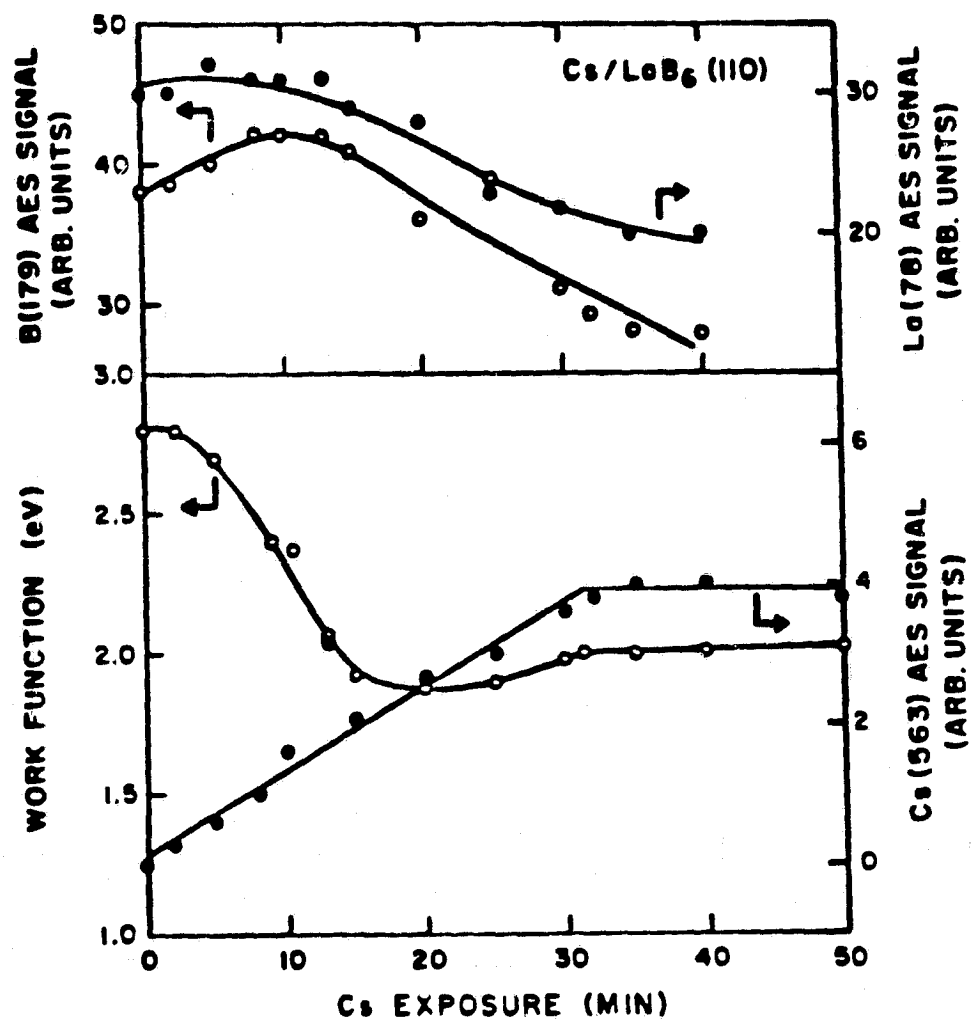


Figure 10(b). FERP work function, B(KLL, 179 eV), La(NOO, 78 eV) and Cs(MVN, 563 eV) Auger signal strengths vs Cs exposure for LaB₆(110).

slope changes discontinuously to zero indicating that the sticking coefficient goes to zero. Presumably, this point marks the filling of all available cesium adsorption sites. The corresponding independence of the work function on additional cesium exposure provides further support for this conclusion.

During cesium exposure, the work function drops from a clean-surface value of 2.78 eV to minima of 1.97 and 1.88 eV for the (100) and (110) orientations, respectively, and then rises to saturation values of 2.07 and 2.00 eV. Both crystals pass through their respective work function minima at $\sim 70\%$ of maximum room temperature cesium coverage. The attenuation of both La and B Auger signals suggests immobile adsorption in such a way that both kinds of atoms are covered or, more probably, sufficient mobility in the adlayer to mask both types of atoms from the Auger analyzer.

An unusual feature of the work function versus coverage curves is the nonlinear behavior near zero coverage. It can be seen from Fig. 10 that the cesium Auger signal increases significantly before the work function starts to decrease. This effect disappears, however, on both surfaces when a small oxygen underlayer is present. Taken at face value, this result suggests that the dipole moment per adatom approaches zero near zero coverage, a phenomenon which has not been observed on refractory metal surfaces. Work done on refractory metals suggests that the cesium adatom is significantly polarized or ionized by the surface. Moreover, cesium does not adsorb

with zero dipole moment until the surface density of cesium atoms is large enough to initiate lateral depolarization via dipole-dipole interactions. It is difficult to imagine a model in which cesium atoms would adsorb on an atomically smooth surface and not be polarized, apart from interaction within the adlayer. Therefore, we conclude that the nonlinear behavior of work function near zero cesium coverage is caused by an unusual interaction of initially adsorbed cesium with the surface, such as the filling of La lattice vacancies below the plane of electric neutrality.

It is interesting to note that the relatively small work function decrease caused by Cs adsorption is not entirely unexpected. Fig. 11 is a plot of minimum work function ϕ_m attained by Cs adsorption versus the initial surface work function ϕ_s for various metallic single crystal substrates. The oxygen-containing Zr/O/W(100) and oxygen-covered LaB₆(100) surfaces have been included for comparison. In an earlier study, Swanson and Strayer¹⁵ showed that the minimum work function attainable for a clean substrate-alkali adsorbate system could be described by

$$\phi_m = k_1\phi_s + k_2I_a \quad (3)$$

where ϕ_s is the clean substrate work function, I_a is the adsorbate ionization potential and k_1 and k_2 are empirically determined constants. The results in Figure 11, based on the most recent single crystal data, are not in disagreement with those earlier measurements.

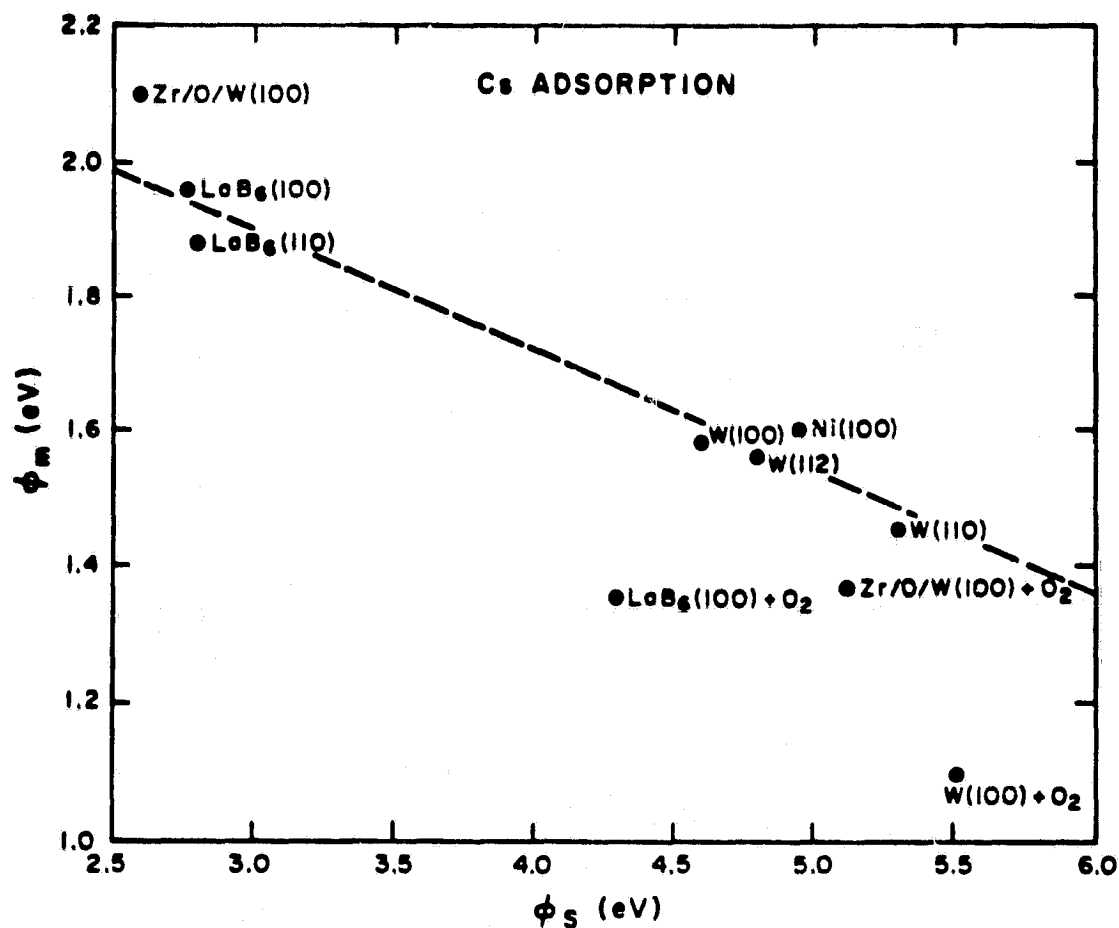


Figure 11. Minimum work function ϕ_m with cesium adsorption versus substrate work function ϕ_s . Data from the following sources: LaB₆(100), LaB₆(100) + O₂, Zr/O/W(100): this study; LaB₆(110): Ref. 7; W(100): Ref. 28; W(112): Ref. 24; Ni(100): Ref. 29; W(110): Ref. 26.

The effect of cesium adsorption upon the low energy electron reflection characteristics of $\text{LaB}_6(100)$ has also been investigated. The results, plotted in Fig. 12, show the following general behavior:

- 1) Structure is present in the region a few eV above the electron collection threshold, which probably corresponds to Bragg-type reflections. Similar structure has been observed for other $\text{LaB}_6(100)$ crystals⁷ and for the (100) faces of other RB_6 compounds.^{16,17}
- 2) The adsorption of successively greater amounts of cesium destroys the structure in the reflection spectrum and causes progressively larger electron reflection to occur.
- 3) The reflection scale is given in arbitrary units because of difficulty in determining the total current impinging upon the sample surface. Nevertheless, the relative changes during cesium adsorption are meaningful.

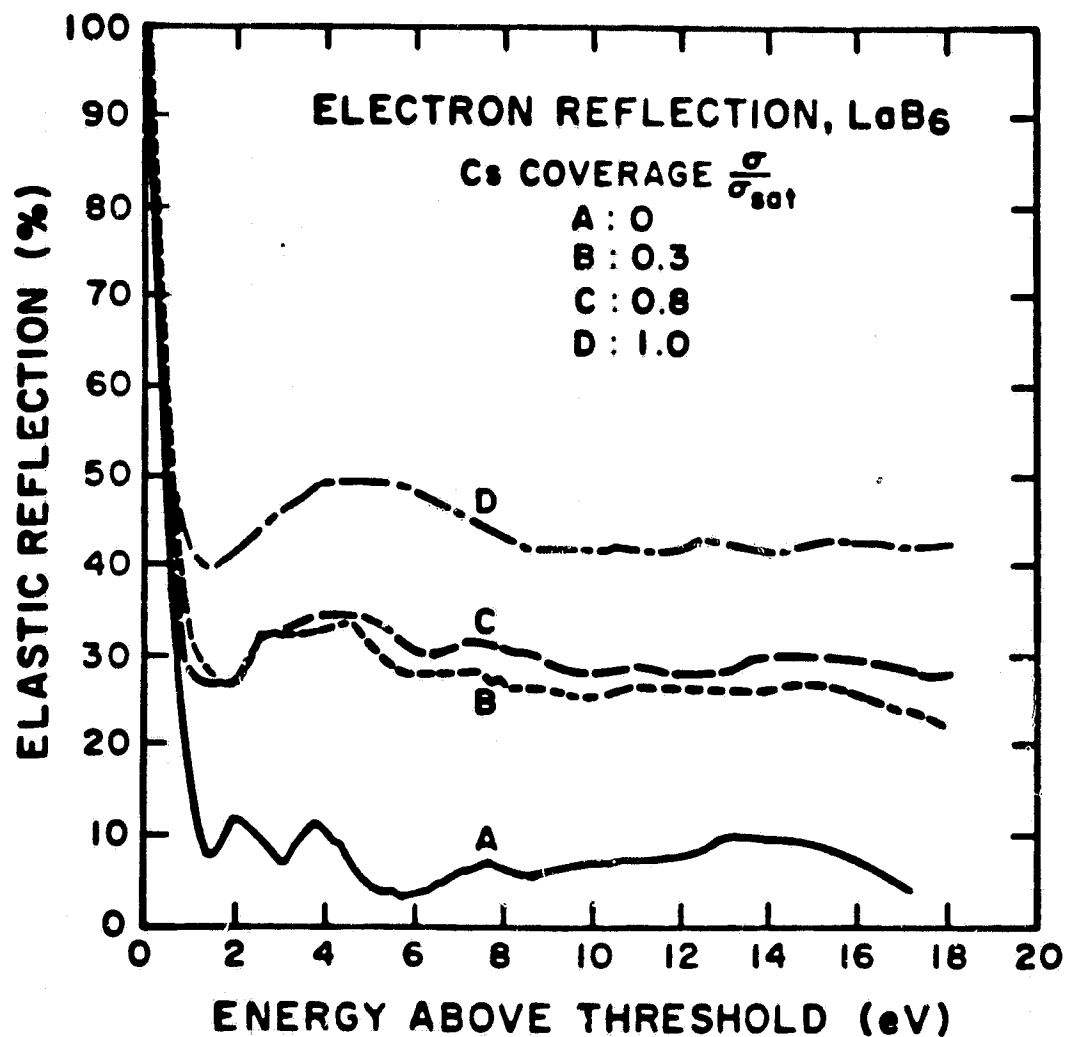


Figure 12. Elastic electron reflection ($V_{grid} \approx 8$ volts) from LaB₆(100) for various cesium coverages. The work functions for the various surfaces are: A, 2.78 eV; B, 2.28 eV; C (minimum), 1.97 eV; D (saturated), 2.06 eV.

II-C-2. Cesium Desorption from the Clean LaB₆(100) Surface

Fig. 13 shows thermal desorption spectra of cesium layers on clean surface as functions of coverage. Relative coverages were determined by using the Cs (MNN) Auger peak intensity dependence on cesium exposure as a measure of the quantity of cesium adsorbed and defining saturation coverage as the point at which the slope of the curve changes discontinuously to zero. Two discrete binding states and a continuum of states are clearly visible. Using Redhead's formulation of desorption kinetics,¹⁸ and assuming first-order desorption (the validity of which will be discussed later) with a pre-exponential factor of 10^{13} sec^{-1} , activation energies of desorption shown in Fig. 13 were calculated for the two discrete binding states. The low-coverage continuum is probably composed of a series of overlapping first-order desorption peaks, some which have coverage-dependent activation energies. This point will be discussed later.

The terminal desorption energy for the surface saturated with cesium prior to desorption is readily estimated using the following method. The desorption rate $R(t)$ at any time t is given by

$$R(t) = - \frac{d\sigma}{dt} = v_n \sigma^n \exp(-E/kT) \text{ atom-cm}^{-2} \text{ sec}^{-1} \quad (4)$$

where σ is the temperature dependent adsorbate coverage in atom-cm^{-2} , n is the order of the reaction, v_n is the rate constant for the reaction, k is Boltzmann's constant, E is the binding energy of the

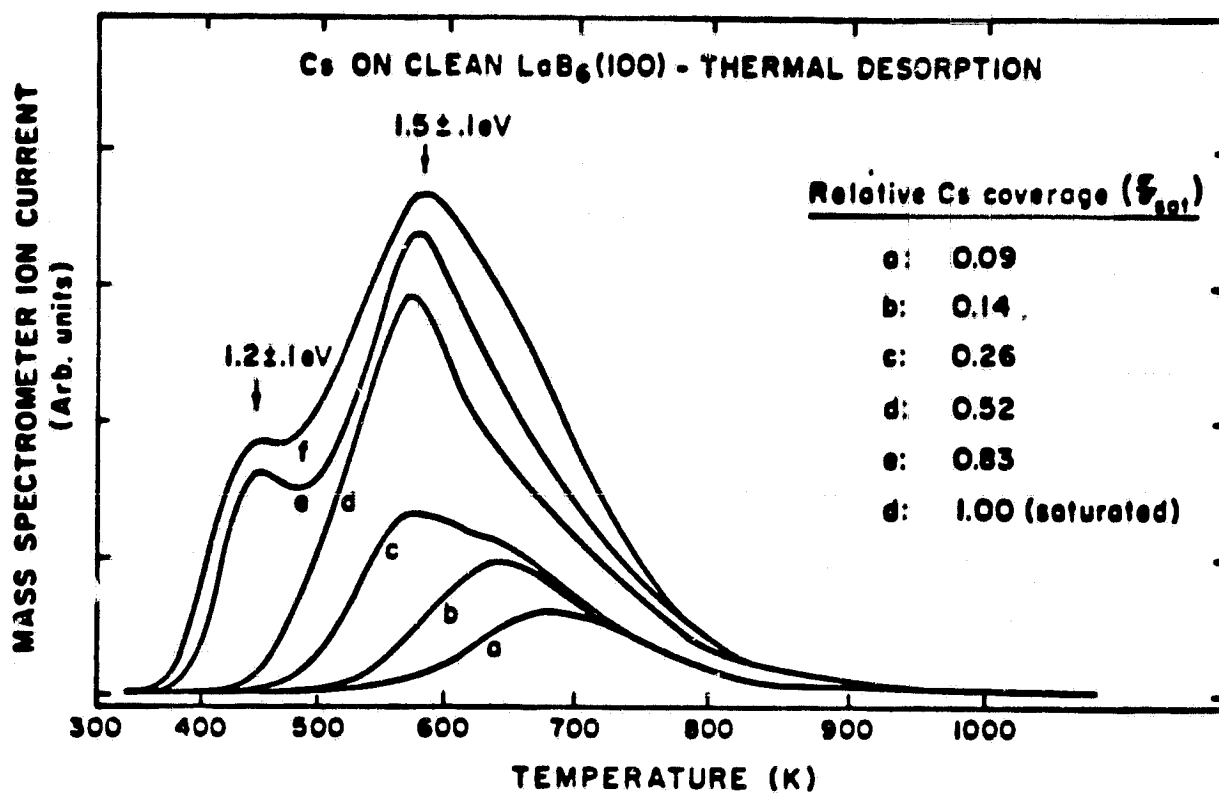


Figure 13. Thermal desorption spectra of neutral Cs from clean $\text{LaB}_6(100)$ as a function of Cs coverage relative to saturation.

adsorbed species and T is the temperature in degrees Kelvin. Assuming first-order kinetics, integration of equation (4) over a narrow coverage range ($\sigma_i \rightarrow \sigma_f$) yields, upon rearrangement,

$$\ln \ln \left(\frac{\sigma_i}{\sigma_f} \right) = -E/kT + \ln v_1 + \ln(\Delta t) \quad (5)$$

when Δt is the time interval over which the desorption takes place. If σ_i and σ_f are close in value and the time over which the desorption takes place is short, the left-hand side and the $\ln(\Delta t)$ term on the right-hand side of equation (5) can be neglected. Equation (5) then reduces to,

$$E \approx kT \ln v_1 \quad (6)$$

From Fig. 13, the terminal desorption temperature for the crystal saturated with cesium prior to desorption is 900 K which, when inserted into equation (6) yields a terminal desorption energy of ~ 2.3 eV, assuming $v_1 = 10^{13} \text{ sec}^{-1}$. Due to the fact that the work function of the surface is less than the first ionization potential of cesium throughout the full range of coverage, all cesium desorbs in the atomic state.

II-G-3. Oxygen Adsorption on $\text{LaB}_6(100)$ and (110)

In Fig. 14 we show the work function and AES signal intensity dependence on oxygen exposure for the (100) and (110) faces at room temperature. Unlike the cesium adsorption curves, the slope of the O(KLL) Auger signal does not change discontinuously with exposure but rather decreases gradually, indicating a continuous decrease in

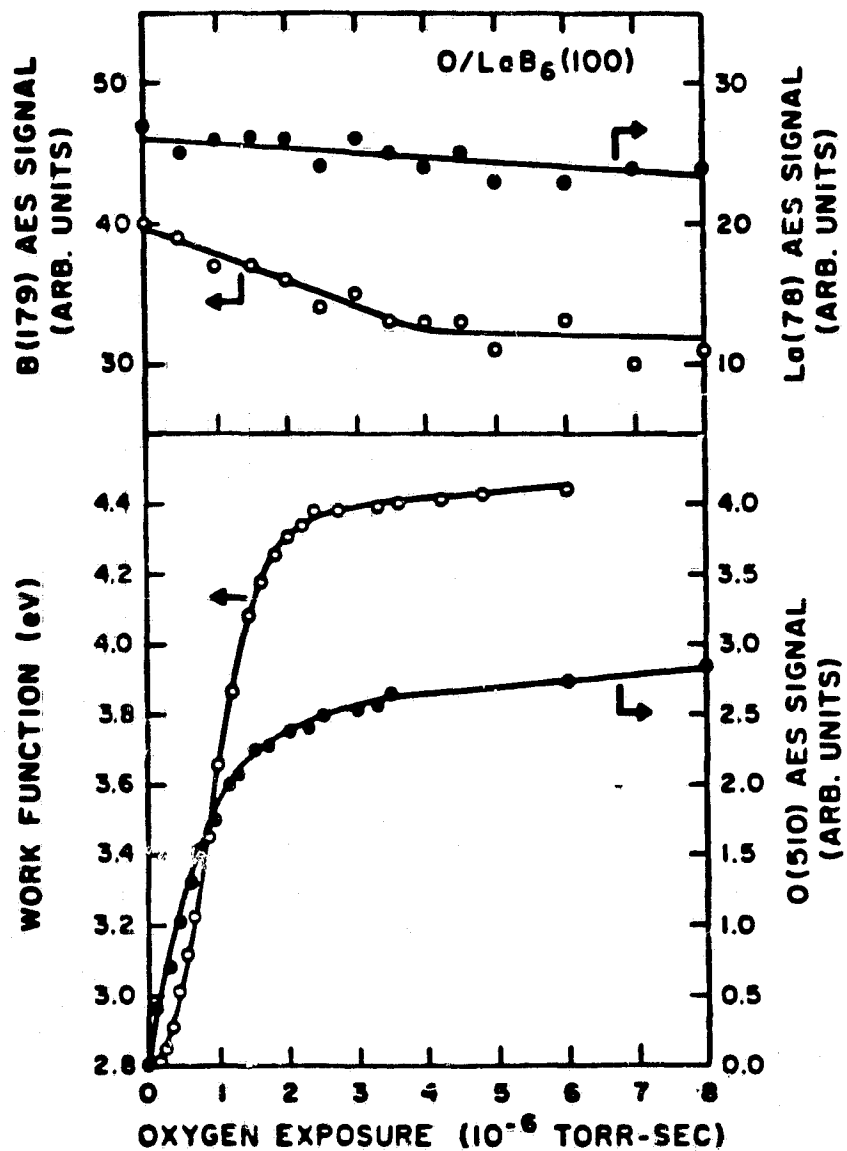


Figure 14(a). FERP work function, B(KLL), La(NOO) and O(KLL) Auger signal strengths vs oxygen exposure for $LaB_6(100)$.

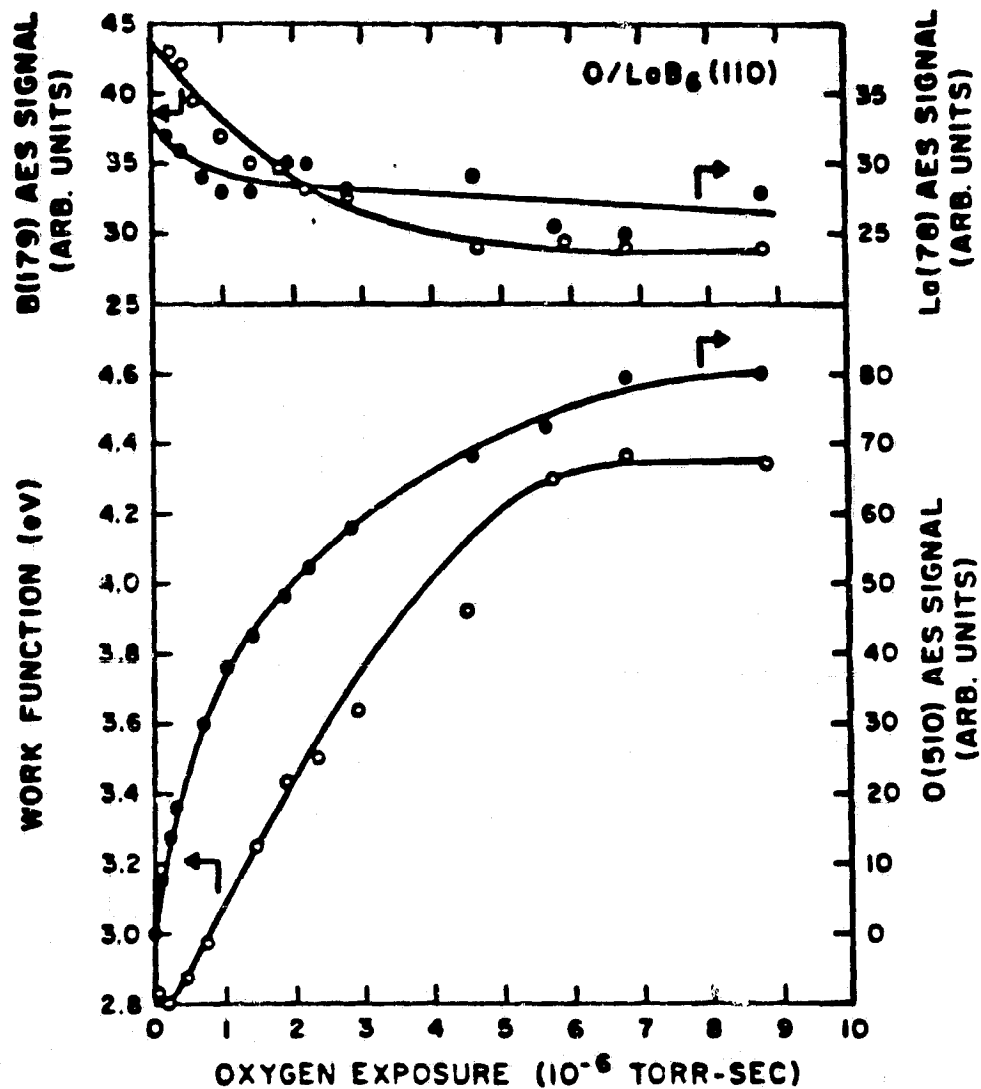


Figure 14(b). FERP work function, B(KLL), La(NOO) and O(KLL) Auger signal strengths vs oxygen exposure for $LaB_6(110)$.

sticking coefficient. The work function is observed to rise from a clean-surface value of ~ 2.8 eV to ~ 4.4 eV for both surfaces, representing a 1.6 eV increase. This result agrees reasonably well with previous work on the (100) surface.^{19,20} Saturation is indicated by a lack of change in the work function and O(KLL) Auger signal beyond certain exposures. The B(KLL) Auger signal is observed to undergo a considerably larger percent attenuation by adsorbed oxygen than is the La(NOO) signal for both crystal orientations throughout the entire range of exposure for which adsorption occurs. This result suggests that B sites are preferred over La sites for oxygen adsorption, as proposed earlier by Goldstein and Szostak¹⁹ and Nishitani et al.²⁰ Based on UPS results, the latter authors believe that B sites are preferentially occupied for exposures between 0 and ~ 1 L (at which point saturation of B sites allegedly occurs) and then La sites begin to be filled. Although the saturation of B sites at ~ 1 L exposure is not supported by the Auger data presented here, our AES peak shape analyses do show an enhanced splitting of the La(MNN) peak at exposures greater than ~ 1 L, indicating that La surface atoms are involved chemically in the binding of chemisorbed oxygen. This conclusion was also reached by Goldstein and Szostak on the basis of similar observations from the Auger spectra of the oxygen covered (100) surface.

As in the case of cesium adsorption, a curious nonlinearity in the work function vs oxygen exposure curves occurs for both crystals

at low exposures. As discussed earlier, this nonlinearity may be due to initially adsorbed oxygen atoms which fill lattice vacancies below the plane of electric neutrality and, therefore, do not affect the work function.

In Fig. 15, we have combined data found in Fig. 14 to plot the work function change vs relative oxygen coverage. According to the classical Helmholtz model, information on the dipole moment per adatom can be obtained from these plots. The work function change, coverage, and coverage-dependent dipole moment per adatom are related by the equation

$$\Delta\phi = -g\pi\sigma\mu(\sigma) \quad (7)$$

where g is either 4 or 2 depending upon the nature of bonding of the adsorbed atoms to the surface.²¹ At low coverages, dipole-dipole interaction is minimized, causing the polarization of adatoms to be due strictly to the substrate. In such situations, the behavior of the dipole strength per isolated adatom, μ_0 , can be deduced from the $\Delta\phi(\sigma)$ curves according to the equation

$$\mu_0 = -\frac{1}{g\pi} \left(\frac{d(\Delta\phi)}{d\sigma} \right)_{\sigma \rightarrow 0} \quad (8)$$

In light of these relationships, Fig. 15 implies that beyond the anomalous behavior of $\Delta\phi$ at low coverages, the oxygen dipole strength increases until $\theta = 0.5$ for both orientations and then remains constant until saturation. This conclusion is at odds with previous results reported for the (100) surface. Nishitani, et al.²⁰ report a linear

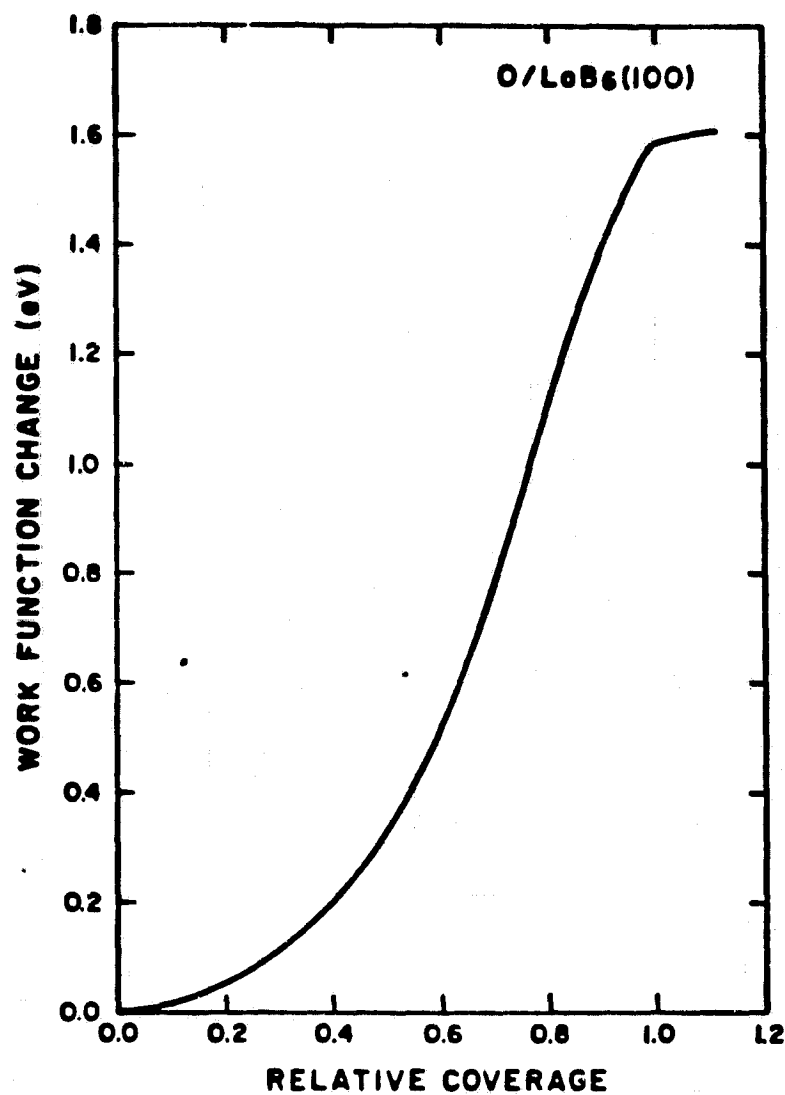


Figure 15(a). FERP work function change (relative to clean surface values) vs relative oxygen coverage for LaB₆(100).

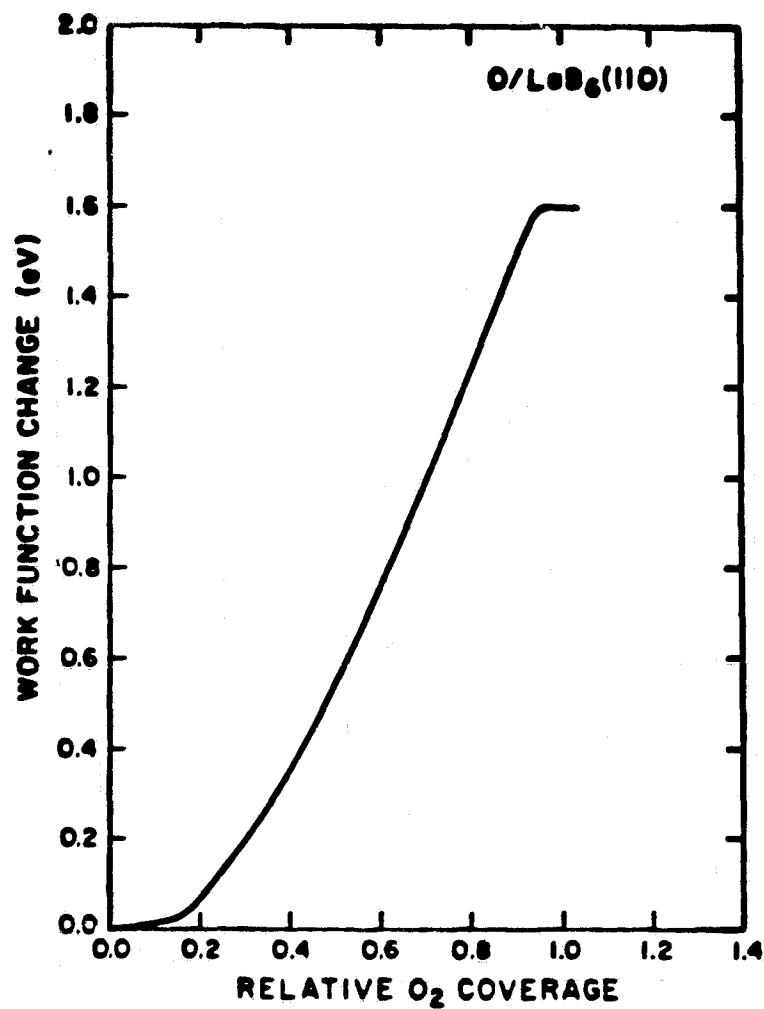


Figure 15(b). FERP work function change (relative to clean surface values) vs relative oxygen coverage for $\text{LaB}_6(110)$.

dependence of $\Delta\phi$ on coverage with a break to smaller slope at $\theta = 0.5$, suggesting a coverage dependence of the dipole strength opposite to that observed here. Goldstein and Szostak,¹⁹ on the other hand, report a constant linear dependence over the entire range of coverage. Although discrepancies exist in the low coverage ($\theta = 0 \rightarrow 0.5$) range, there is reasonable agreement on the dipole strength at higher coverages ($\theta = 0.5$ to saturation). Assuming that, at saturation, the oxygen density equals the unit cell density for the (100) orientation ($5.8 \times 10^{14}/\text{cm}^2$), the dipole moment per adatom at $\theta > 0.5$ is calculated to be 0.68, 0.50, and 0.65 D for the results reported in Goldstein and Szostak, Nishitani et al., and this work (Fig. 15(a)) respectively. It should be noted that on the basis of their conclusion that oxygen adsorbs to both La and B sites, Nishitani et al. actually assumed the surface oxygen density at saturation to be twice the value used here. However, for the purpose of normalizing the three sets of measurements, we have chosen a maximum oxygen surface density of $5.8 \times 10^{14} \text{ cm}^{-2}$ ($= a^{-2}$ where $a = 4.16 \text{ \AA}$, the LaB_6 lattice constant). The discrepancies at low coverage most likely result from:

- (1) the difference in dependence of the O(KLL) AES signal and O(2p) UPS signal on oxygen exposure between 0 and 1 L as seen by comparing Fig. 14(a) of this work with Fig. 3 of Nishitani et al.,
- (2) the nonlinearity in the $\phi(\theta)$ curve (Fig. 15(a)) reported here, and

- (3) the fact that Goldstein and Szostak do not show any data points in the first quarter of their $\phi(\theta)$ curve but simply extrapolate to zero coverage.

II-C-4. Coadsorption of Cesium and Oxygen onto LaB₆(100) and (110)

The effect of various amounts of preadsorbed oxygen on the work function and surface atomic composition dependence following cesium exposure is shown in Figs. 16 and 17. Based on Fig. 14, the oxygen doses used can be calibrated in terms of coverage (relative to saturation) by comparing the O(KLL) Auger signal at the exposure of interest to that at saturation. Thus, in terms of fractions of saturation coverage, the oxygen coverages used correspond to approximately 0.7 and 1.0.

Several interesting features emerge from these data. Despite the high initial ($\theta_{Cs} = 0$) work function caused by the oxygen underlayer, the subsequent minimum value achieved upon cesium adsorption is considerably lower than that observed for the clean surface. This observation is summarized in Table III. Also, as in the case of cesium adsorption on the clean surfaces, both La and B Auger peak intensities diminish with cesium coverage, suggesting localized chemisorption such that AES signals from both kinds of atoms are attenuated.

The presence of an oxygen underlayer causes a substantial increase in the amount of cesium that can be adsorbed before minimum

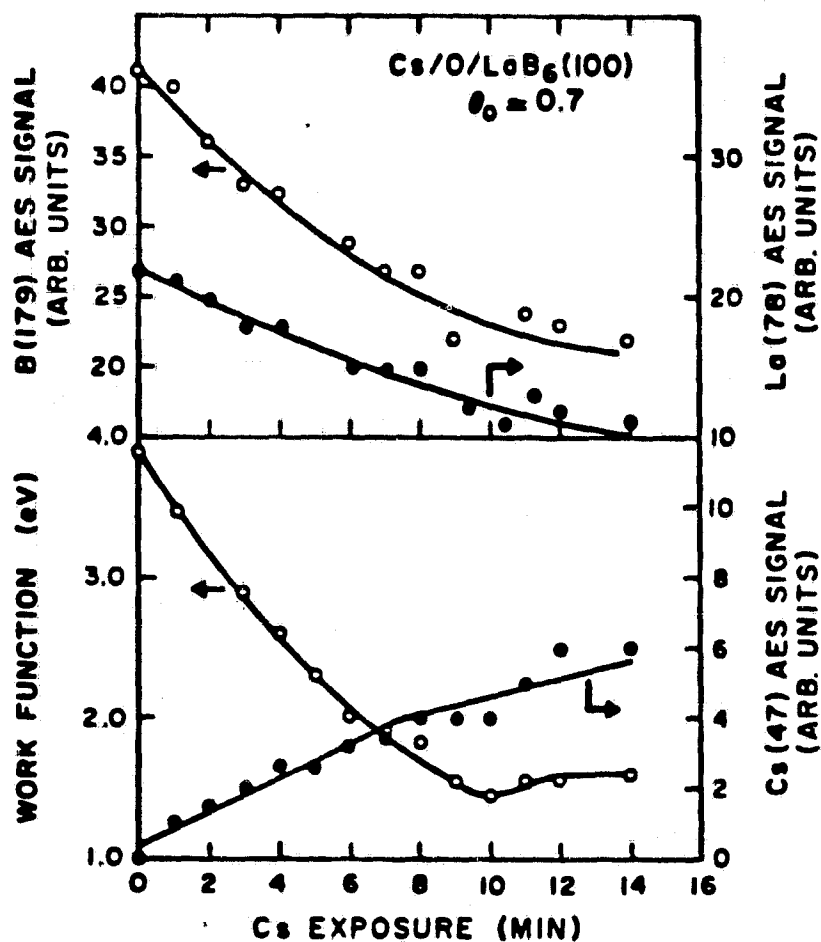


Figure 16(a). FERP work function, B(KLL), La(NOO), and Cs(NOO) Auger signal strengths vs cesium exposure time for relative oxygen precoverage of 0.7 on $\text{LaB}_6(100)$.

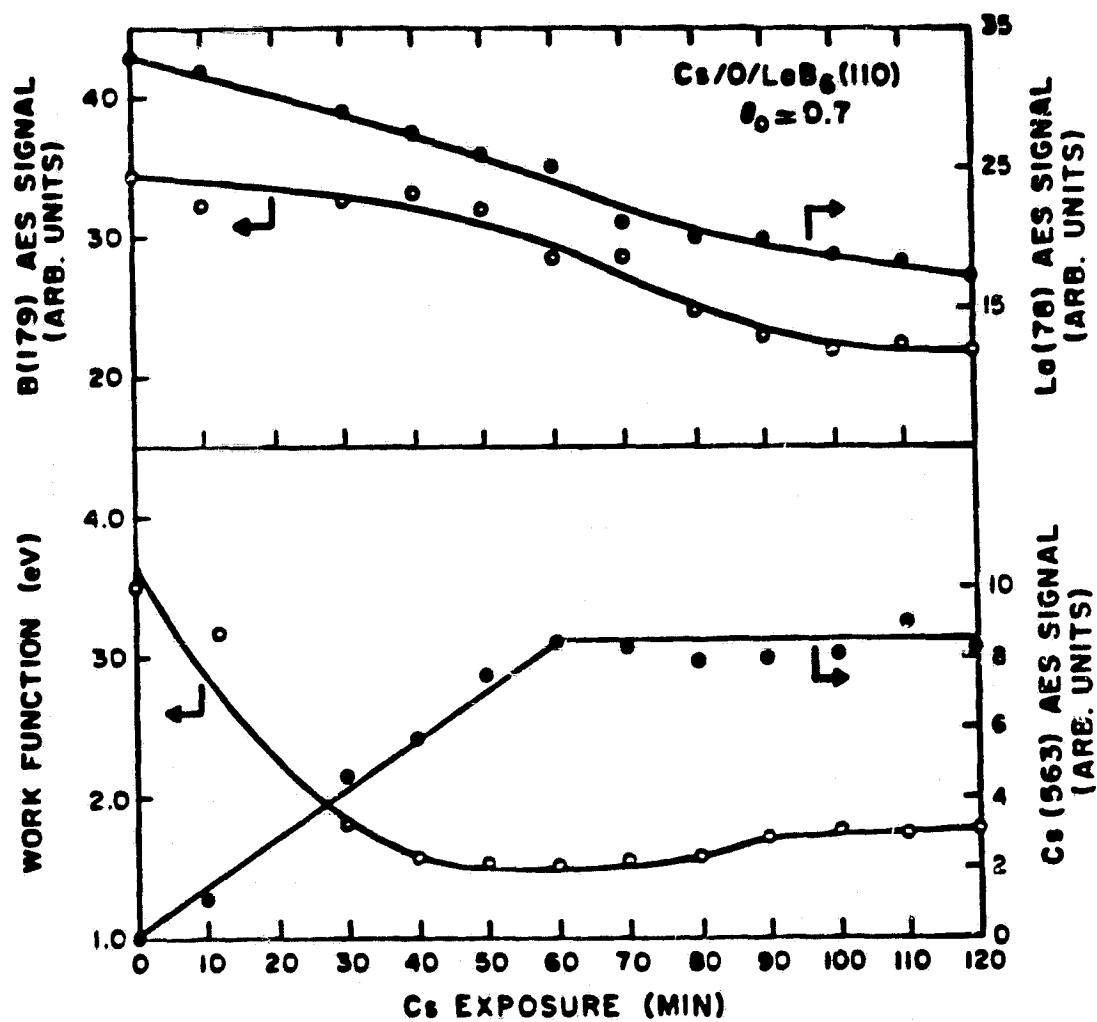


Figure 16(b). FERP work function, B(KLL), La(NOO), and Cs(MNN) Auger signal strengths vs cesium exposure time for relative oxygen precoverage of 0.7 on $\text{LaB}_6(110)$.

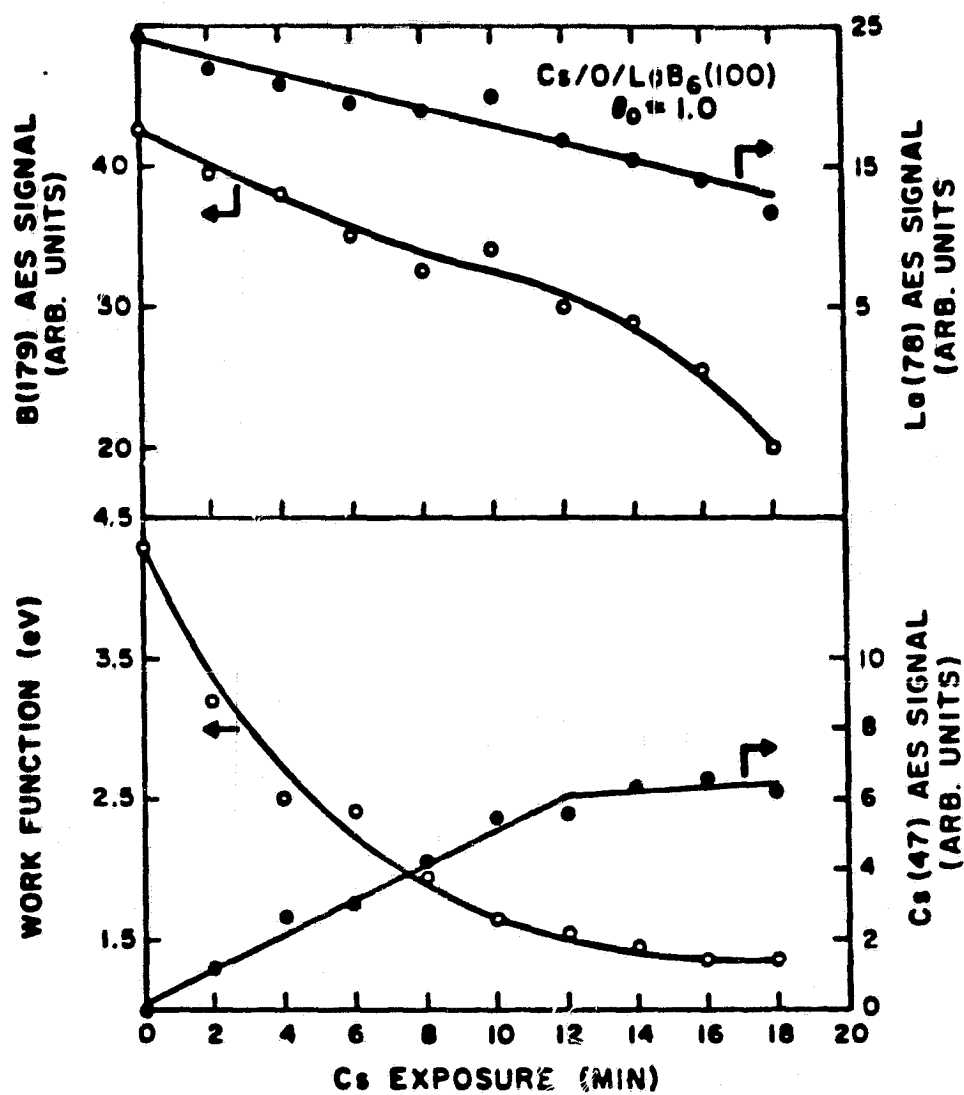


Figure 17(a). FERF work function, B(KLL), La(NOO), and Cs(NOO) Auger signal strengths vs cesium exposure time for relative oxygen precoverage of 1.0 on $\text{LaB}_6(100)$.

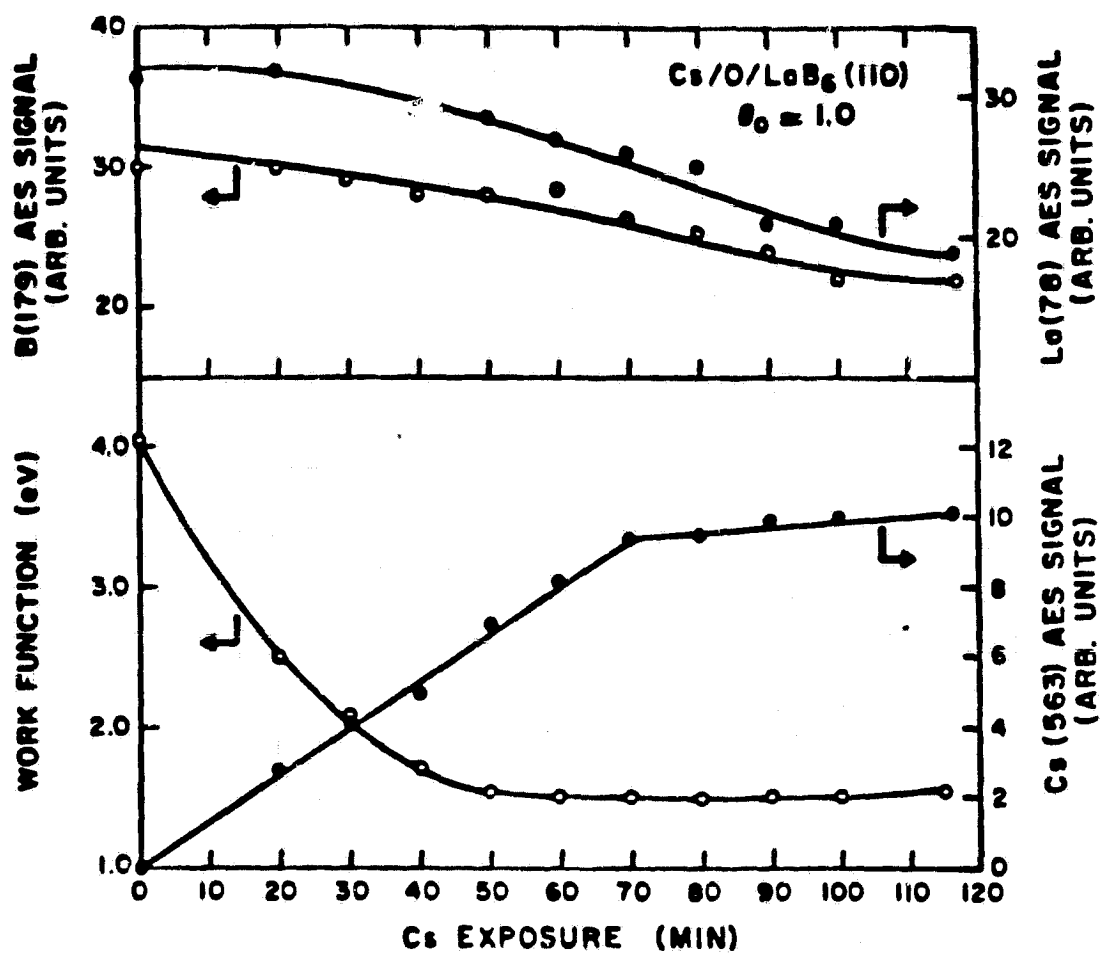


Figure 17(b). FERF work function, B(KLL), La(NOO), and Cs(MNN) Auger signal strengths vs cesium exposure time for relative oxygen precoverage of 1.0 on $\text{LaB}_6(110)$.

TABLE III

THE EFFECT OF PREADSORBED OXYGEN UPON THE FERP WORK FUNCTION
DEPENDENCE ON CESIUM COVERAGE: $\text{LaB}_6(100)$ and (110)

Oxygen Precoverage (Relative to Saturation)	ϕ Prior to Cesium Exposure (eV)*		ϕ_m Upon Cesium Exposure (eV)*	
	(100)	(110)	(100)	(110)
0	2.78(8)	2.78(8)	1.97(7)	1.88(5)
0.7	3.9(1)	3.50(6)	1.5(1)	1.49(7)
1.0	4.3(1)	4.08(7)	1.35(5)	1.47(6)

*The number in parentheses represents the uncertainty in the last digit.

work function is reached. This conclusion is supported as follows:

- (1) The cesium AES signal intensity vs dose time curves for the clean crystals (Fig. 10) show sharp breaks in slope at exposure times of 4 and 31 minutes for (100) and (110) orientations, respectively. However, when an oxygen underlayer is present, the cesium Auger signal continues to increase monotonically well beyond these exposure times before changing slope.
- (2) Inspection of Figs. 10, 16 and 17 shows that the cesium sticking coefficient during adsorption is independent of oxygen precoverage. Therefore, the shift to higher dose times at constant cesium flux before minimum work function

is reached indicates that the oxygen underlayer serves to increase the cesium density for both surfaces.

- (3) In Fig. 18, work function vs cesium AES signal is plotted for the surfaces with different amounts of pre-adsorbed oxygen. Inasmuch as saturation of the surface is characterized by independence of the work function on cesium exposure, the shift in the minimum work function value to higher cesium AES signal strength with oxygen precoverage seen in Fig. 18 is clear evidence of enhanced adsorption of cesium.

It is found that the presence of an oxygen underlayer results in enhanced ionic bond character of adsorbed cesium atoms near $\theta_{Cs} = 0$. According to equation (8), information on the dipole moment per isolated adatom can be deduced from the initial slope of the $\phi(\sigma)$ curve. Fig. 19 shows the work function change versus cesium exposure time for $LaB_6(100)$ with and without preadsorbed oxygen. As already discussed, the cesium sticking coefficient is independent of oxygen precoverage. Therefore, cesium coverage is proportional to dose time at the constant flux used here. Although the absolute dipole strength cannot be deduced because the absolute coverage is not known, it is clear from Fig. 19 that the presence of preadsorbed oxygen increases the dipole moment per cesium adatom by about a factor of 2. This result is consistent with a model of the surface in which cesium adatoms are directly bound to oxygen sites which comprise an ordered underlayer.

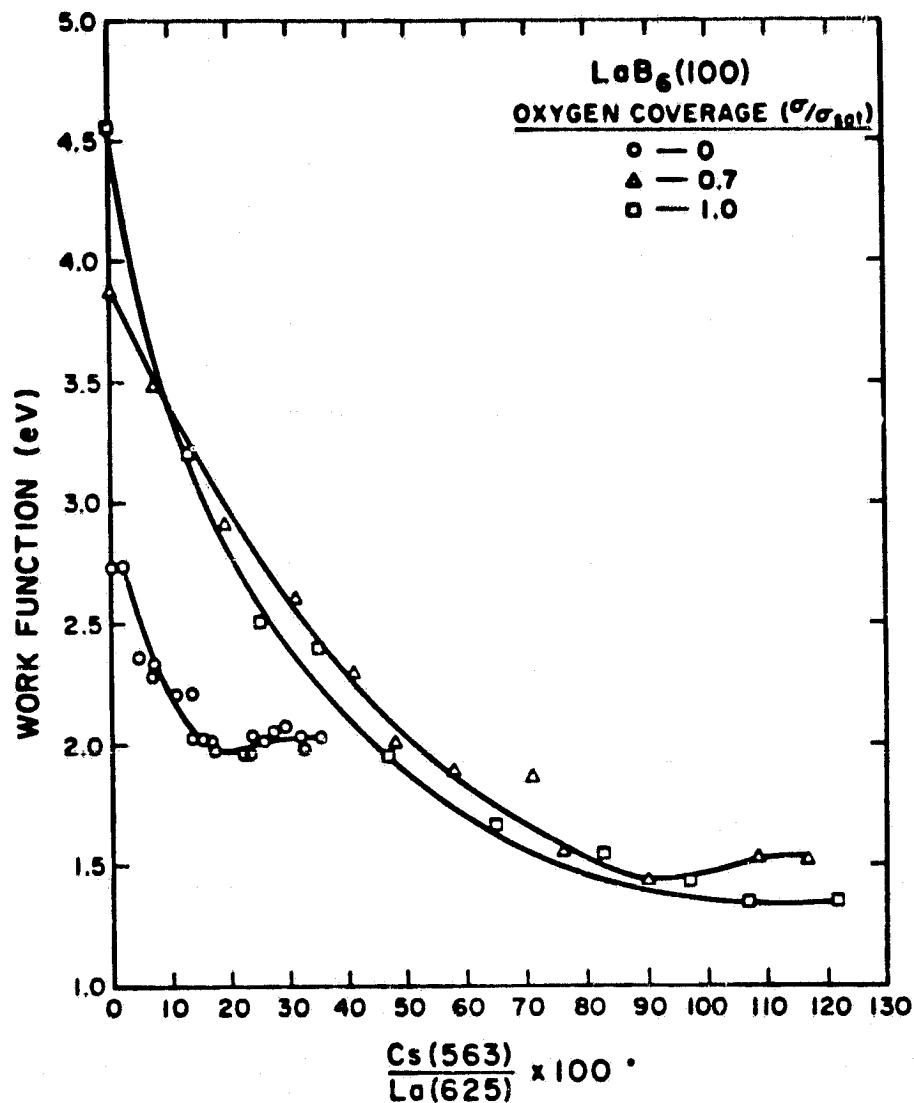


Figure 18(a). FERP work function vs Cs(MNN) Auger intensity for relative oxygen precoverages of 0, 0.7, and 1.0 on LaB₆(100). Figure 18(a) employs the Cs(MNN)/La(MNN) ratio because different primary beam currents were used for the different runs. The La(MNN) diminished by at most 27% during the course of cesium adsorption.

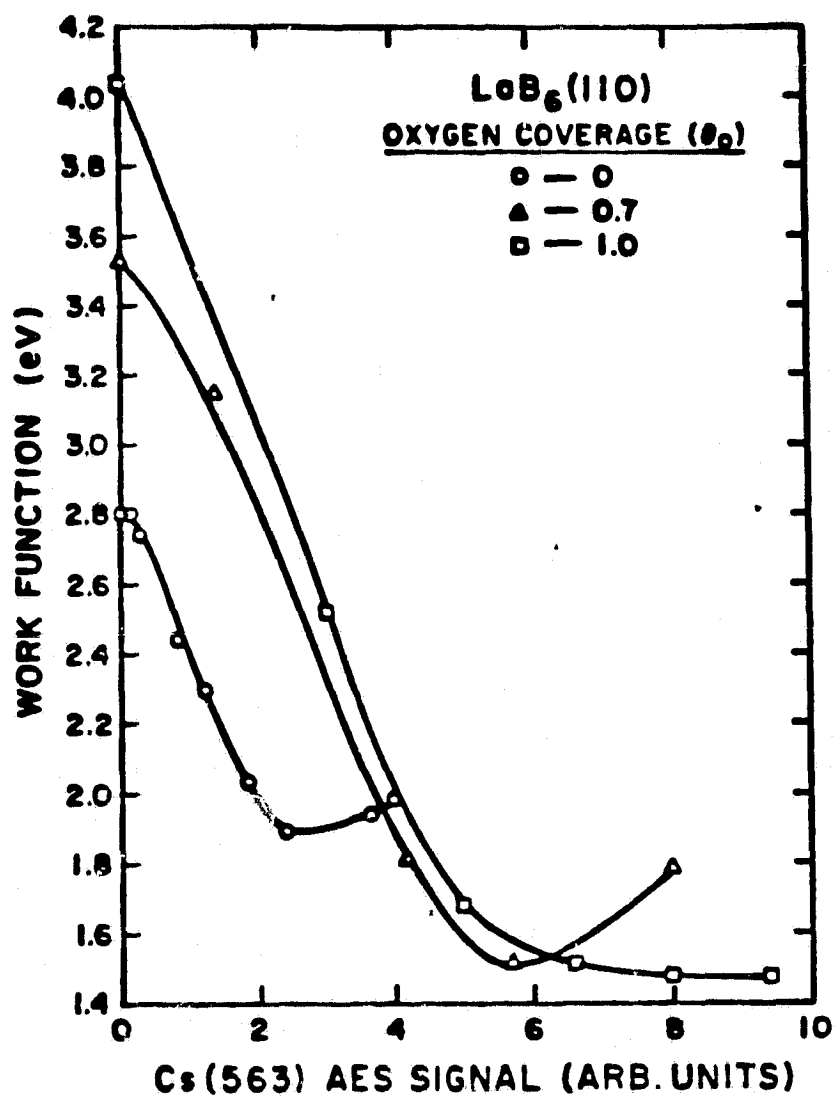


Figure 18(b). FERP work function vs Cs(MNN) Auger intensity for relative precoverages of 0, 0.7, and 1.0 on LaB₆(110).

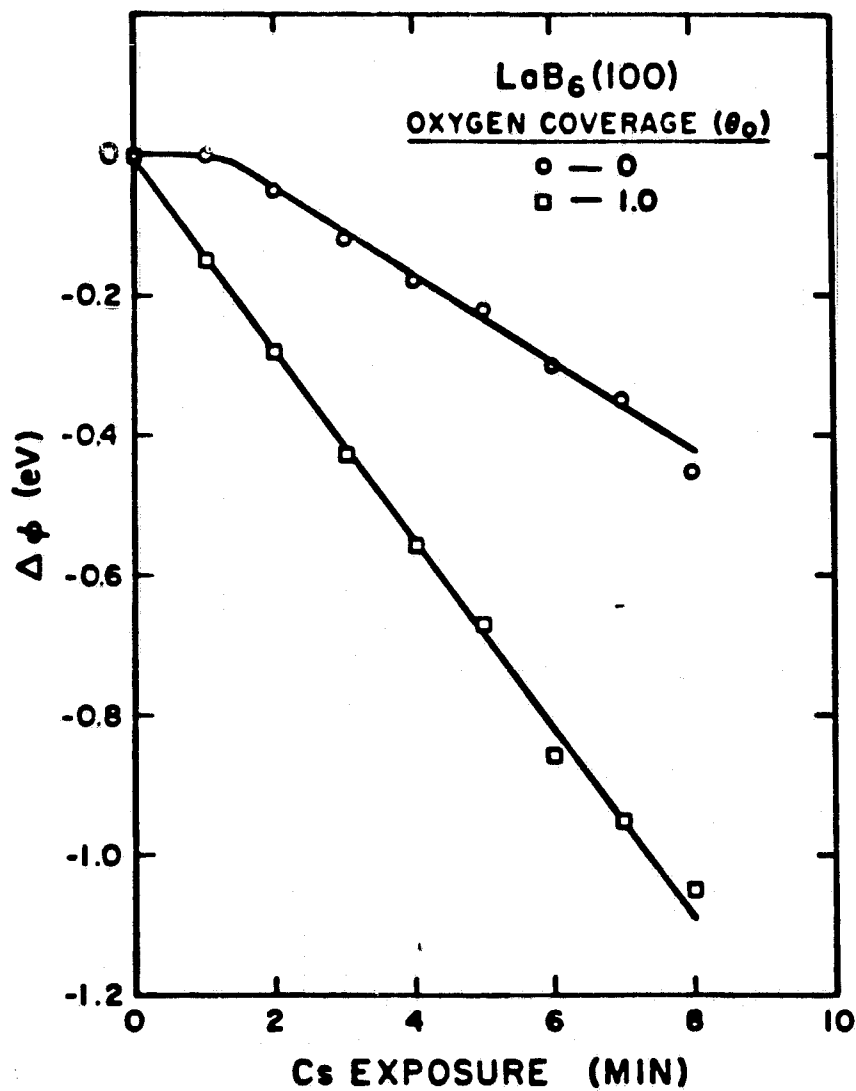


Figure 19. FERF work function change vs cesium exposure for $\text{LaB}_6(100)$ with ($\theta_o = 1.0$) and without preadsorbed oxygen.

II-C-5. Cesium Desorption from the Oxygen Covered $\text{LaB}_6(100)$ Surface

In Fig. 20, thermal desorption spectra for various amounts of cesium on the oxygen covered surface are shown. The sample was dosed at room temperature and the crystal was not heated after oxygen adsorption. As in the case of desorption from the clean surface, two discrete peaks and a continuum of peaks at low cesium coverage are present. The terminal desorption temperature is, however, shifted to a higher value (1200 K) as a result of oxygen precoverage. Using equation (6), a terminal desorption energy of 3.1 eV is calculated for cesium adsorbed on the oxygen saturated surface. Thermal desorption studies of oxide species from $\text{LaB}_6(100)$ have shown that B_2O_2 begins to desorb above ~ 1000 K.²² Therefore, significant changes are occurring in the oxygen layer in the temperature range over which cesium desorption takes place.

The energies of the two discrete states in Fig. 20 are equal, within experimental error, to those of the corresponding peaks in the clean-surface cesium desorption spectra (Fig. 13). Overall, the cesium desorption spectra with and without preadsorbed oxygen are quite similar with the exception of the 0.8 eV shift in the terminal desorption energy that results when oxygen is coadsorbed.

Fig. 21 shows the effect of varying the amount of preadsorbed oxygen upon the neutral cesium desorption spectrum. In each case, the same dose of cesium has been applied, a dose which is sufficient to saturate the surface at room temperature when no chemisorbed oxygen

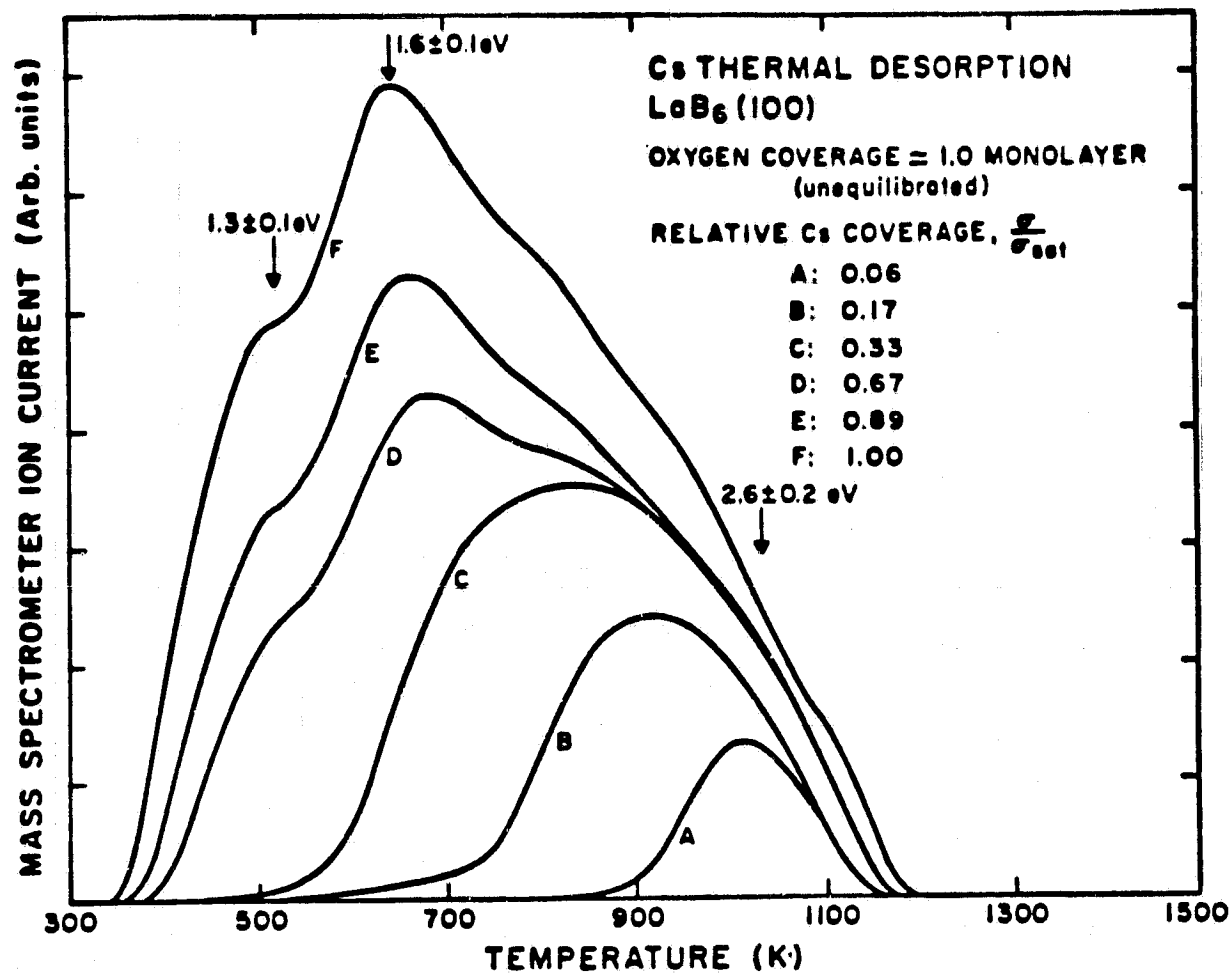


Figure 20. Thermal desorption spectra of neutral cesium from oxygen covered LaB₆ ($\theta_o = 1.0$) as a function of cesium coverage relative to saturation.

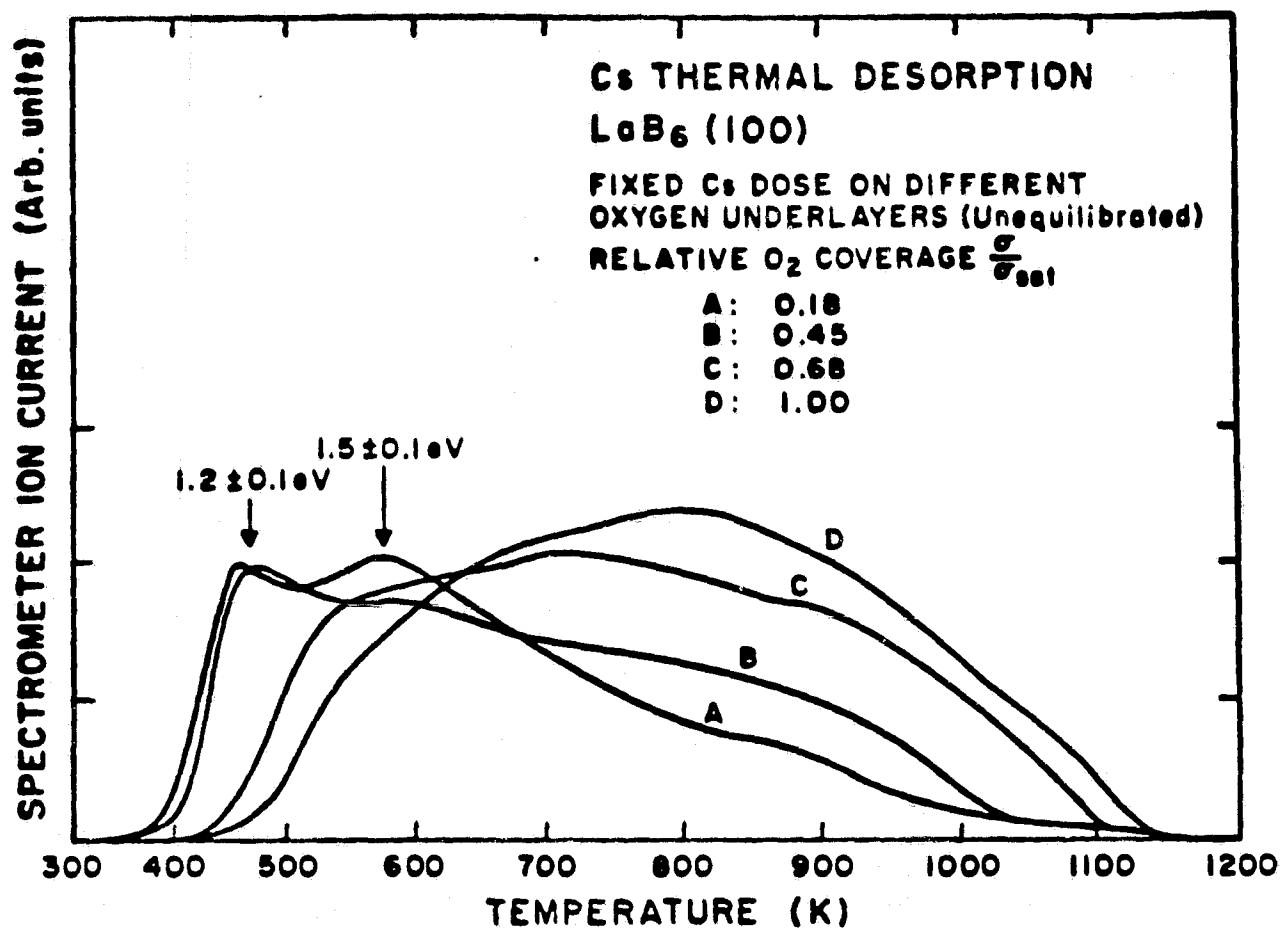


Figure 21. A thermal desorption spectra of neutral cesium from oxygen covered LaB₆(100) as a function of oxygen precoverage.

is present. Since the total amount of cesium applied is constant, the increase in number of adsorption sites caused by preadsorbed oxygen results in incomplete population of the lower energy binding states. Indeed, when the oxygen precoverage reaches saturation (curve D), the 1.2 eV state is not populated at all and the 1.5 eV state is only partially filled. Fig. 21 also shows that the terminal cesium desorption energy increases monotonically with preadsorbed oxygen coverage.

Heating the oxygen layer to 1400 K prior to cesium deposition causes an inversion in population of the two high-coverage states in the desorption spectra for saturation oxygen coverage and various amounts of cesium, i.e., the 1.3 eV state then binds more cesium than does the 1.6 eV state. However, the binding energies are unchanged by this preheating step.

Fig. 22 shows the desorption spectra of Cs^+ from the oxygen covered surface. Ion desorption can occur only if the work function of the surface is higher than the ionization potential of the adsorbed species, in accordance with the Saha-Langmuir equation. The surface saturated with oxygen possesses a work function of 4.3 eV and subsequent cesium adsorption reduces the work function to a value equal to the cesium ionization potential (3.87 eV) at a fractional cesium coverage of ~ 0.07 . Cs^+ desorption thus can be expected to occur at or below this cesium coverage. Indeed, no ion desorption is detected for relative coverages greater than 0.08.

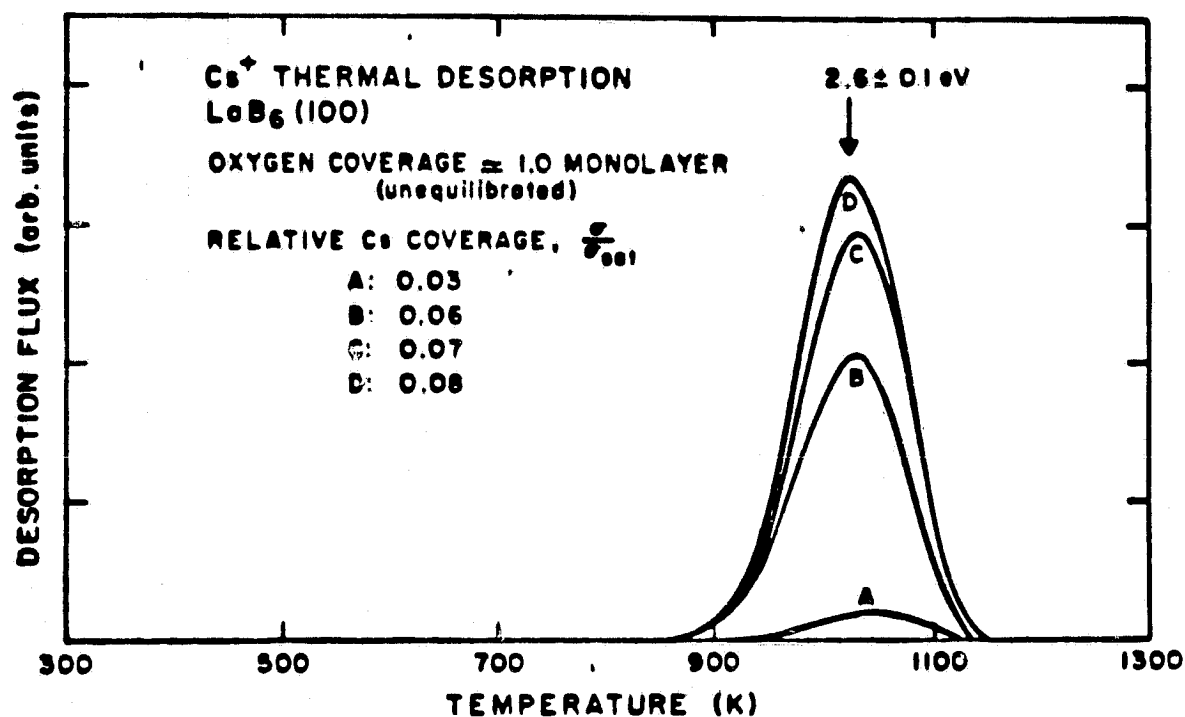


Figure 22. Thermal desorption spectra of Cs^+ from oxygen covered $\text{LaB}_6(100)$ ($\theta_o = 1.0$) as a function of cesium coverage relative to saturation.

Only one ionic binding state is observed and the activation energy of desorption remains constant at 2.6 eV over the range of coverage for which ion desorption can occur.

All the cesium desorption processes investigated here are governed by first order kinetics as we shall show in the following discussion. If we assume that the activation energy is independent of coverage, equation (4) can be differentiated to find the relationship between the temperature T_p at which the desorption rate is maximized and the activation energy of desorption. For a linear heating rate ($T = T_0 + \alpha t$), the general result is,

$$E = \frac{v_n n \sigma_p^{(n-1)} k T_p^2}{\alpha} \exp(-E/kT_p) \quad (9)$$

where the subscript p indicates evaluation at the peak desorption rate for a given binding state. From equation (9) it is evident that the peak temperature, (a) is independent of coverage for first-order reactions; (b) increases with increasing coverage for fractional order reactions; and (c) decreases with increasing coverage for second-order reactions. For zero order desorption equation (9) does not hold since the desorption rate (equation 4) increases monotonically with temperature.

Because of the fact that the associated peak temperatures are independent of coverage, the two discrete peaks in the neutral desorption spectra for the surface with and without oxygen as well as the ion peaks in the spectra of the oxygen covered surface are clearly

the results of first-order processes. The low-coverage continuum appears to come from three overlapping states centered at approximately 750, 700, and 650 K for the surface without adsorbed oxygen and 1000, 900, and 800 K for the surface with oxygen. A comparison of curves b and c from Fig. 13 shows that the state centered at ~ 650 K does not shift in position over the coverage range represented; by $\theta = 0.26$ (curve c), the 1.5 eV state has started to fill but is not yet so populated as to preclude identification of the 650 K state as a shoulder on the high-temperature side. Curves c through f in Fig. 20 show a similar pattern. The 800 K state is discernable as a shoulder on curves d, e and f and stands alone in curve c. For all four coverages, the binding energy is constant. Therefore, the 650 K and 800 K peaks in Figs. 13 and 20, respectively, result from first-order processes. Comparison of curves f, b, and a in Fig. 20 shows that the peaks at 950 and 1000 K (which are shoulders in curve f but are the main peaks in curves b and a) increase in energy only very slightly with coverage, suggesting that these peaks result from first-order desorption with coverage-dependent activation energies, rather than from fractional order processes. The same is probably true for the corresponding peaks in the clean-surface spectra.

An alternative method of calculating binding energy is available for the $\theta_{Cs} = 0.06$ spectrum (Fig. 20). Due to the fact that ion desorption occurs at this coverage, the Schottky equation can be utilized to calculate the desorption energy

$$E_N = E_I + \phi - I_p. \quad (10)$$

Here E_I and E_N are the ion and neutral desorption energies at a given coverage, ϕ is the work function of the surface at that coverage and I_p is the cesium ionization potential. The work function of the surface with 1.0 monolayer of oxygen and ~ 0.06 monolayer of Cs is 3.9 eV. Fig. 22 shows that the binding energy of ionic Cs at $\theta_{Cs} = 0.06$ is 2.6 eV. Insertion of these numbers along with the first ionization potential of Cs (3.9 eV) into equation (8) yields a calculated neutral Cs binding energy of 2.6 eV, which is shown in Fig. 20. Direct application of equation (9) yields the same result.

II-C-6. Comparison of Cesium-Oxygen Coadsorption on LaB₆ and W

The coadsorption properties of cesium and oxygen on tungsten have been reported for different crystal faces^{15,23-28} and provide a comparison for LaB₆. For both substrates, the presence of preadsorbed oxygen causes a work function increase relative to the clean surface value and a lower work function minimum upon cesium adsorption. This phenomenon has been interpreted in terms of increased ionic character of the cesium bond caused by the oxygen underlayer, resulting in a reduction of the surface electrostatic barrier, and hence, the work function. We have observed an increase in the cesium dipole moment by a factor of 2 as a result of oxygen preadsorption on LaB₆(100) whereas Desplat²⁵ reports a corresponding increase in the cesium dipole strength of 40% on W(100). However, the lowest work function

observed for the Cs/O/LaB₆ system (1.35 eV) still exceeds that observed for Cs/O/W (1.1 eV).

In contrast to LaB₆(100) and (110), the different crystal faces of tungsten do not show marked shifts of the minimum work function to higher cesium coverage as a result of oxygen preadsorption. Instead, the $\phi(\sigma_{\text{Cs}})$ curves for the different tungsten surfaces all go through minima and reach saturation values at approximately the same relative cesium coverages, regardless of whether oxygen is preadsorbed. LEED data from studies on W(112)²⁴ show that the saturation cesium density is increased slightly by the oxygen underlayer, as evidenced by a reduction in the nearest neighbor separation once the characteristic HCP pattern is achieved at saturation. However, the increase in cesium density with oxygen adsorption does not appear to be as marked on tungsten as it is on LaB₆.

The values of the saturation-coverage work functions of W(100)^{23,25} and W(110)²⁶ (but not W(112)) approach the bulk polycrystalline cesium value as oxygen precoverage becomes more extensive. This phenomenon indicates that a second cesium layer which is not strongly perturbed by the oxygen layer can be grown at room temperature and can achieve bulk cesium electronic properties. Moreover, a low-energy cesium binding state not present in the clean surface desorption spectrum has been observed for oxygen covered W(110),²⁶ lending further support to the notion of second layer cesium formation as a result of oxygen precoverage. Neither of these effects has been observed for oxygen preadsorption on LaB₆ surfaces.

VI-D. Evaluation of LaB₆(100) as a Cesium Vapor TEC Electrode Material

Using reasonable assumptions and a simple adsorption model, we have evaluated the usefulness of LaB₆(100) as an electrode material for nuclear electric propulsion (NEP) TEC applications. The (100) plane of LaB₆ appears to be the most stable, both in good vacuum and in background gas environments. Other planes tend to facet, forming (100) faces. The (100) surface also exhibits the lowest work function of any low index plane. Unfortunately, the clean LaB₆(100) work function is not low enough to meet the stringent requirements of NEP converter applications (10 A-cm⁻² at 1600 K, or effective emitter thermionic work function of 2.4 eV), which are determined by spacecraft specific power requirements. Therefore, some cesium adsorption would be required if LaB₆ were to be used in NEP converter applications.

The behavior of the work function ϕ and AES peak to peak signal with cesium dose on an initially clean LaB₆(100) surface has been shown in Fig. 10a. A separate set of adsorption-desorption experiments has verified that the cesium AES signal is proportional to the quantity of cesium adsorbed. Thus, if the break in the AES vs dose curve (Fig. 10a) corresponds to one monolayer of cesium (a reasonable coverage assignment), the dependence of work function on actual cesium coverage may be determined.

The effect of thermal equilibration of the oxygen layer at 1400 K is to evaporate boron oxides, changing the character of the surface. Independent studies of oxygen interaction with the (100) surface have shown that desorption of oxygen (as B_2O_2 and other species) occurs above ~ 1000 K and is complete at ~ 1650 K.^{6,22} At 1600 K, nearly all the oxygen has been removed. Thus, even though an adsorbed cesium layer has greater thermal stability on preadsorbed oxygen layers than on the clean $LaB_6(100)$ surface, the oxygen-covered surface itself is unstable at the desired operating temperature of a NEP emitter. Unlike cesium, oxygen would not be continuously readsorbed unless a non-zero oxygen pressure were intentionally maintained during converter operation. Consequently, oxygen adsorption is not a practical method of improving LaB_6 emitter cesiation in NEP thermionic converters. On the other hand, the oxygen layer is stable at collector operating temperatures (600-800 K). In what follows, we evaluate the clean and oxygen saturated $LaB_6(100)$ surfaces as practical emitter and collector, respectively, in NEP thermionic converters.

Table IV is a summary of work function and binding energy data measured in this study for various cesium coverages on clean and oxygen covered $LaB_6(100)$. To illustrate the method of electrode evaluation, we use the clean data to calculate the cesium flux required to maintain the emitter conditions (2.4 eV at 1600 K) required for NEP applications. For first order desorption, equation (4) can be written

$$R = \sigma \theta_{Cs} v_1 \exp(-E_d/kT_e) \quad (11)$$

where T_e is the emitter temperature, σ is the saturation (monolayer) coverage atom density (5×10^{14} atom-cm⁻² for Cs), θ_{Cs} is the fractional monolayer coverage, v_1 is taken to be 10^{13} sec⁻¹ and E_d is the cesium desorption energy at θ_{Cs} . From Table IV we see that, at $\phi = 2.4$ eV, $\theta_{Cs} = 0.2$ and $E_d \approx 1.5$ eV. Then $R = 1.9 \times 10^{22}$ atom-cm⁻² sec⁻¹. In equilibrium, the desorbing flux R must equal the incident flux times a factor $(1 - \theta_{Cs})$, the number of available adsorption sites, assuming the sticking coefficient is unity on available substrate sites and zero elsewhere. This flux may be related to the equilibrium cesium pressure in the converter by

$$\mu = p(2\pi mkT_{Cs})^{-1/2} \text{ (atom-cm}^{-2} \text{ sec}^{-1}) \quad (12)$$

where p is the cesium pressure (dyne-cm⁻²), m is the cesium atom mass (gram) and T_{Cs} is the cesium gas temperature (K). The pressure p is a function of the cesium reservoir temperature T_R , which we assume here to be equal to T_{Cs} , and is given by

$$\log_{10} p \text{ (torr)} = 0.3833.7 T_R + 6.949 \quad (13)$$

in the temperature range of interest.

Since

$$R = \mu(1 - \theta_{Cs}) \quad (14)$$

TABLE IV
DESORPTION ENERGIES AND WORK FUNCTIONS FOR
SELECTED CESIUM COVERAGES ON CLEAN
AND OXYGEN COVERED LaB₆(100)

θ_{Cs}^*	$\theta_{\text{O}_2}^*$	Cs E_d (eV)	ϕ (eV)
~ 0	0	$1.8 \pm 0.1^{**}$	~ 2.77
0.2	0	1.5 ± 0.1	2.4
0.8	0	1.2 ± 0.1	1.96^{\dagger}
~ 0	$.8^{\ddagger}$	$2.6 \pm 0.1^{**}$	~ 4.1
0.8	$.8^{\ddagger}$	1.3 ± 0.1	1.4
1	$.8^{\ddagger}$	1.3 ± 0.1	1.35^{\dagger}

* Coverage = $\sigma/\sigma_{\text{sat}}$.

**Terminal desorption energy.

\dagger Minimum work function attained by Cs adsorption.

\ddagger Unequilibrated O₂ layer.

we find that the required incident flux is 2.3×10^{22} atom-cm⁻² sec⁻¹, corresponding to a cesium pressure of 240 torr or $T_R = 840$ K. These values are outside the practical range for converter operation.

Similar calculations for idealized NEP converter collector conditions (1.4 eV at 700 K) show that the oxygen covered (0.8 monolayer O₂) LaB₆(100) would require a cesium pressure of 0.06 torr or $T_R = 470$ K. For comparison, we may use data of Desplat and

Papageorgopoulos²⁶ for single crystal W(110). Their results show a work function of 2.4 eV at $\theta_{Cs} = .27$, with a corresponding desorption energy of 2.3 eV. To meet NEP converter emitter requirements, we calculate a cesium pressure of 0.7 torr or $T_R = 540$ K. The corresponding collector conditions, with "2-D oxide" W(110) substrate, would require only $\sim 1 \times 10^{-11}$ torr ($T_R \approx 200$ K)! The collector calculations here involve the additional assumption that there are no evaporation products (except cesium) from the emitter surface which would change the character of the collector surface during operation.

The above calculations show that cesiated $LaB_6(100)$ has a higher minimum work function and lower thermal stability than, for example, W(110) at NEP converter electrode operating temperatures. On the other hand, recent studies of $LaB_6(210)$ ^{30,31} suggest that this surface could meet NEP converter emitter requirements in the uncesiated mode. Indeed $LaB_6(100)$ itself can easily supply 10 A-cm^{-2} at a temperature of 1800 K without cesium, making it an attractive candidate for advanced terrestrial converter designs.

III. Characterization of Refractory Alloys and Related Surfaces - Task B

Investigation of the surface properties of W-Zr and W-Hf alloys have been completed. Final measurements have been made on W-0.5% Zr, W-5% Zr and W-1% Hf samples, so that data on the set of samples (W-0.5% Zr, W-5% Zr, W-0.5% Hf, W-1% Hf, W-5% Hf) are now available. Both surface composition (AES) and work function (FERP and thermionic) measurements have been made.

The work function data are summarized in Table V. Note that there is some disagreement among values determined by the various techniques. Since the thermionic emission comes primarily from low work function surface regions, thermionic measurements are strongly weighted toward the low work function values. In particular, polycrystalline alloy Richardson plots yield small slopes (low ϕ_R) and correspondingly small pre-exponential values (A_R), suggesting that a small fraction of the total surface has low work function and dominates the electron emission. For thermionic converter applications, the effective work function ϕ_{eff} is the most reasonable value to use, since the emitted current density J may be derived directly from it. Table V shows the typical low emission current densities which could be obtained from representative alloy samples.

Surface composition measurements on W-Hf and W-Zr alloys are summarized in Table VI. Only the alloy elements and oxygen are indicated, although there is also contamination from other elements (primarily carbon). In general, contamination is small and does not vary systematically with bulk alloy composition. In earlier studies of the Zr/O/W(100) single crystal surface,⁵ we found oxygen to be intimately associated with the Zr. That phenomenon also appears here, with the normalized oxygen signal tending to follow the surface concentration of the minority alloying component (Zr or Hf). Note that, in the case of W-Zr alloys, even a bulk Zr concentration as low as

TABLE V

WORK FUNCTIONS OF W-Zr AND W-Hf ALLOYS

Sample	Retarding Potential ϕ_{FERP} (eV)	Effective Thermionic ϕ_{eff} (eV) @ 1600 K	J (A-cm^{-2}) @ 1600 K	ϕ_R (eV)	A_R ($\text{A-cm}^{-2}\text{-K}^{-2}$)
W-0.5% Hf	4.5 ± 0.2	3.9 ± 0.1	1.6×10^{-4}	2.65	0.016
W-1% Hf	4.7 ± 0.1	--	--	--	--
W-5% Hf	3.9 ± 0.1	3.8 ± 0.1	3.2×10^{-4}	3.27	2.0
W-0.5% Zr	3.6 ± 0.1	--	--	--	--
W-5% Zr	3.9 ± 0.1	3.62 ± 0.05	1.2×10^{-3}	--	--
Zr/W(100) ¹	$2.6 - 2.8$	2.9 ± 0.1	> 0.1	2.56	6

1. Data from Ref. 5.

TABLE VI

SURFACE COMPOSITIONS OF W-Zr AND W-Hf ALLOYS

Bulk Composition	(after heating at 1800-1900 K)		
	$\frac{\text{Zr}(147)^{1,2}}{\text{Zr}(147) + \text{W}(163/169)}$ (Z)	$\frac{\text{Hf}(1624)^{1,2}}{\text{Hf}(1624) + \text{W}(1736)}$ Z	$\frac{\text{O}(503)^{1,2,3}}{\text{W}(163/169)}$
W-0.5% Hf	-	9	.17
W-1% Hf	-	11	.18
W-5% Hf	-	24	.28
W-0.5% Zr	39	-	.37
W-5% Zr	41	-	.36
Zr/O/W(100) ⁴	26	-	.37

- 1) Relative sensitivity corrections made according to Ref. 13.
- 2) Numbers in parentheses indicate energies of Auger peaks used in calculation.
- 3) Oxygen peak normalized to tungsten peak. This is a relative value, to be used for comparison only.
- 4) Data from Ref. 5.

0.5% appears to drive the Zr surface concentration above the critical value observed for a properly activated, low work function Zr/O/W(100) single crystal surface.

One of the primary goals of the polycrystalline alloy studies was to determine the bulk alloy composition which would yield optimum surface segregation of the minority component (Zr or Hf). The criterion for optimum surface segregation is minimum surface work function. This criterion is difficult to apply because of surface crystalline anisotropy, which may influence both surface segregation and work function decrease. Even so, the data presented here allow some general conclusions to be made.

- 1) Surface segregation of zirconium is more favorable than surface segregation of hafnium for the same bulk composition.
- 2) To attain the optimum surface segregation of zirconium suggested by studies of the Zr/O/W(100) system (26%), a bulk zirconium concentration of less than 0.5% would be required.
- 3) The data suggest that the optimum hafnium surface concentration (24%) is obtained with a bulk alloy of W-5% Hf. This surface concentration is of the same magnitude as that observed for Zr on the low work function Zr/O/W(100) surface, and yields the lowest FERP and effective thermionic work functions of the hafnium alloys studied. However, studies of the Hf/O/W(100) optimum surface concentration

have not yet been done, so data are not available for that surface. It seems premature to predict optimum W-Hf alloy composition for low work function based upon Zr/O/W(100) data, especially since the surface segregation properties of W-Zr and W-Hf alloys seem to differ markedly.

The results imply that attainment of work functions in the 2.6 eV range may not be possible with polycrystalline alloys of the type W-Zr or W-Hf. Recent studies in other laboratories³² suggest that slight deviations from (100) orientation, even on single crystal W surfaces, cause dramatic increases in the minimum work function attainable with Zr and O adsorption. We therefore believe that the most productive basic studies are those performed on well characterized single crystal surfaces and have therefore continued to emphasize this type of research. For this reason, proposed studies on Mo-Hf and Mo-Zr alloys were not performed, with efforts being devoted instead to the investigation of adsorbates on the well-characterized Zr/O/W(100) surface.

IV. Effects of Adsorbates on Refractory Alloy Surface Properties - Task C

IV-A. Cesium Adsorption and Cesium-Oxygen Coadsorption on Zr/O/W(100)

Studies of cesium adsorption and cesium/oxygen coadsorption on the Zr/O/W(100) surface have been performed. The measurements were made in an ion-pumped chamber with ultimate pressure of 4×10^{-10} torr. Background gases were monitored with a quadrupole mass analyzer (QMA)

and consisted primarily of CO and H₂. The tungsten crystal was electropolished and its orientation was determined to be within 1° of the (100) face by Laue x-ray diffraction. The crystal was mounted so that it could be resistively heated to 1700 K or heated by electron bombardment to 2400 K. Sample temperatures were monitored by a W-5% Re versus W-26% Re thermocouple and were checked at high temperature with an optical pyrometer. Estimated uncertainty in quoted temperature values is ± 10 K.

Zirconium was supplied from a resistively heated W wire onto which Zr was melted.³³ The source could deposit reproducible doses of Zr with less than 1% O and 2.5% C in the adsorbed layer, as monitored by AES. Cesium and oxygen were adsorbed as discussed earlier for LaB₆.

The Zr/O/W(100) low work function surface (2.6 eV) was prepared by the following treatment:⁵ (1) Heat the W(100) crystal, onto which several monolayers of zirconium have been initially deposited, at 1500 K for 2 min. in 1×10^{-7} torr O₂. (2) Heat the crystal to 2100 K for 10 sec. in background pressure $< 2 \times 10^{-9}$ torr. The sample was cleaned of adsorbed residual gas by electron bombardment to 1900 K before each experiment.

The FERP gun was used to measure the absolute work function of the surface with the sample temperature below 400 K. The FERP gun was also used to measure the integral $I_c(V_c)$ curves from which electron reflection vs primary beam energy could be determined. AES measurements were made with a retarding field analyzer using primary

beam of 2000 eV energy and 18 μ A current. Modulation amplitudes of 4 V peak-to-peak (V_{pp}) for the Zr(147 eV), W(169/179 eV), O(510 eV) and of 5.2 V_{pp} for the O(510 eV) and Cs(563/575 eV) peaks were used.

In TDS, the neutral Cs mass 133 peak was monitored with the line of sight QMA, using a retarding field of ~ 20 V/cm to prevent Cs positive ion emission. The sample was heated to 1300 K in 35 sec. Due to non-linear heating, the heating rate dropped from 51 K/sec to 20 K/sec during this heating interval. This factor was considered in Cs desorption coverage and binding energy determinations.

IV-A-1. Cs Adsorption on Zr/O/W(100)

The work function change with Cs adsorption on the low work function Zr/O/W(100) surface is shown in Fig. 23. The minimum work function obtained is $\phi_m = 2.12$ eV. This curve has a shallow minimum, leading to a saturation value $\phi_s = 2.16$ eV. A plot of Cs Auger peak-to-peak amplitude vs Cs adsorption time is linear with a break in slope around 24 min. indicating, if unity sticking coefficient is assumed, that it takes 24 min. to develop one monolayer Cs coverage on Zr/O/W. Interestingly, the O_2 Auger amplitude is unchanged during Cs adsorption.

The change in work function with heating temperature of an initially Cs saturated surface of Zr/O/W(100) is shown in Fig. 24. The sample was heated for 1 min. intervals to successively higher temperatures ranging from 350 K to 1000 K. The FERP work function was measured after the sample cooled below 400 K. Gradual

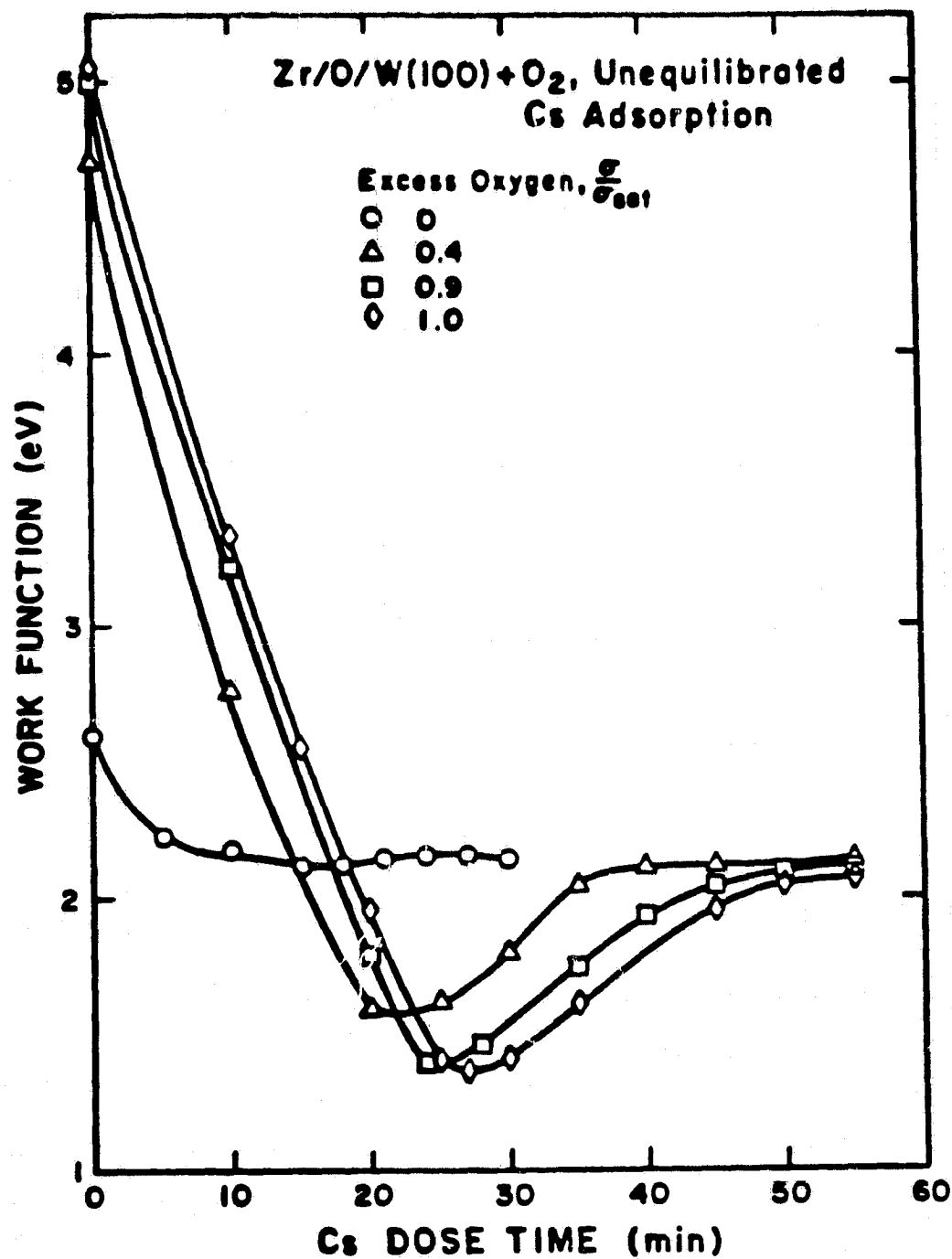


Figure 23. Work function versus dose time for cesium adsorption on Zr/O/W(100) with and without unequilibrated excess oxygen layers. Excess oxygen coverages based upon Auger data.

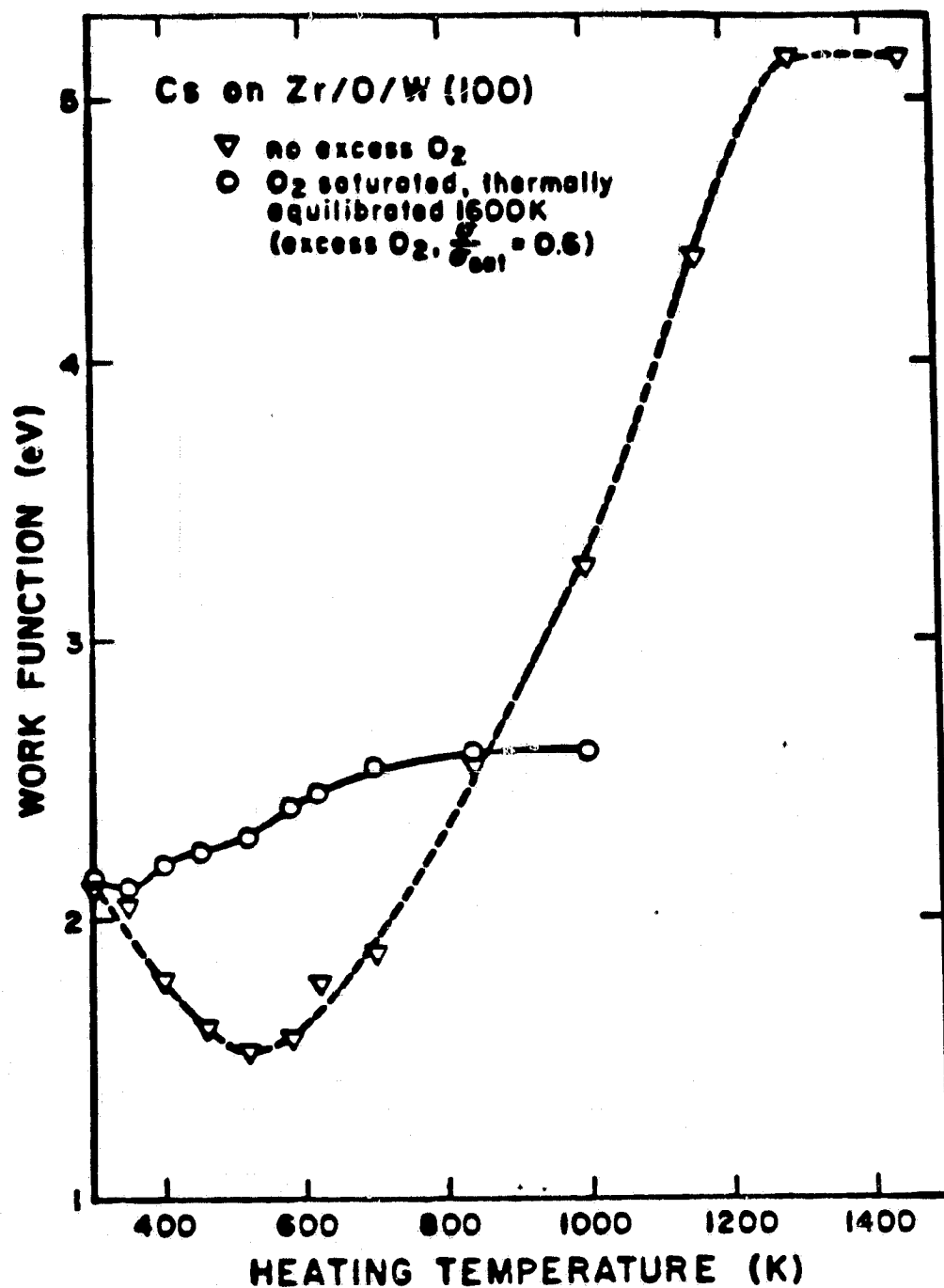


Figure 24. Work function versus desorption temperature for an initially saturated cesium layer on Zr/O/W(100) with and without a thermally equilibrated oxygen layer. Measurements were made at $T \leq 400$ K after 1 min heating at each temperature.

desorption of Cs from this saturated Cs layer caused an initial lowering of work function to 2.12 eV, which is the same minimum observed from Cs adsorption on Zr/O/W(100). Further desorption of Cs increased the work function. Heating to > 900 K yielded the work function of the original Zr/O/W(100) surface. These results suggest a reversible adsorption/desorption process.

Neutral Cs desorption spectra are presented in Fig. 25, as a function of the fractional cesium coverage $\theta_{Cs} = \sigma/\sigma_{sat}$. The amplitudes of these curves have been corrected for the nonlinear sample heating rate. The curves show that as θ_{Cs} increases, the high energy desorption peak shifts slightly to lower temperature, implying that the binding energy of Cs in this state is weakly coverage dependent. Nevertheless, the desorption energies were calculated assuming first order desorption through Redhead's equation,¹⁸

$$E = kT_p [\ln(v_1 T_p / \alpha) - 3.64] . \quad (15)$$

Here T_p is the peak desorption temperature in degrees Kelvin, α is the instantaneous heating rate at $T = T_p$ and a pre-exponential factor $v_1 = 10^{13} \text{ sec}^{-1}$ is assumed. The two major desorption peaks occur at 445 K and 552 K, corresponding to binding energies of $1.1 \pm 0.1 \text{ eV}$ and $1.3 \pm 0.1 \text{ eV}$, respectively. Fig. 25 also shows that Cs desorption is complete at 900 K which is consistent with the behavior of work function vs heating temperature of the initially saturated Zr/O/W(100) surface (Fig. 24).

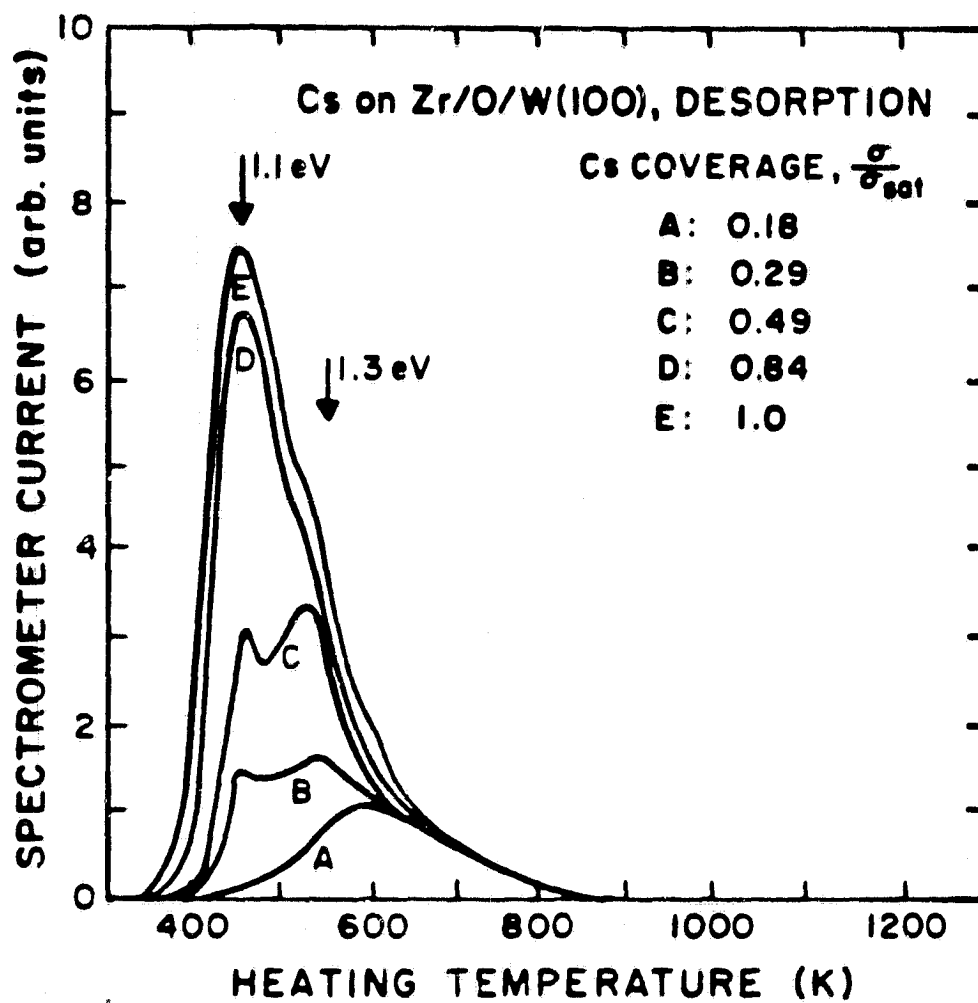


Figure 25. Thermal desorption of cesium from Zr/O/W(100), for various initial coverages.

IV-A-2. O₂ Adsorption on Zr/O/W(100)

Fig. 26 shows the work function and O₂ Auger signal changes for adsorption by exposure of the Zr/O/W(100) surface to 1×10^{-8} torr O₂ at room temperature. The work function increases rapidly with O₂ exposure up to 0.6 L, then levels out and reaches a final value around 5.3 eV. The O₂ Auger signal also increases rapidly in the initial exposure range from 0.3 L to 0.9 L and levels out at higher O₂ exposures. After 0.9 L O₂ exposure, the sticking coefficient of O₂ drops significantly, and the surface is essentially saturated. The Zr/O/W(100) surface with "excess" O₂ is produced by the above O₂ dosing procedure. The surface may then be heated to 1600 K for 2 min. in vacuum. We refer to the O₂ treated surface before heating as unequilibrated and after heating as thermally equilibrated.

We have studied the adsorption of Cs onto the Zr/O/W(100) surface covered with various amounts of excess O₂, both thermally equilibrated and unequilibrated.

IV-A-3. Cs-O₂ Coadsorption on Zr/O/W(100)

The change of work function with Cs adsorption on unequilibrated excess O₂ layers on the Zr/O/W(100) surface is shown in Fig. 23. The work function minimum is reduced from 2.12 to 1.37 eV. Compared with Cs on Zr/O/W(100), the excess O₂ surfaces have lower work functions at saturated Cs coverage, higher saturated Cs coverages, and the work function minima are shifted to higher Cs coverages.

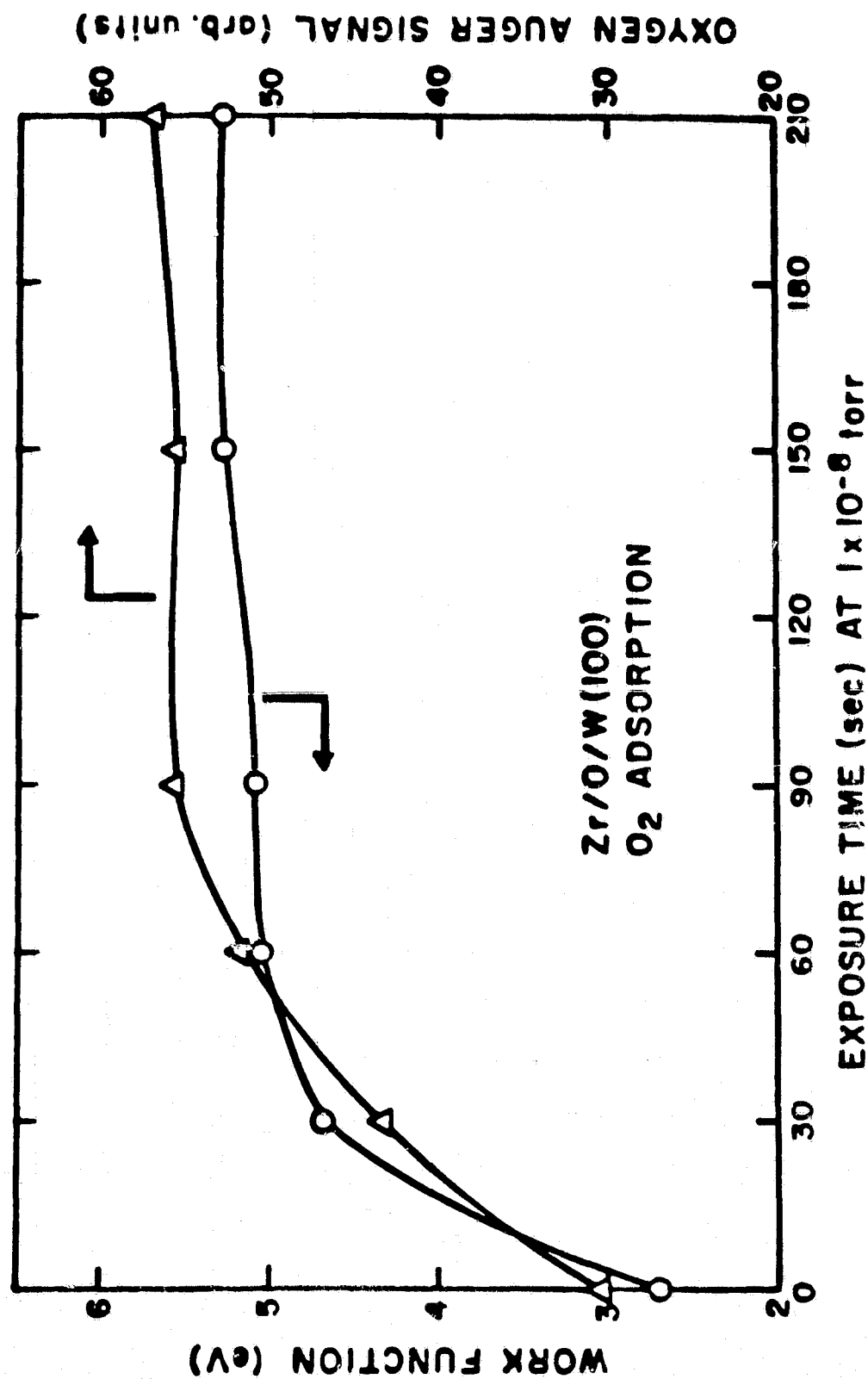


Figure 26. Work function and oxygen Auger peak-to-peak amplitude increase during room temperature oxygen adsorption on Zr/O/W(100).

The primary effect of thermal equilibration of excess oxygen layers at 1600 K for two minutes is a reduction in the total amount of oxygen and slight reduction in the amount of zirconium at the surface as determined by AES. The net effect upon Cs adsorption is the same as adsorbing less oxygen initially. Fig. 27 illustrates the strong effect of excess O₂ coverage on the minimum work function attained by Cs adsorption. Data for both thermally equilibrated and unequilibrated O₂ layers fall on the curve.

Cesium thermal desorption from equilibrated and unequilibrated surfaces is also strongly affected by excess O₂ coverage. Fig. 28 presents several desorption spectra showing increased energy (higher temperature) binding states compared to surfaces without excess O₂ (Figure 25). Note that curve B of Fig. 28, corresponding to lowest O₂ coverage, exhibits the lowest terminal desorption temperature and predominance of low energy binding states.

The adsorption of excess O₂ greatly increases the amount of Cs which may be adsorbed. For example, a plot of Cs Auger amplitude vs Cs dose time on the O₂ saturated, thermally equilibrated surface (excess O₂ $\sigma/\sigma_{\text{sat}} = 0.6$) is linear, and shows a sharp break in slope (corresponding to saturation coverage) at 45 min. This surface thus requires approximately twice as much Cs to develop saturation coverage as does the Zr/O/W(100) surface without excess O₂, assuming unity sticking coefficient in both cases. In contrast to the constant O₂ Auger signal observed during Cs adsorption on the low work function

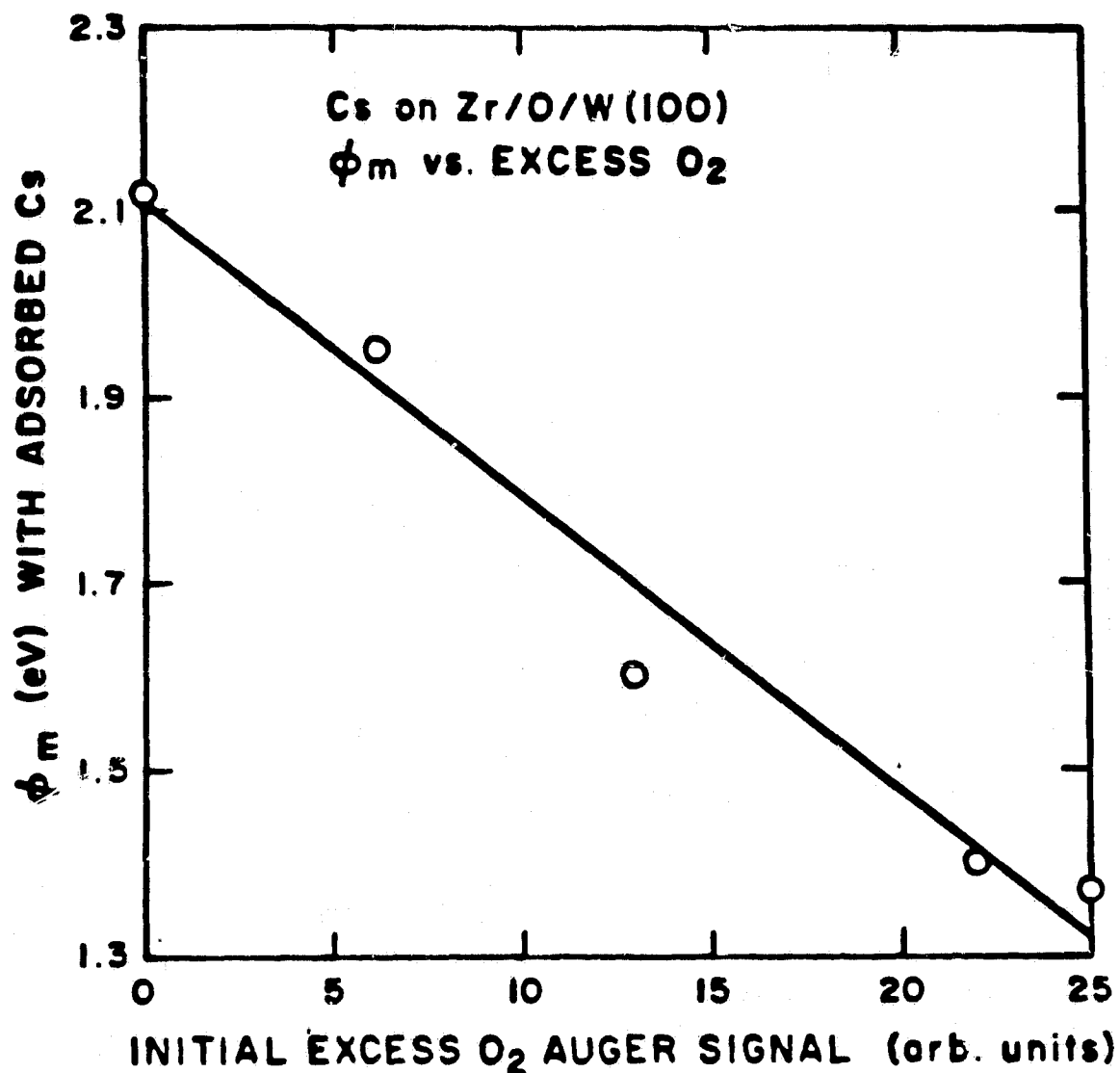


Figure 27. Work function minimum attained by cesium adsorption on Zr/O/W(100) as a function of excess oxygen adsorbed. An excess oxygen Auger signal of 25 corresponds to a saturated layer.

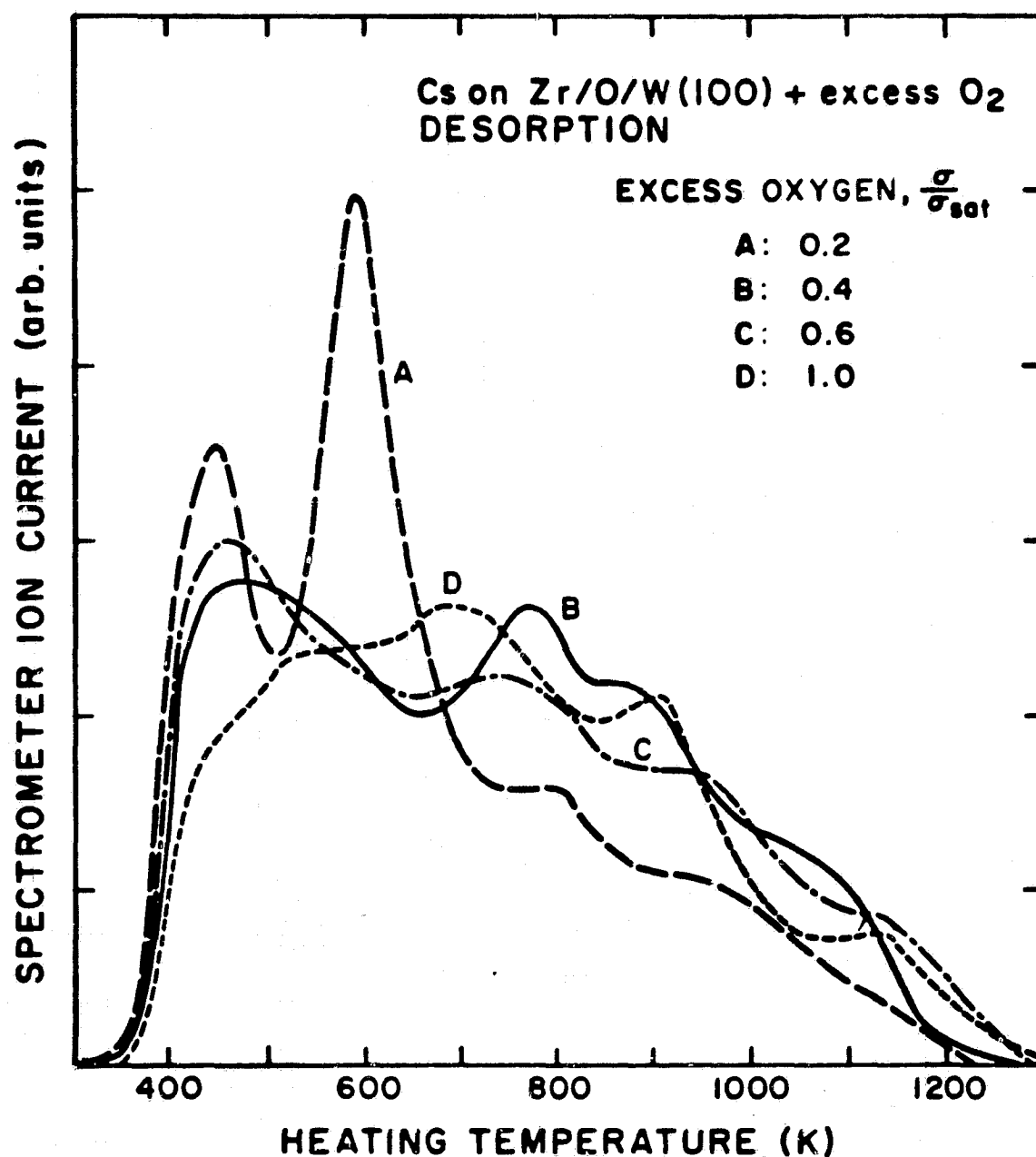


Figure 28. Thermal desorption of saturated cesium layers from various oxygen layers on Zr/O/W(100).

Zr/O/W(100) surface, the excess O₂ Auger amplitude decreases as Cs coverage increases. This result implies that Cs adsorbs on top of excess O₂, thereby attenuating the O₂ Auger signal. As determined by desorption/work function experiments (Fig. 24), the Cs adsorption/desorption process is approximately reversible on equilibrated O₂ layers.

These results indicate that the effect of adsorbed excess O₂ on the Cs adsorption/desorption characteristics of the low work function Zr/O/W(100) surface is significant. The minimum work function attained for Cs adsorption on Zr/O/W(100) is 2.12 eV, while preadsorption of excess O₂ reduces the minimum Cs work function approximately linearly with increasing O₂ coverage, yielding an absolute minimum of 1.37 eV. Excess O₂ increases the thermal stability of the Cs layer, producing a variety of binding states of energy higher than those observed without excess O₂. Equilibration of excess O₂ layers at 1600 K reduces both the surface Zr and O₂ concentrations, but the corresponding change in Cs adsorption/desorption characteristics appears to be due primarily to the decrease in surface O₂.

IV-B. Comparison of Cesium Adsorption and Cesium-Oxygen Coadsorption on Zr/O/W(100) and W(100)

It is interesting to compare these results with those obtained for cesium adsorption on clean W(100). The most recent thorough study of the Cs/W(100) system was that of Desplat,²⁸ who investigated

work function behavior, surface structure and surface composition of cesium and cesium/oxygen coadsorbed layers on W(100). Unfortunately, neither Desplat nor anyone else has made complete thermal desorption measurements for Cs/W(100). Therefore, we investigated cesium adsorption/desorption on W(100).

Measurements were performed on the same W(100) sample which had been used for Zr/O/W(100) studies. The sample was cleaned of zirconium by repeated flashing to 2400 K. A residual amount of zirconium (estimated to be < 0.2 monolayer) remained on the surface after these treatments, because zirconium was continually resupplied from the bulk. The surface oxygen and carbon were reduced to levels undetectable by AES.

A plot of FERP work function vs cesium exposure for this W(100) surface is shown in Fig. 29. The curve is based on FERP peak positions and includes a peak broadening and instrumental correction of -0.05 eV to yield absolute work functions. Cesium coverage varies linearly with dose time, as indicated by the Auger data of Fig. 30. The clean, minimum and saturated work functions given in Table VII are compared with data of Desplat²⁸ for cesium adsorption on an atomically clean W(100) crystal. The agreement is excellent implying that the effect of residual zirconium on our sample is negligible.

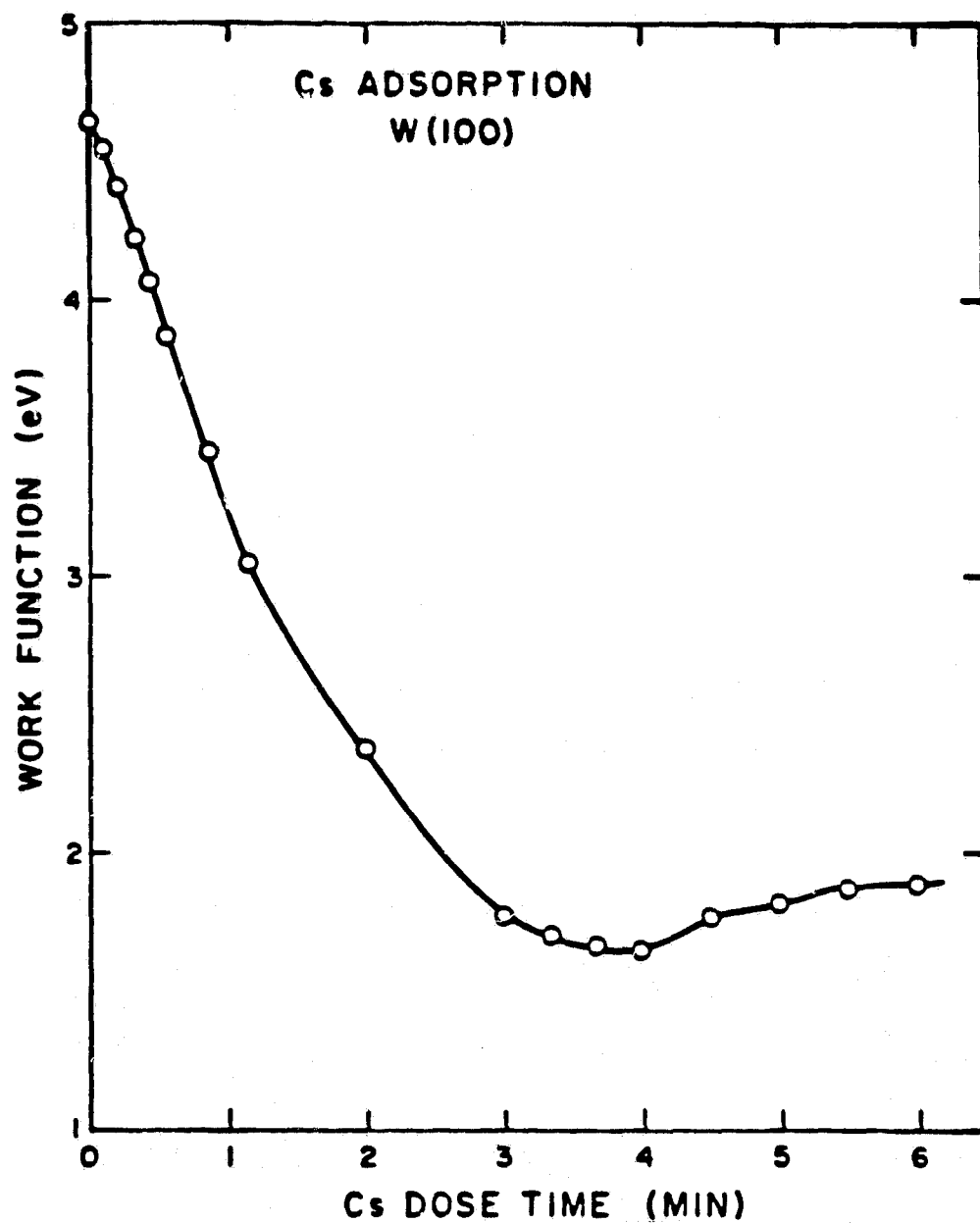


Figure 29. Variation of FERP work function on W(100) with cesium adsorption at room temperature.

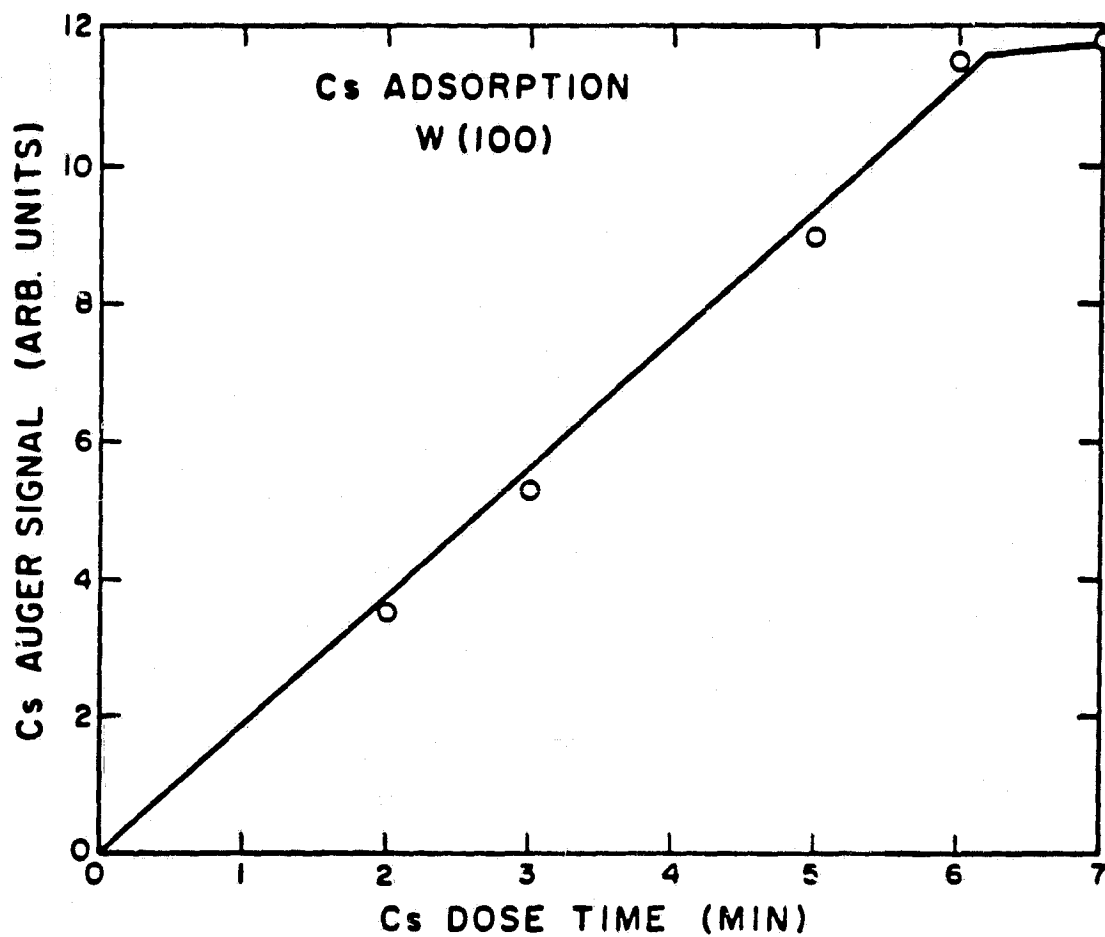


Figure 30. Variation of cesium Auger signal with cesium dose time on W(100) at room temperature.

TABLE VII
CRITICAL WORK FUNCTIONS FOR CESIUM LAYERS ON W(100)

	<u>This Work</u>	<u>Desplat (Ref. 28)</u>
ϕ_{clean}	$4.65 \pm .05$	4.65^*
ϕ_{min}	$1.65 \pm .05$	1.58
ϕ_{sat}	$1.90 \pm .05$	1.80

* Value chosen by Desplat based upon best available data. His Kelvin probe measured only work function change.

Desorption of cesium from the W(100) surface produces the spectra shown in Fig. 31. The relative cesium coverage values shown were determined from integrated peak areas of the respective desorption spectra, taking into account the kinetic energy variation with temperature of the desorbing atoms. It is clear that cesium adsorbs on the W(100) surface in at least two, and possibly three distinct binding states. The high temperature states are unchanged with cesium coverage implying first-order desorption kinetics. On the other hand, the low temperature peak shifts to lower temperature with increasing coverage, an effect that could be caused by second order kinetics or first order kinetics with coverage dependent binding energy. Using a technique devised by Redhead,¹⁸ these two cases may be separated.

Fig. 32 shows a deconvolution of the spectra of Fig. 31 to yield only the low energy peaks. Thus, the peak temperature T_p and

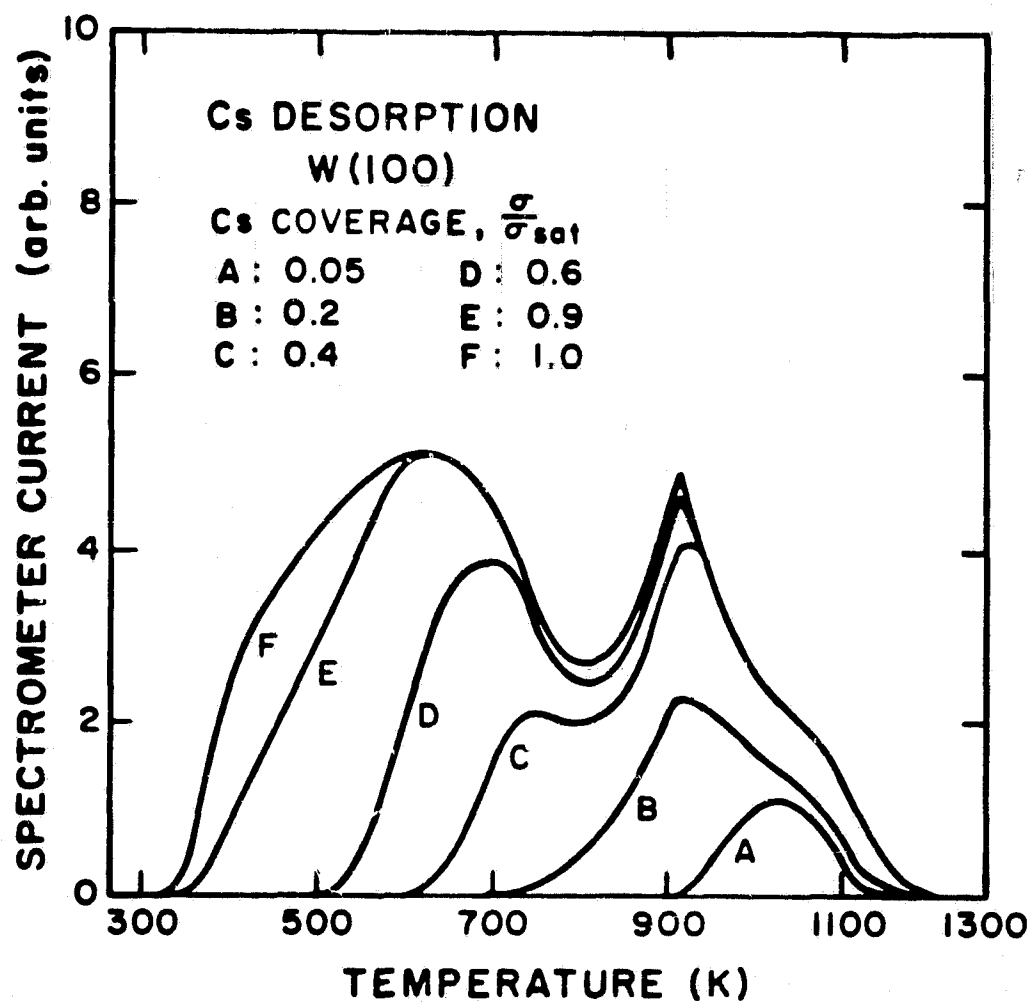


Figure 31. Thermal desorption of cesium from W(100).

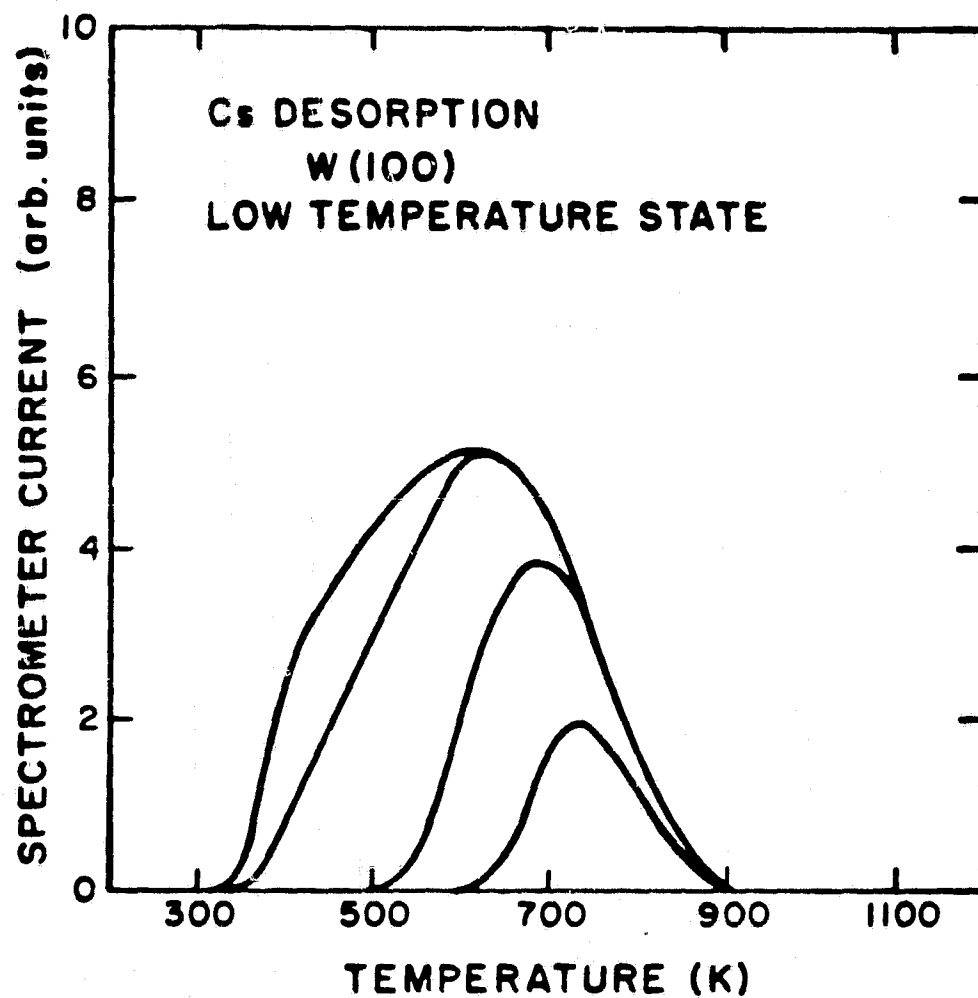


Figure 32. Low temperature data extracted from Figure 31.

initial coverage σ_0 for each spectrum may be substituted into the equation for second order desorption

$$E/kT_p^2 = \frac{\sigma_0 v_2}{a} \exp (-E/kT_p) . \quad (16)$$

If second order kinetics apply, then a plot of $\log(\sigma_0 T_p^2)$ vs $1/T_p$ should yield a straight line of slope E/k . A nonlinear $\log(\sigma_0 T_p^2)$ vs $1/T_p$ plot, on the other hand, would imply first order kinetics with a varying binding energy. As Fig. 33 shows, the latter case is applicable here. Therefore, all the peaks shown in Fig. 31 result from first order desorption processes.

The decrease with coverage of the binding energy of the low temperature state is an interesting phenomenon. In other adsorption systems, the highest energy binding states (near zero coverage) may shift with coverage, an effect generally attributed to the growing importance of adsorbate-adsorbate interactions as the coverage of the adsorbed species increases. It is known that at high coverage, cesium on the W(100) plane compresses into a pseudo-hexagonal structure, determined predominantly by adsorbate-adsorbate interactions.²⁸ The change in binding energy at high coverage which we observe may indicate the onset of this compressed two-dimensional phase.

In a previous study of cesium adsorption on W(110), a completely different desorption behavior was observed.²⁶ No discrete binding states were observed but, rather, a continuous decrease in desorption energy with increasing coverage. Nevertheless, the terminal desorption

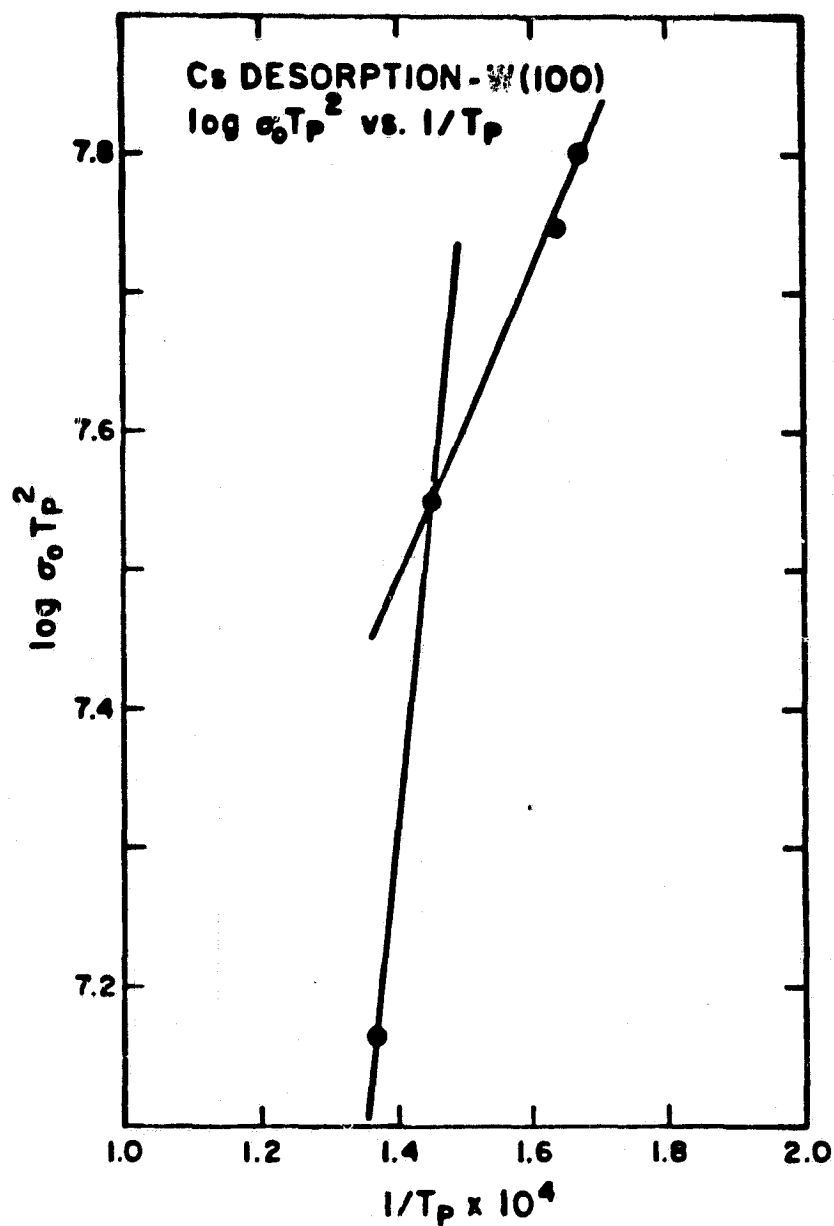


Figure 33. Plot of $\log \sigma_0 T_p^2$ vs $1/T_p$ for low temperature state of cesium on W(100), indicating binding energy change with coverage.

temperature of cesium from that surface was ~ 1400 K, compared with ~ 1200 K which we observe for cesium on W(100).

The desorption spectra of Figs. 25, 28 and 31 show that adsorbed cesium is more stable on the W(100) surface than on Zr/O/W(100), but is more stable on Zr/O/W(100) with excess oxygen. A more instructive comparison may be seen in Fig. 34, where the data of Fig. 24 are replotted with corresponding W(100) data. These curves represent pseudoequilibrium T/T_R curves at zero cesium pressure.

The work function and desorption results presented here suggest fundamental differences between cesium adsorption on Zr/O/W(100) and on W(100). The presence of the surface Zr-O complex reduces the binding energy of cesium and causes cesium to be ineffective in reducing the work function, even though this layer contains a significant amount of oxygen. Apparently, the oxygen is so tightly bound to the Zr that its electron affinity is satisfied, and little or no bonding between oxygen and cesium occurs. The addition of excess oxygen to the surface, however, creates additional active sites for cesium adsorption, thereby increasing its binding energy and enhancing the cesium surface dipole layer strength.

Using the FERP gun, we have performed electron reflection studies for cesium adsorption on Zr/O/W(100) and on W(100). The results for Zr/O/W(100) are shown in Fig. 35. The behavior is quite different from that discussed earlier for LaB₆(100) (Section II). The Zr/O/W(100) surface exhibits significant reflection near threshold which is

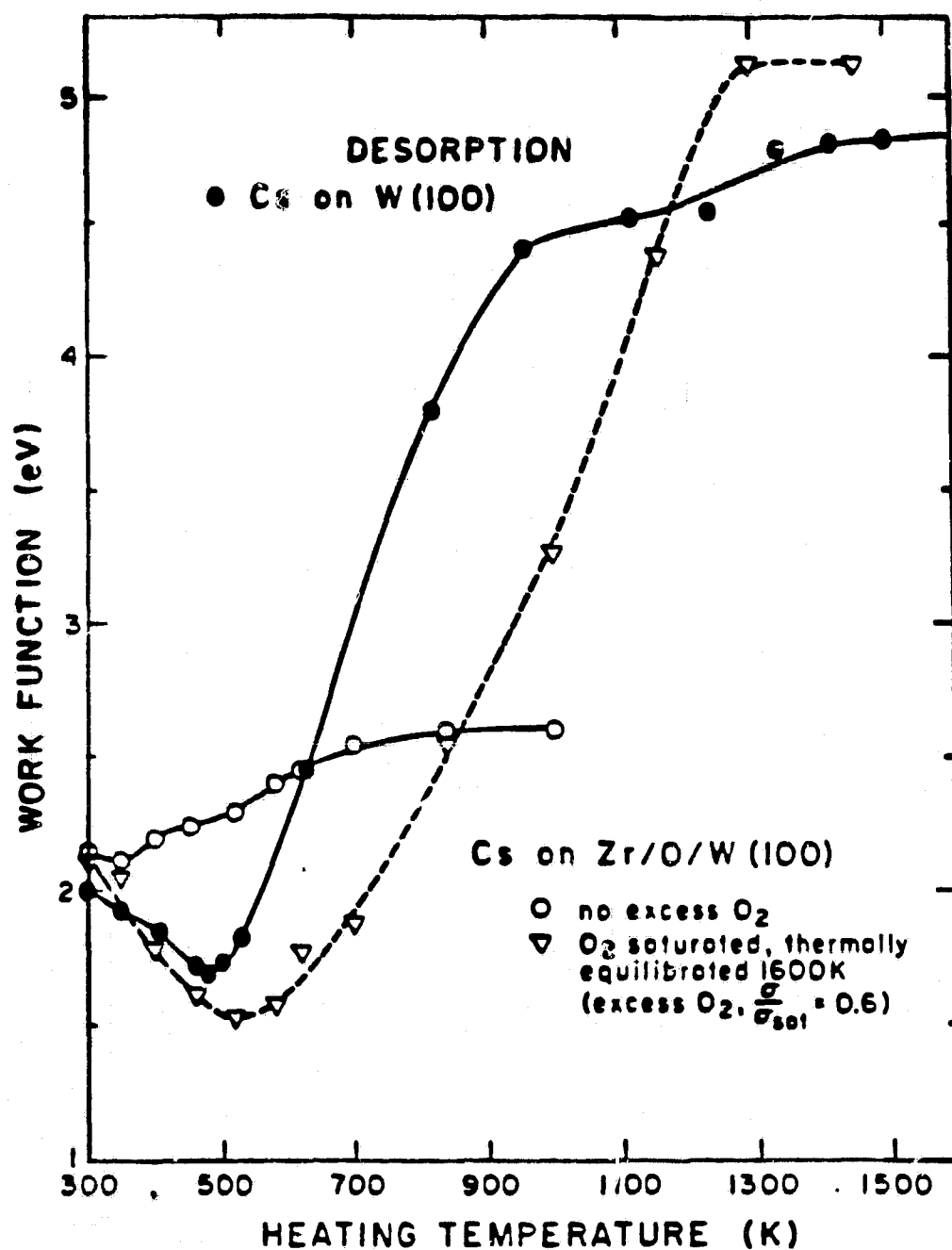


Figure 34. Stepwise, pseudoequilibrium desorption of cesium from various surfaces. Each point represents two minutes of heating at the indicated temperature followed by a room temperature FERP measurement.

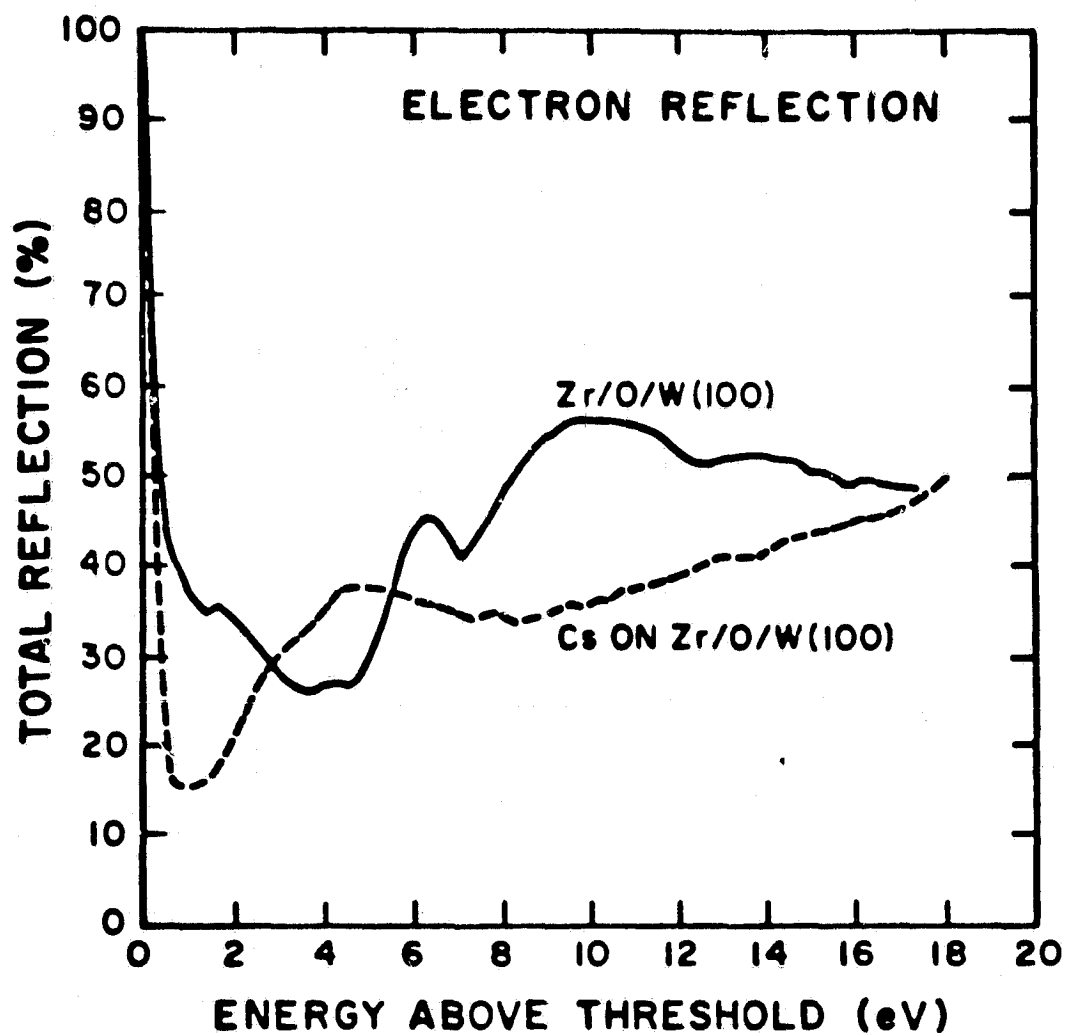


Figure 35. Total electron reflection ($V_{\text{grid}} = 22$ volts) for Zr/O/W(100) with and without a saturated cesium layer adsorbed at room temperature.

reduced when cesium is adsorbed. For thermionic converter applications, the region near threshold is of primary interest, but the curious cross-over behavior at about 3 and again at 6 eV above threshold may contain additional information on the nature of the surface layer. Unfortunately, the Cs/Zr/O/W(100) surface is so complex, both geometrically and electronically, that further interpretation of the reflection data is difficult. Note that the adsorption of cesium reduces the amount of structure in the reflection spectrum.

For comparison, Figs. 36 and 37 show, respectively, the elastic and total reflection spectra for W(100) with and without adsorbed cesium. The elastic reflection spectrum is determined by biasing the FERF gun grid so that only electrons with energies approximately equal to the incident energy (energy loss ≤ 4 eV) can be reflected. In all the cases presented here, the qualitative behavior of total and elastic reflected spectra is similar. Note also that in every case where a saturated cesium layer is present, a broad peak around 5 eV appears, regardless of the substrate. This peak may be characteristic of a close-packed cesium layer.

The conclusion to be drawn from these experiments is that the electron reflection near threshold is increased for W(100) when cesium is adsorbed (with a similar result occurring for LaB₆(100) as discussed in Section II), while the reflection from Zr/O/W(100) is reduced when cesium is adsorbed. The different behavior of the Zr/O/W(100) surface results from a high electron reflection coefficient

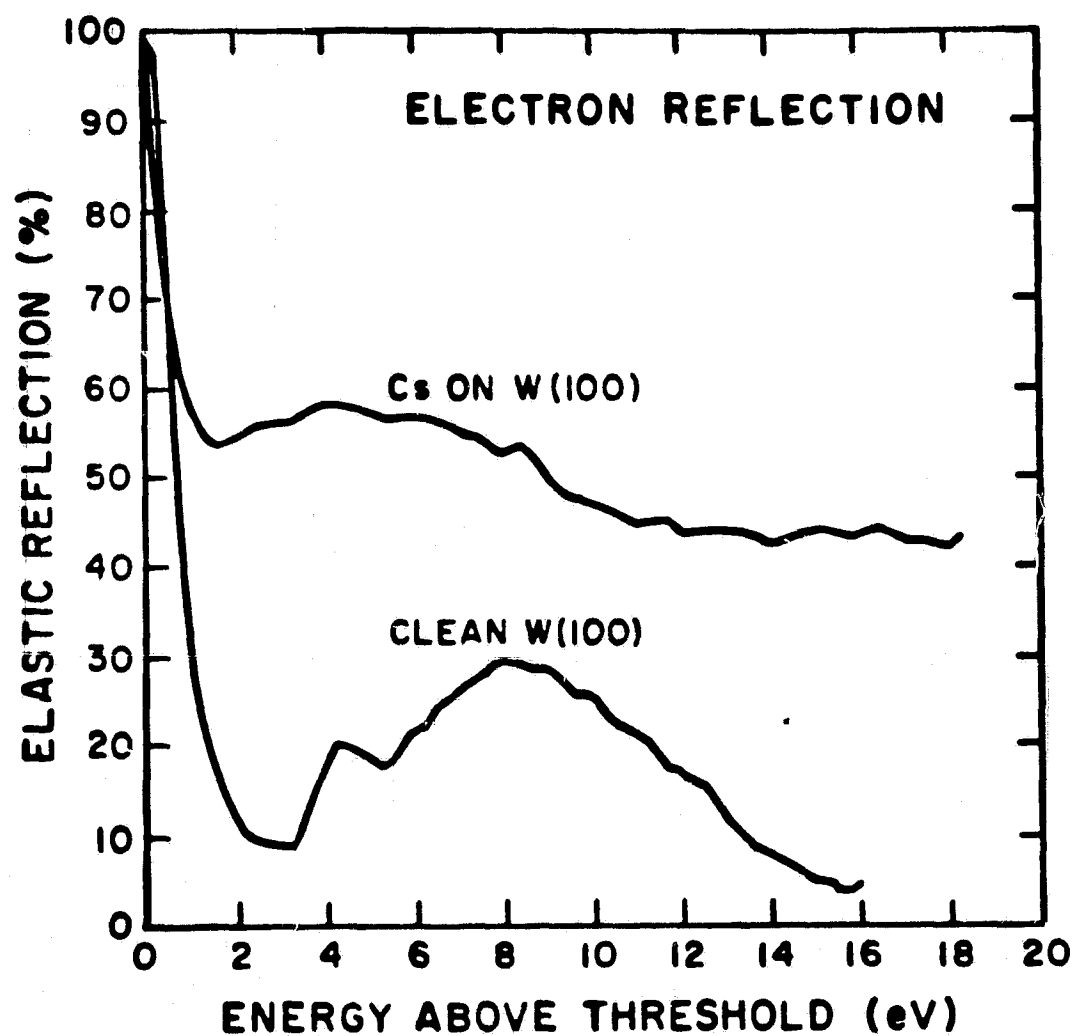


Figure 36. Elastic electron reflection ($V_{\text{grid}} = 8.9$ volts) from W(100), clean and with a saturated cesium layer adsorbed at room temperature.

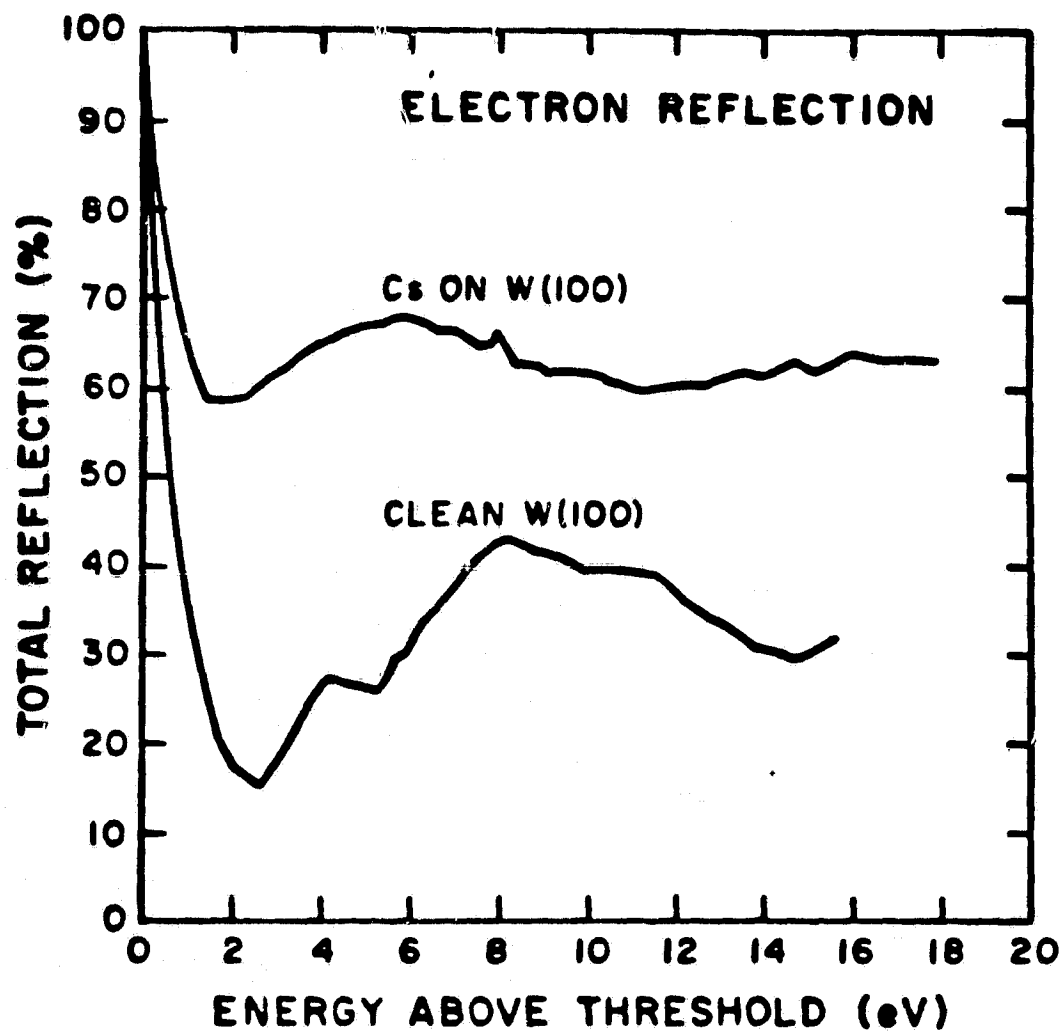


Figure 37. Total electron reflection ($V_{\text{grid}} = 22$ volts) from W(100), clean and with a saturated cesium layer adsorbed at room temperature.

for the surface without cesium, but the precise cause of this large reflection coefficient near threshold is not known.

V. Technical Summary

The objective of this project is to fabricate, characterize and evaluate electrode materials that have the potential of significantly improving converter performance. During this reporting period, studies of the thermal stabilities of clean LaB_6 single crystal faces have been performed, and investigation of the properties of adsorbed carbon, cesium and cesium-oxygen layers on LaB_6 surfaces has continued. Research on the surface properties of polycrystalline W-Zr and W-Hf alloys has been concluded. Cesium adsorption and cesium-oxygen co-adsorption on the low work function Zr/O/W(100) surface has been investigated and compared with results of cesium adsorption studies on W(100).

The relative thermal stabilities of the various crystal planes of LaB_6 were examined using field emission and field ion microscopy. Thermal faceting was observed for high index planes, and the (100), (110) and (111) planes were found to be the most thermodynamically stable faces in vacuum. The work function difference between the (100) and (110) faces could be radically changed by field evaporation in hydrogen. This latter effect may be due to referential hydrogen field evaporation of La atoms from the (100) plane.

Carbon adsorption and desorption at $\text{LaB}_{5.74}$ (100), (110) and $\text{LaB}_{5.86}$ (110) surfaces were investigated. Significant work function

increases (~ 0.2 eV) were observed for surface carbon levels less than 5% of a monolayer. Procedures were developed for removing both gas-phase adsorbed carbon and surface segregated carbon diffused from the bulk. It is likely that the generally poor showing of LaB_6 in thermionic test converters may be attributable in part to surface segregation of bulk carbon in the materials used.

The properties of adsorbed cesium and cesium-oxygen layers on $\text{LaB}_6(100)$ surfaces were studied in detail and the results compared with results of similar work on $\text{LaB}_6(110)$ surfaces. Cesium adsorption produces work function minima of 1.97 and 1.88 eV, respectively, on the initially clean (100) and (110) surfaces, whereas a preadsorbed oxygen layer yields respective minima of 1.35 and 1.47 eV with cesium adsorption. Oxygen appears to adsorb preferentially over boron sites, but the surface La atoms are also involved chemically in bonding to the adsorbed oxygen. Oxygen precoverage increases the ionic character of the cesium bond to the surface, and also increases the cesium coverage at ϕ_{min} . A simple model has been applied to the data to show that $\text{LaB}_6(100)$ would make an unsatisfactory emitter for hypothetical NEP cesium vapor converter applications. On the other hand, $\text{LaB}_6(100)$ with adsorbed oxygen could be a suitable collector for such applications.

Characterization of a set of polycrystalline Zr-W and Hf-W alloy sample surfaces has been completed. Because of the inhomogeneous nature of these surfaces, detailed understanding of their geometric and electronic properties is not possible. Therefore,

similar proposed experiments on polycrystalline Zr-Mo and Hf-Mo samples have been abandoned in favor of careful, controlled studies on the related, single crystal surface Zr/O/W(100).

Cesium and oxygen adsorption on the Zr/O/W(100) surface have been investigated. The minimum work function attained for cesium adsorption on Zr/O/W(100) is 2.12 eV, while preadsorption of excess oxygen reduces the minimum cesium work function approximately linearly with increasing oxygen coverage, yielding an absolute minimum of 1.37 eV. Excess oxygen increases the thermal stability of the adsorbed cesium layer, producing a variety of binding states of energy higher than those observed without excess oxygen. Similar measurements were made on a W(100) sample and the thermal stabilities and work function characteristics of cesium layers on W(100) and Zr/O/W(100) were compared. Cesium was found to adsorb more strongly on W(100) than on Zr/O/W(100), unless excess oxygen was present on the latter surface. The work function lowering effect of cesium was more pronounced on W(100) than on the low work function Zr/O/W(100) surface.

Finally, low energy electron reflection measurements were performed for LaB₆(100), Zr/O/W(100) and W(100) surfaces with and without adsorbed cesium. Cesium was found to increase electron reflection near the collection threshold on LaB₆(100) and W(100) but decrease the reflection on Zr/O/W(100). This difference may be explained by the unusually high threshold reflection coefficient of Zr/O/W(100) without adsorbed cesium.

REFERENCES

1. J. F. Morris, NASA TMX-7149 (1974).
2. R. W. Strayer, W. Mackie and L. W. Swanson, Surf. Sci. 34 (1973) 225.
3. E. Storms and B. Mueller, J. Phys. Chem. 82 (1978) 51.
4. L. W. Swanson and N. A. Martin, J. Appl. Phys. 46 (1975) 2029.
5. L. R. Danielson and L. W. Swanson, Surf. Sci. 88 (1979) 14.
6. P. R. Davis and L. W. Swanson, Annual Report (JPL Contract No. 955156, December 1979).
7. L. W. Swanson, D. R. McNeely and M. Gesley, NASA CR-159649 (Lewis Research Center, August 1979).
8. L. W. Swanson and T. Dickinson, Appl. Phys. Lett. 28 (1976) 578.
9. M. Futamoto, S. Hosoki, H. Okano and U. Kawabe, J. Appl. Phys. 48 (1977) 3541.
10. T. Sakurai, G. Robertson and Y. Kuk, Proc. Electrochem. Soc. 80-1 (1978) 608.
11. M. A. Noack, M. S. Thesis (Iowa State University, 1979).
12. C. Oshima, E. Bannai, T. Tanaka and S. Kawai, Jpn. J. Appl. Phys. 16 (1977) 965.
13. P. W. Palmberg, G. E. Reach, R. E. Weber and N. C. MacDonald, Handbook of Auger Electron Spectroscopy (Physical Electronics, Inc., Edina, MN, 1972).
14. Progress Report No. 40, Thermo Electron Corp., DOE Contract EY-76-C-02-3056 and JPL Contract 955009 (July-September 1979).

15. L. W. Swanson and R. W. Strayer, J. Chem. 48 (1968) 2421.
16. L. W. Swanson and D. R. McNeely, NASA CR-155582 (Lewis Research Center, June 1979).
17. L. W. Swanson and D. R. McNeely, Surf. Sci. 83 (1979) 11.
18. P. A. Redhead, Vacuum 12 (1962) 203.
19. B. Goldstein and D. J. Szostak, Surf. Sci. 74 (1978) 461.
20. R. Nishitani, S. Kawai, H. Iwasaki, S. Nakamura, Surf. Sci. 92 (1980) 191.
21. J. R. MacDonald and C. A. Barlow, Jr., J. Chem. Phys. 39 (1963) 412.
22. P. R. Davis and S. A. Chambers, Appl. Surf. Sci. (in press).
23. C. A. Papageorgopoulos and J. M. Chen, Surf. Sci. 39 (1973) 313.
24. C. A. Papageorgopoulos and J. M. Chen, J. Vac. Sci. Technol. 9 (1972) 570.
25. J.-L. Desplat, Jpn. J. Appl. Phys. Suppl. 2, Pt. 2 (1974) 177.
26. J.-L. Desplat and C. A. Papageorgopoulos, Surf. Sci. 92 (1980) 97.
27. J.-L. Desplat and C. A. Papageorgopoulos, Surf. Sci. 92 (1980) 119.
28. J.-L. Desplat, Thesis (University of Paris - Orsay, 1974).
29. C. A. Papageorgopoulos and J. M. Chen, Surf. Sci. 52 (1975) 40.
30. C. Oshima, M. Aono, T. Tanaka, R. Nishitani and S. Kawai, J. Appl. Phys. 51 (1980) 997.
31. C. Oshima, M. Aono, T. Tanaka, S. Kawai, R. Shimizu and H. Hagiwara, J. Appl. Phys. 51 (1978) 1201.
32. Report No. TE4258/4247-226-80 (Thermo Electron Corp., Jan-Mar 1980).
33. P. R. Davis and H. R. Poppa, J. Vac. Sci. Technol. 15 (1978) 1771.

APPENDIX

Summary of Conference Attendance

During this contract year, OGC personnel have participated in a variety of conferences, workshops and other meetings related to thermionic energy conversion. A summary of such activity is given below.

- 1) April 15-17, 1980 - P. R. Davis and L. W. Swanson attended Tri-Services Cathode Workshop, Griffiss AFB, Rome, NY. Papers presented: P. R. Davis and S. A. Chambers, "The Desorption of Oxide Species from $\text{LaB}_{5.74}(100)$ "; L. W. Swanson, "Recent Progress in Thermal Field Electron Source Performance." These papers are to be published in Appl. Surf. Sci.
- 2) April 18, 1980 - P. R. Davis presented a general seminar at Central Wyoming College, Riverton, WY entitled "Thermionic Energy Conversion."
- 3) May 19-21, 1980 - L. W. Swanson attended IEEE International Conference on Plasma Science, University of Wisconsin - Madison. Papers presented: L. W. Swanson, H. K. Chen, and P. R. Davis, "Cesium Adsorption on the Zr/O/W(100) Surface"; P. R. Davis, S. A. Chambers and L. W. Swanson, "The Adsorption of Cesium on Lanthanum Hexaboride Surfaces."
- 4) May 21, 1980 - L. W. Swanson attended Thermionic Converter Electrode Workshop held in conjunction with the IEEE Conference.

- 5) June 12-14, 1980 - S. A. Chambers attended the Joint Rocky Mountain/Pacific Northwest ACS Regional Meeting, University of Utah, Salt Lake City, Utah.

Paper presented: S. A. Chambers, "Interaction of Cesium and Oxygen with $\text{LaB}_6(100)$."

- 6) June 27, 1980 - P. R. Davis and L. W. Swanson visited JPL, Pasadena for technical program review by K. Shimada and J. Mondt.

- 7) August 21-22, 1980 - P. R. Davis and L. W. Swanson attended Intersociety Energy Conversion Engineering Conference, Olympic Hotel, Seattle, WA.

Papers presented: P. R. Davis, S. A. Chambers and L. W. Swanson, "The Adsorption of Cesium on Lanthanum Hexaboride Surfaces"; H. K. Chen, L. W. Swanson and P. R. Davis, "Cesium Adsorption on the $\text{Zr/O/W}(100)$ Surface."